LiDAR Enhanced Closed-Loop Active Wake Mixing Control

Zekai Chen

Master of Science Thesis

Delft University of Technology

Delft Center for Systems and Control

LiDAR Enhanced Closed-Loop Active Wake Mixing Control

Master of Science Thesis

For the degree of Master of Science in Mechanical Engineering (ME) at
Delft University of Technology

Zekai Chen

January 14, 2025

Faculty of · Delft University of Technology

Delft University of Technology
Department of
Delft Center for Systems and Control (dcsc)

The undersigned hereby certify that they have read and recommend to the Faculty of for acceptance a thesis entitled

LiDAR Enhanced Closed-Loop Active Wake Mixing Control

by

Zekai Chen

in partial fulfillment of the requirements for the degree of

Master of Science Mechanical Engineering (ME)

Dated: January 14, 2025

Supervisor(s):

prof.dr.ir. J.W. van Wingerden

ir. A.A.W. van Vondelen

Reader(s):

dr.ir. A.J. Laguna

dr.ir. M. Coquelet

dr.ir. M. Zagorowska

Abstract

When turbines are placed aligned in a wind farm, the downstream wind turbines suffer from the wake effect, reducing their power production and increasing structural loads. To address this, wake mixing control strategies are designed to enhance the mixing of free-stream air with the turbine's wake, which eventually improves overall wind farm performance. Among all strategies, the Helix approach gains attention for the lower structural loads and slightly better mixing effect. However, the Helix approach is currently implemented in an open-loop manner, limiting its ability to manage deviations introduced by external disturbances that a closed-loop controller can potentially handle. Thus, this thesis investigates closed-loop wake mixing control using Light Detection and Ranging (LiDAR) as a feedback measurement device. The LiDAR subsystem uses a continuous-wave LiDAR with additional assumptions to sample flow data. A data processing pipeline extracts the hub jet as the control feature of the Helix. A coordinate transformation is used to map the rotating hub jet from the fixed frame to the Helix frame where it becomes a constant bias, simplifying control design significantly. Due to the time for the wake to propagate to the measurement position, the system exhibits a constant time delay τ. Consequently, a Smith predictor based on Internal Model Control (IMC) is employed to compensate for the τ in the control subsystem. Initially, a decentralized control strategy is attempted by decoupling the Multiple-Input, Multiple-Output (MIMO) system and designing a diagonal controller. However, this approach fails due to strong coupling at bandwidth frequencies. Consequently, an $\mathcal{H}_\infty$ controller is designed to control the MIMO system effectively.

The performance of the designed framework is evaluated in QBlade with the National Renewable Energy Laboratory (NREL)-5MW wind turbine. For comprehensive comparisons, multiple cases are simulated under shear, turbulence, and combined shear and turbulence wind conditions. The results show that the designed framework aligns with open-loop performance under uniform wind conditions, and achieves a 5% power increase in the downstream turbine and a 1% increase in the two-turbine setup under shear conditions. Limitations are noted in handling high-frequency turbulence. Nevertheless, the proposed framework demonstrates great potential, offering a novel perspective in deploying wake mixing control.

Table of Contents

List of Figures

List of Tables

Acknowledgements

If someone had told me 8 years ago when I failed my high school math exam for the first time that I would one day complete research like this, I would have thought he was high. And yet, here I am. Looking back, these past 8 years were far from smooth. Conversely, they were filled with senses of being lost, despair, and pain. I used to hate those struggles and envied an easier life. However, now I am as nostalgic for the bad as I am for the good. In Chinese mythology, the phoenix rises from the ashes and flames. Today, I am a firm believer in this wisdom.

This work would not have been possible without the support of many people. First, I would like to thank my supervisors, Professor Jan-Willem van Wingerden and Mees van Vondelen, for their guidance and support. I also want to express my sincere gratitude to the entire Data Driven Control group at DCSC, Professor David Schlipf, and Professor Mohammad Khosravi for providing me with resources and suggestions, without which I would have faced far greater struggles. Moreover, I would like to thank my friends Jingru Feng, Yucheng Shang, Xufang Yang, Kaiyi Zhao, Sawa Bezelev, Brigitte de Graaf, Laurens Hoogenboom, Leon Kehler, Adbulkayum Mukhamedov, Niels Stienen, Willem van der Linden, Floris van Leeuwen, and many others. Your invaluable friendships have been the best weapon to life's hardships. With that being said, thanks to some breweries in the Netherlands, Belgium, Ireland, and Germany, turns out alcohol can occasionally be a medicine.

Thanks to all who supported me. You guys brought tears to my eyes when listening to one of my favorite songs, *Bad* by U2. And to those who knocked me down, thank you as well. You guys helped me understand that what doesn't kill you makes you stronger 80% of time, while the other 20% crashes you completely and teaches you hard lessons.

Lastly, I want to thank my family. I am endlessly grateful to be part of such a wonderful family. I cannot tell you how many times when I felt on the verge of breaking down, only to be saved by just a glimpse of the family photo. The four of us made me realize that love is the best antidote.

Thank you all, love you all, and I love my life.

Delft, University of Technology — Zekai Chen
January 14, 2025

”Up the mountain of books, there is a path of diligence; Across the boundless sea of learning, there is a boat made from hard work.”

— *Yu Han*

Chapter 1

Introduction

Wind energy, together with other renewable energy sources, plays a key role in mitigating climate change and achieving energy sustainability [1]. A wind farm represents a pattern for wind turbine operation, wherein several units of turbines are placed strategically by a certain configuration in a concentrated area to produce electricity. When placed together in arrays to make wind farms, wind turbines are subject to the aerodynamic interaction among each other that greatly reduces downstream turbines' power production, increases structural loading and maintenance, reduces lifetime, and ultimately increases the levelized cost of energy [2]. This interaction is called the "Wake Effect".

1-1 Wake Effect

The wake effect refers to the reduced speed and turbulent air that the downstream turbine experiences under the existence of the upstream turbine. This chapter aims to introduce the wake effect in terms of the wake phenomenon and wake effect on the downstream turbine.

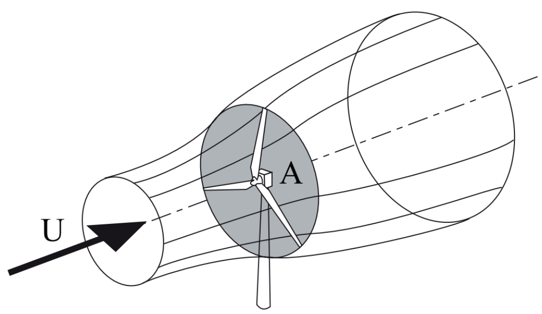

Figure 1-1: Wind Turbine actuator disk model, **A** and **U** represent the rotor disc and perpendicular component of wind speed to the rotor disc. Figure adapted from [3].

1-1-1 Wake Phenomenon

When a wind turbine operates, the momentum of the inflow wind passes through the rotor plane and is converted into aerodynamic forces that cause the rotor to rotate. In the actuator disk model, this process is conceptualized as a stream tube passing through an imaginary rotor disk illustrated by Fig. 1-1. From the figure, it can be noticed that the diameter of the upstream stream tube is smaller than the downstream. This occurs because the mass flow rate of the wind through the tube must stay constant and the air behaves as incompressible at these velocities. Consequently, as the wind speed decreases downstream, the cross-sectional area of the stream tube correspondingly increases to maintain the flow rate [3]. The area region behind the turbine where the flow is changed is called the turbine wake.

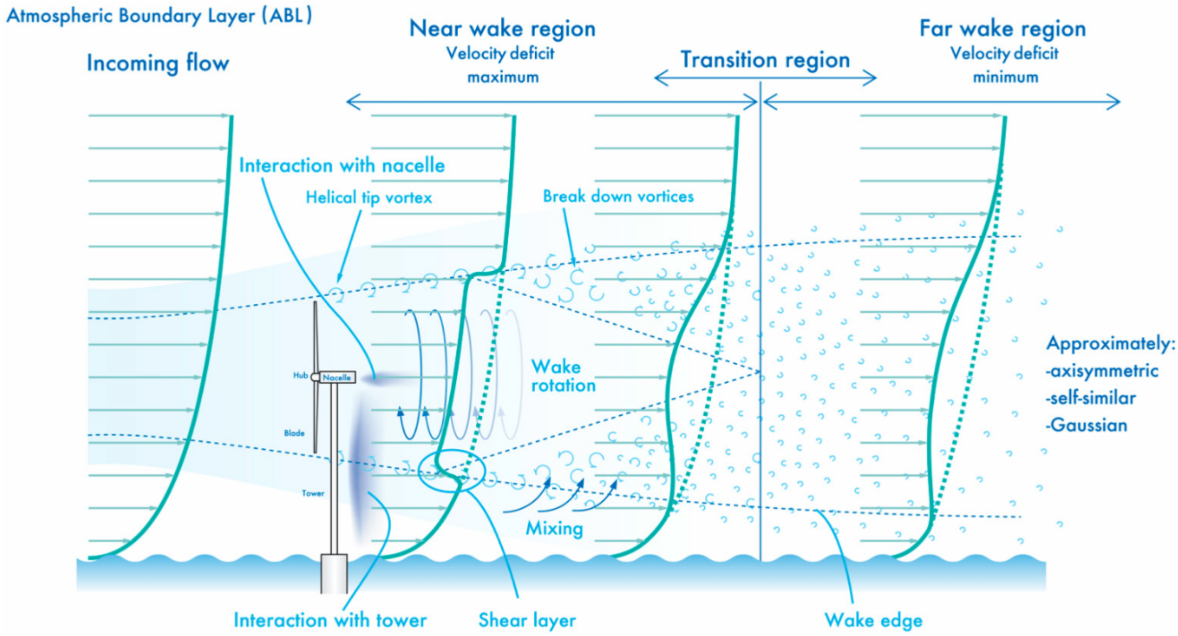

Figure 1-2: Different regions in a wind turbine wake. Figure adapted from [4].

Based on the distance to the rotor disk, the wake region could be divided into near-wake and far-wake. As depicted in Fig. 1-2, this division shows the differences in flow characteristics. The near-wake region, typically extending from 2 to 4 rotor diameters from the turbine, is marked by a noticeable reduction in wind speed and the clear structure of tip and root vortices [5]. Additionally, the turbulence intensity is increased because of the blade tips vortex generated from the rotating blades. As distance increases, the vortices are broken down and the speed-deficit air mixes with the high-speed free-stream air. This interaction leads to a recovery in wind speed within the wake and a decrease in shear. Eventually, the wind speed deficit is eliminated by the mixing.

To understand the wake effect, it is crucial to understand the dynamics of how the wake propagates from the upstream turbine to the downstream turbine. In the work of Korb [6], wake deflection, deformation, and meandering are distinguished:

- Wake Deflection: A translation of the wake center line due to forces exerted by the turbine.

- Wake Deformation: The change of wake shape without changing the wake center line.
- Wake Meandering: the lateral motion of the wake, characterized by the fluctuation of the wake center around a center line both horizontally and vertically. This is primarily triggered by large-scale motions within the background turbulence, resulting in heightened dynamic loading on the downstream turbine [7].

The dynamics of the wake, compounded by factors such as wind shear and the kidney-shaped configuration of the wake enhance the complexity of wake behavior [8]. These factors collectively affect the downstream turbine, influencing its power output and loads.

1-1-2 Wake Effect on Downstream Turbine

As analyzed in the previous chapter, the wake effect leads to wind speed deficit and increasing turbulence intensity. This results in less power production and increased structural loads in the downstream wind turbine [9]. An experimental study conducted in 2011 [10] found that the loss in maximum power coefficient of the downstream turbine varies between about 20% to 45% depending on the distance between the turbines and their operating conditions. The study highlights that the thrust of the downstream turbine is significantly lower compared to an unobstructed turbine. This reduction in both power and thrust coefficients for the downstream turbine is the result of a velocity deficit within the wake. Consequently, the downstream turbine encounters a significantly reduced free-stream velocity compared to the upstream turbine, leading to less energy being available in the flow. This can be noticed by the large blue area shown in Fig. 1-3. This phenomenon underlines the critical impact of wake effects on turbine efficiency and performance in wind farms [10].

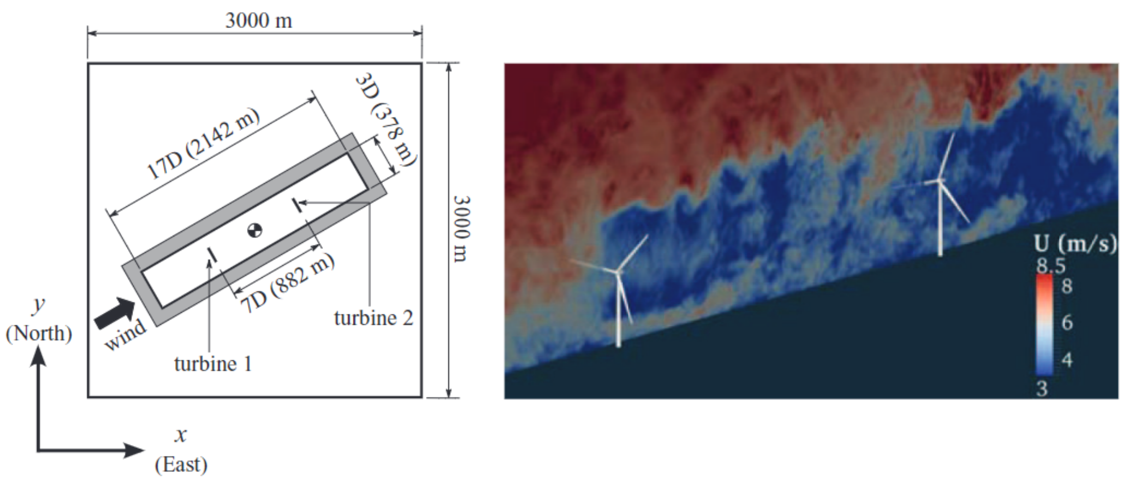

Figure 1-3: Wake between two turbines, an experiment setup. Figure adapted from [10].

To mitigate the negative influences of wake on the downstream turbines, some research aims at arranging wind turbines more effectively [11], while other studies are working on control methods to get the best performance out of wind farms. In the next chapter, wind farm flow control strategies will be introduced to alleviate the wake effect within a wind farm.

1-2 Wind Farm Flow Control

Control strategies to compensate for the negative effects of the existing wake are called the wake management technique, i.e. Wind Farm Flow Control (WFFC) strategies. To ensure reliable and low-cost operation and the best possible performance, control solutions are critical to optimizing the turbine power production while balancing structural loading through the turbine components [7]. In reality, WFFC relies on actuation at the turbine level [7]. Consequently, to provide an overview of WFFC strategies, the subsequent chapter first introduces the control of a single wind turbine. Subsequently, it presents the three main categories of WFFC: Axial Induction Control (AIC), Wake Steering, and Wake Mixing control strategies.

1-2-1 Single Wind Turbine Control

Degrees of freedom in controlling a single wind turbine involve adjusting several key variables to optimize performance and efficiency. These variables include:

- Generator torque set-point k;
- Blade pitch angle β_i;
- Turbine yaw setting γ.

Changing these variables individually or in combination can lead to variation in induction factor a. This is defined as Eq. 1-1 shows. In the equation, U_∞ represents the wind speed at hub height, and U_{disc} is the wind speed at the rotor disc:

$$a = \frac{U_\infty - U_{\text{disc}}}{U_\infty} \tag{1-1}$$

The change of induction factor a consequently leads to changes of both thrust coefficient C_{t} and power coefficient C_{p}. The formulas for these coefficients are outlined in Eqs. 1-2 and 1-3 respectively. The power coefficient C_{p} is particularly crucial as it reflects the ratio of generated power to available power, and directly measures the turbine's power generation efficiency [12]. Hence, maximizing the power coefficient C_{p} is a primary objective of turbine controllers because it directly enhances the energy output efficiency of the wind turbine. However, achieving a power coefficient of 1 is impossible in wind turbine technology, implying that the rotor would need to be a solid disk to achieve such efficiency. Consequently, all wind turbines are subject to the Betz limit, which stipulates that no turbine can convert more than 59.3% of the kinetic energy of the wind into mechanical energy for rotor movement [13]

$$C_{\text{t}} = 4a(1-a) \tag{1-2}$$

$$C_{\text{p}} = 4a(1-a)^2. \tag{1-3}$$

Changing the blade pitch angle β or generator torque set-point k also affects the tip speed ratio. This is defined as the ratio between the wind velocity and the velocity of the blade tips. In Eq. 1-4, ω is the rotation rate of the rotor and D is the rotor diameter. This variable directly affects the power generated and, consequently, the effectiveness of the investment made [14]:

$$\lambda = \frac{\omega D}{2U_\infty} \tag{1-4}$$

Despite various control options, the collective effects on flow physics resulting from turbine actuation are treated as a control input when discussing wind farm control. This simplification focuses on the aggregated impact of adjustments made across multiple turbines rather than delving into the specifics of individual turbine actuation. Nevertheless, it is important to mention that this simplification may be sufficient for effective wake flow development, it becomes significant when considering the impacts on turbine loads and power production. Subsequently, should be included in the overall control optimization [7].

A wind turbine operates in various modes, each determined by the wind speed. By visualizing the relationship between the change of wind speed to the generator power and the rotor thrust, a power and thrust curve can be acquired. Figure. 1-4 illustrates the power-thrust curve of the National Renewable Energy Laboratory (NREL) 5MW wind turbine, which is the turbine used in this study.

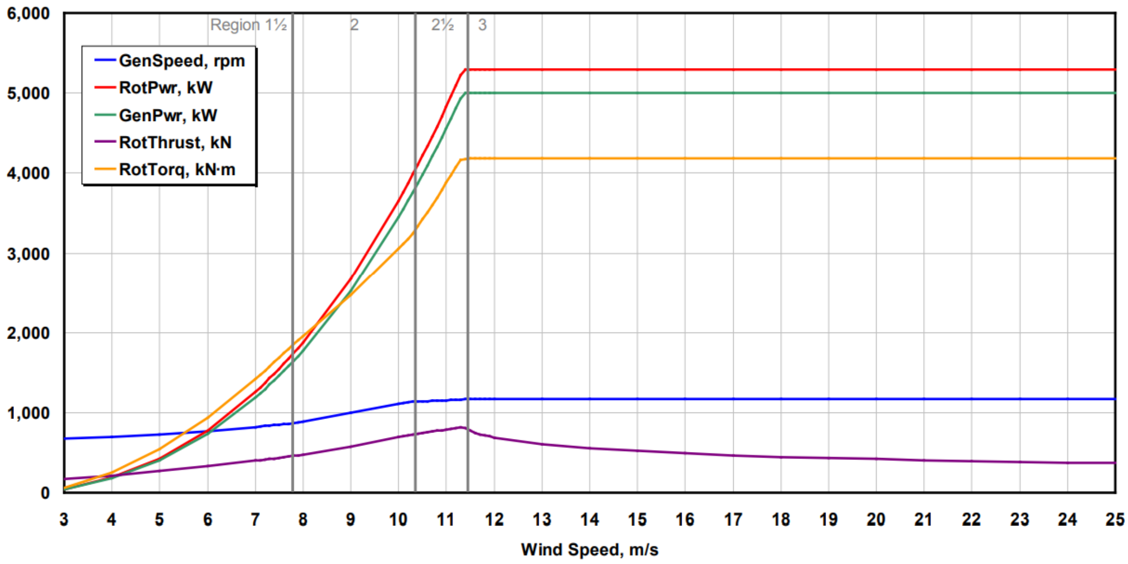

Figure 1-4: Power and thrust curve for the NREL 5MW offshore wind turbine [15].

From Fig. 1-4, it can be noticed that the wind turbine begins to generate power once the wind reaches the cut-in speed. This is defined as the lowest wind speed at which the turbine can produce electricity. With the increasing wind speed, the turbine enters Region 2, where the torque controller plays a critical role in tracking the set point for the tip-speed ratio. The set point is set near or at maximum C_p to ensure maximum power output by adhering to the ideal λ [16]. Upon reaching the rated wind speed, the system stabilizes the power output at a constant level in Region 3. As wind speed continues to rise, the required thrust to maintain the turbine's rated power output decreases. Eventually, the turbine is turned off when the wind speed surpasses a predetermined threshold to ensure safety.

Building upon the preceding introduction, the following sections of this chapter present the three categories of WFFC strategies in detail.

1-2-2 Axial Induction Control

Axial induction control involves deliberately operating the upstream turbine at less than its maximum capacity, with the aim of decreasing the velocity deficit in the wind that reaches the downstream turbines to improve the overall performance of the wind farm. The "derate" of the upstream turbine can be achieved by changing the blade pitch angle β or the generator torque k. However, the potential for increased energy extraction from static induction control is rather low [17]. This could be explained by the fact that the possible kinetic energy gains in the wake results from under-induction are mainly concentrated at the outer part of the wake [18]. Moreover, field tests show that the energy benefit of the AIC is minimal [17]. Another way to implement AIC is by over-induction, a study shows that this method leads to faster wake breakup through LES simulation, which could improve the energy extraction of the downstream wind turbine [19].

1-2-3 Wake Steering Control

The goal of wake redirection is to divert the wake flow to mitigate the impact of the wake effect experienced by turbines downstream through yawing or tilting the wind turbine. This strategy that redirects wake away is also called wake steering.

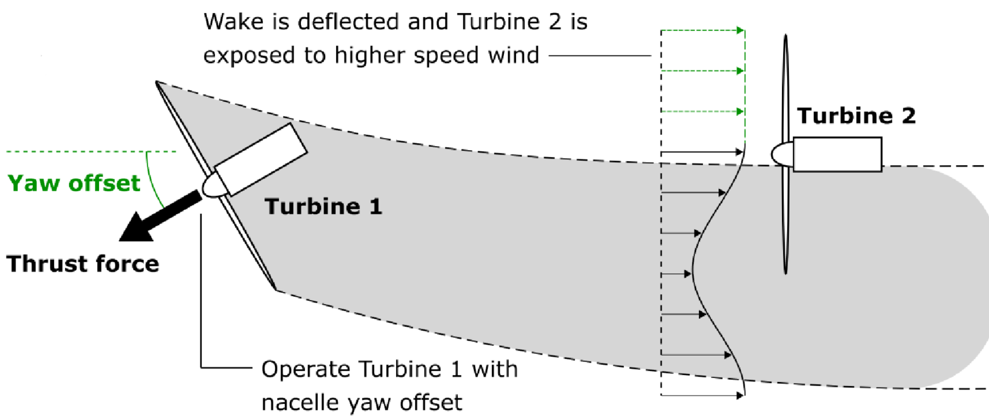

Figure 1-5: Top view of wake steering through yawing for a two-turbine setup. Figure adapted from [20].

To redirect the wake, the turbine nacelle is yawed to misalign the rotor plane with the inflowing wind, creating aerodynamic imbalances that generate crosswind forces, altering the wake's trajectory [20]. The redirected wake diverges from its initial path, decreasing its overlap with the rotor of a downstream turbine. As a result, parts of the downstream rotor encounter higher speed and less turbulent wind, which can lead to an increase in power generation that may surpass the power reduction in the upstream turbine due to yaw misalignment. This process is illustrated in Fig 1-5.

1-2-4 Wake Mixing Control

The wake mixing control strategy is developed to enhance the mixing of the turbine's wake with ambient free-stream velocity air. This enhanced mixing accelerates the energy recovery of the wake more effectively than would occur through natural wake processes and recovery mechanisms.

Strategy	Name	Actuation Object	Definition
Wake Mixing	Pulse Approach	C_{t}	The induction factor a is dynamically changed in a sinusoidal pattern whose amplitude and frequency are found using a grid search. As a result, the periodic shedding of vortex rings is generated behind the upstream turbine [21].
	Helix Approach	β	By applying a phase-shifted sinusoidal signal to each blade, the fixed frame tilt and yaw moments acting on the turbine are altered. This variation results in a helical-shaped wake [22].

Table 1-1: Summary of active wake-mixing methods.

Drawing inspiration from the sinusoidal variation of yaw control to promote wake meandering, Munters and Meyers introduced a sinusoidally varying thrust coefficient aimed at inducing further mixing within the wake [21]. This actuation leads to the excitation of a train of larger annular vortex rings surrounding the wake that entrain high-speed fluid into the core of the wake [7]. Consequently, this forms a pulse-shaped pattern within the wake, hence giving the name to this approach "The Pulse Approach". Additionally, Frederik et al. explored another way of conducting wake mixing based on employing a modulation of classical cyclic pitch control to trigger the helicoidal breakup of the wake [22]. This method is termed "The Helix approach" [22]. These two approaches constitute the current landscape of active wake-mixing control strategies. A summary of these methods can be found in Table 1-1.

Figure 1-6 shows the effect of the pulse approach and Helix approach. The dark blue represents the iso-surface of the velocity and the light blue represents the velocity magnitude. From the figure, it can be noticed that the downstream turbine suffers the most in the baseline scenario. When the pulse approach is implemented, a pulsating wake is created. The mixed wake provides the downstream turbine with high-energy air, which results in an increase in power extraction for both the downstream turbine and the wind farm. When the Helix approach is employed, a helical wake is produced through Individual Pitch Control (IPC) from the upstream turbine. This consistent mixing of high-energy air and low-energy air generates the result of the most significant increase in power production for the downstream turbine. This thesis focuses on the latter method of the Helix approach, which will be discussed in detail in Chapter 1-3.

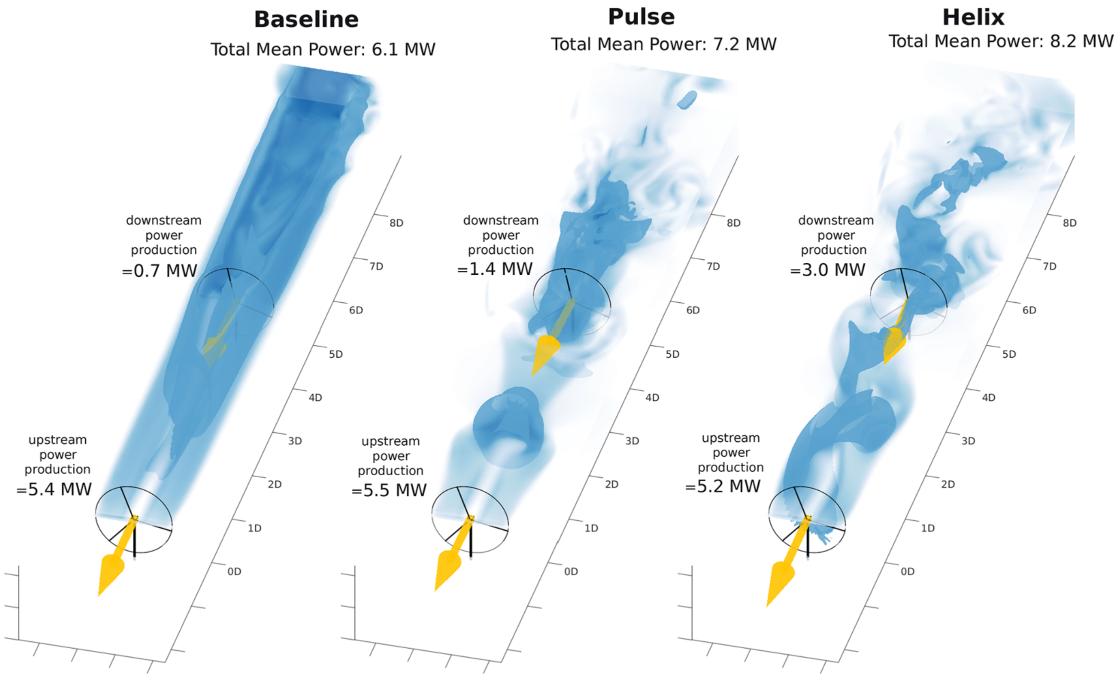

Figure 1-6: Comparison of baseline case and cases where pulse approach and Helix approach are actuated. Figure adapted from [7].

1-3 The Helix Approach

The Helix approach relies on IPC to strategically manipulate the wake behind the excited wind turbine, creating a dynamically actuated helical wake. The IPC mentioned here is defined relative to the collective pitch control, where the pitch of all blades is adjusted simultaneously and uniformly. In IPC, each blade's pitch can be adjusted independently, allowing for more precise control over the aerodynamic forces on each blade [23].

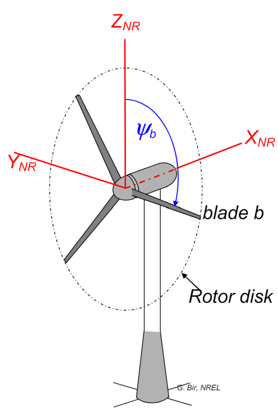

Figure 1-7: Multi-Blades Coordinate (MBC) reference frame relationship. Figure adapted from [24].

MBC Transform The individual blade pitch angles β_i of the turbine are used to generate a directional moment on the rotor. The resulting force vector exerted on the airflow is manipulated thereby continuously changing the direction of the wake [22]. This working mechanism addresses the need to establish a linkage between the blade movement and the rotor movement. Normally, the dynamics of wind turbine rotor blades are generally expressed in the rotating frame attached to the individual blades. The rotor, however, responds as a whole to excitation such as aerodynamic gusts and control inputs in a non-rotating frame. As a result, MBC helps integrate the dynamics of individual blades and express them in a fixed (non-rotating) frame [25].

Fig. 1-7 shows the relationship between the rotational frame (blades) and the non-rotational frame (rotor disk). By defining ψ_i as the azimuth angle of blade i with $\psi = 0°$ indicating the vertical upright position, the blade pitch signals of a three-bladed turbine can be projected to the non-rotating reference frame by Eq. 1-5. In the equation, β_0 represents the cumulative pitch signal, and β_{tilt} and β_{yaw} mean the fixed frame and azimuth-independent tilt and yaw pitch signal respectively:

$$\begin{bmatrix} \beta_{\text{col}}(t) \\ \beta_{\text{tilt}}(t) \\ \beta_{\text{yaw}}(t) \end{bmatrix} = \underbrace{\frac{2}{3} \cdot \begin{bmatrix} 1/2 & 1/2 & 1/2 \\ \cos\psi_1 & \cos\psi_2 & \cos\psi_3 \\ \sin\psi_1 & \sin\psi_2 & \sin\psi_3 \end{bmatrix}}_{T(\omega_r t)} \cdot \begin{bmatrix} \beta_1(t) \\ \beta_2(t) \\ \beta_3(t) \end{bmatrix}. \tag{1-5}$$

As a result, the individual pitch commands β_i can now to computed as decoupled collective, tilt, and yaw pitch commands β_{col}, β_{tilt}, and β_{yaw} respectively, allowing simple Single-Input, Single-Output (SISO) control loops instead of more complex Multiple-Input, Multiple-Output (MIMO) control. Conversely, the pitch angle of individual blades can be acquired based on the collective, tilt, and yaw pitch signal of the rotor in the non-rotational frame by the inverse MBC transformation:

$$\begin{bmatrix} \beta_1(t) \\ \beta_2(t) \\ \beta_3(t) \end{bmatrix} = \underbrace{\begin{bmatrix} 1 & \cos(\psi_1 + \psi_{\text{off}}) & \sin(\psi_1 + \psi_{\text{off}}) \\ 1 & \cos(\psi_2 + \psi_{\text{off}}) & \sin(\psi_2 + \psi_{\text{off}}) \\ 1 & \cos(\psi_3 + \psi_{\text{off}}) & \sin(\psi_3 + \psi_{\text{off}}) \end{bmatrix}}_{T^{-1}(\omega_r t + \psi_{\text{off}})} \cdot \begin{bmatrix} \beta_{\text{col}}(t) \\ \beta_{\text{tilt}}(t) \\ \beta_{\text{yaw}}(t) \end{bmatrix}. \tag{1-6}$$

In Eq. 1-6, the ψ_{off} represents an azimuth offset that compensates for unmodeled actuator delays and blade flexibility. This offset is essential for achieving full decoupling of the tilt and yaw channels [26].

Helix Excitation The helical wake is generated by dynamically manipulating the wake in vertical and horizontal direction respectively over time, i.e. varying tilt and yaw moment of the rotor [22]. From the Eq. 1-6, it can be concluded that this manipulation can be indirectly achieved by using the IPC. As a member of the category of Dynamic Induction Control (DIC) method, finding the optimal time-varying induction settings is a very complex control problem for the Helix approach as well [27]. In the pulse approach, a practical way of finding the actuation signal of DIC is given by sinusoidal input signals on the thrust force C_{t}. This method is called periodic DIC and is also adopted by the Helix approach by superimposing a low-frequent sinusoidal signal on the static collective pitch angles of the turbine [28]. Compared to the pulse approach, the periodic DIC is not directly imposed on the rotor thrust but rather on the blade pitch angle. For practical implementation purposes, the periodic induction signal is confined to a sinusoid [21] [28]. Consequently, the control parameters are reduced to the pitching amplitude and the frequency of excitation f_e [22]. The latter is usually characterized in terms of the Strouhal number St defined in Eq. 1-7 with f_e representing the frequency, D stands for the rotor diameter, and U_∞ stands for the inflow velocity:

$$\mathrm{Str} = \frac{f_\mathrm{e} D}{U_\infty}. \tag{1-7}$$

By using empirical experience, the optimal St is found between 0.2 and 0.4 as recommended by previous work [22] [29]. Subsequently, the optimal f_e can be acquired by solving Eq. 1-7. This leads to the tilt and yaw pitch commands for Helix wake mixing as the following equation shows:

$$\begin{bmatrix} \beta_\mathrm{tilt} \\ \beta_\mathrm{yaw} \end{bmatrix} = \begin{bmatrix} A\sin(\omega_e t) \\ A\sin(\omega_e t \pm \pi/2) \end{bmatrix}. \tag{1-8}$$

The A is the amplitude of Helix excitation, usually no larger than 6 degrees due to practical constraints such as pitch rate limitations. The $\omega_e = 2\pi f_e$ represents the Helix frequency in the unit of [rad/s]. In Eq. 1-8, the collective pitch term, β_col is omitted as it is managed by the collective pitch controller which enhances wind turbine performance by synchronously adjusting the pitch angles of all blades in response to rotor speed feedback, thereby ensuring stable power output and rotor speed [30].

There are two Helix variants distinguished by a phase difference of $\pi/2$ and $-\pi/2$ between the tilt and yaw pitch signals, resulting in a Clockwise (CW) and Counterclockwise (CCW) Helix, respectively. While the actuation frequency in the fixed frame remains identical for both variants, the actual frequency applied by the pitch actuator varies once the tilt and yaw control commands are mapped to the rotating frame. This mapping leads to a Helix frequency in the rotating frame of either $\omega_r \pm \omega_e$ ($1P \pm f_e$), depending on whether the Helix is CW or CCW. This relationship can be derived from Eq. 1-9, where ω_r represents the rotating frequency of the wind turbine and ψ_i^0 is the phase shift originating from the azimuthal position of blade i at time $t = 0$:

$$\begin{aligned} \beta_i &= \beta_\mathrm{col} + \cos(\psi_i)\,\beta_\mathrm{tilt} + \sin(\psi_i)\,\beta_\mathrm{yaw} \\ &= \beta_\mathrm{col} + A\cos(\omega_r t + \psi_i^0)\,\beta_\mathrm{tilt} + A\sin(\omega_r t + \psi_i^0)\,\beta_\mathrm{yaw} \\ &= A\cos(\omega_r t + \psi_i^0)\sin(\omega_e t) + A\sin(\omega_r t + \psi_i^0)\sin(\omega_e t \pm \pi/2) \\ &= A\sin[(\omega_r \pm \omega_e)t + \psi_i^0], \end{aligned} \tag{1-9}$$

Generally, a CCW Helix results in higher farm-level energy gains [22], while the CW Helix is favored for lower damage to the pitch bearing [31], which can be explained by the lower effective actuation frequency of $1P - f_e$. The result of the open-loop feed-forward control scheme for the Helix approach built based on the above analysis is illustrated in Fig. 1-8.

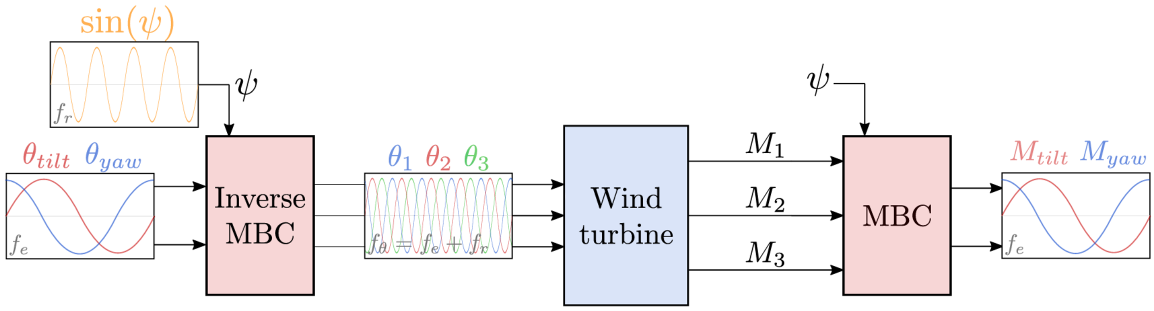

Figure 1-8: A schematic representation of the usage of MBC in the Helix approach. Figure adapt from [22].

Currently, the Helix approach methods have been predominantly studied and implemented in an open-loop configuration. This approach offers the significant advantage of being both fast and easy to implement. However, the absence of feedback information regarding the output wake limits the system's ability to dynamically adjust control strategies in the presence of uncertainties, such as model inaccuracies, wind speed variations, gusts, and shear [7]. Consequently, this configuration reveals a substantial research gap in the closed-loop control of the Helix approach. Addressing this gap serves as the primary motivation for this thesis, guiding the outlining of the research objective and formulation of the research questions.

1-4 Research Questions Formulation

Based on the above analysis, the primary objective of this thesis is to develop a closed-loop control system for the Helix approach. A key distinction between closed-loop and open-loop control is the incorporation of a feedback mechanism. In this context, Light Detection and Ranging (LiDAR) is employed due to its capability to measure flow dynamics, making it suitable for use in feedback systems for wind turbines [12]. When positioned facing downwind, LiDAR provides a valuable source of measurement of the wake generated by the upstream wind turbine. This measurement could be used to provide feedback on the upstream wind turbine. And subsequently, improve our understanding of the wake effects that occur after the implementation of wake management strategies [12]. Furthermore, enabling the effective implementation of closed-loop control schemes, which is required in modeling the relevant wind farm dynamics under the uncertainties concerning inflow estimation and the high complexity nature of the modeling task [32].

Thus, the main research question of this thesis is formulated as:

> *How to integrate LiDAR and the Helix approach for closed-loop wake mixing control for wind farms?*

To support the main research question, three sub-questions have been formulated. The first question addresses the configuration of the LiDAR. Moreover, the LiDAR sample contains extensive information about the Helix. However, it is necessary to selectively focus on specific information about the wake to control for performance improvements. Therefore, the second question addresses the object to be controlled within the Helix and focuses on how to integrate LiDAR with the wind turbine to obtain the necessary information. Answering this question helps identify the control input and the corresponding system output, which is a prerequisite for designing any control system. The third question concerns the integration of the entire system. These questions are defined as follows:

1. *Which LiDAR configuration is most suitable?*
2. *What should be controlled in the Helix?*
   (a) *What specific feature in the helical wake should be controlled?*
   (b) *How can the LiDAR system be designed to obtain real-time data on the target feature?*
3. *How can a control framework be developed to control the Helix in real-time using a closed-loop approach?*

1-5 Overall System Design

The concept of integrating a LiDAR with wind turbines for closed-loop WFFC is not new. For instance, in the study of [33], a downwind-facing LiDAR is employed for wake steering control. In the context of controlling the single wind turbine, the goal of yaw control is to minimize yaw misalignment. This reduction is crucial as it maximizes power production by aligning the turbine optimally with the wind direction. Traditionally, the wind direction signal is measured at one single point by a nacelle-mounted wind vane behind the blades [34]. This generates a potential bias in the measurement because the vane is located in the near wake of the rotor, leading to a steady state yaw misalignment that the controller will not be able to account for [12]. As a result, LiDAR can be used to eliminate this yaw misalignment. In the work of [34], a yaw misalignment of 0.7° was found by using LiDAR recorded field test data. The application of using a yaw controller integrating with LiDAR to mitigate this yaw misalignment is further been explored in a field test demonstrated in [35], from which the result of a 2.4% increase in the annual energy production was found.

Inspired by the work of [33], the overall system is designed to have two subsystems:

- **The LiDAR Subsystem** Consists a LiDAR facing downwind and a supporting pipeline for data processing. The design should fulfill two functionalities in real-time:
  - Wake data sampling.
  - Wake feature acquisition.
- **The Control Subsystem** Consists of a controller and the supporting components for the sack of closed-loop control. The design should fulfill the functionality of:
  - Rectify the Helix based on the current output of the system and the given reference.

Consequently, the block diagram of the overall system is constructed as shown in Fig. 1-9. The next chapter focuses specifically on the LiDAR subsystem, while Chapter 3 addresses the control subsystem.

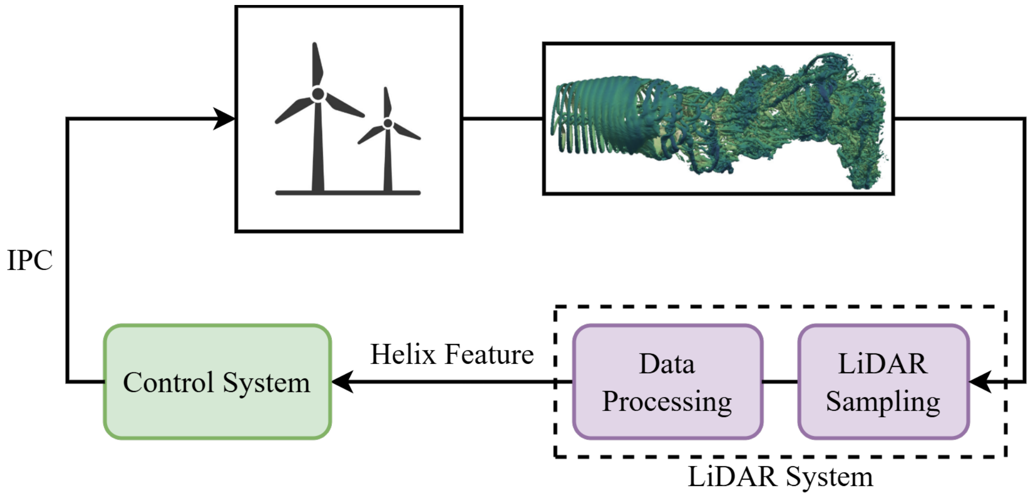

Figure 1-9: The block diagram of the overall closed-loop control system consisting of the LiDAR subsystem and control subsystem. This design is inspired by the work of [33].

1-6 Thesis Structure

The structure of this thesis is outlined as follows. In **Chapter 2**, the LiDAR subsystem system design is presented, detailing the LiDAR setup, Helix feature acquisition, and the Helix frame transformation. These components are essential for addressing the first and second sub-questions of the main research question. Additionally, the entire pipeline for data sampling and processing is constructed. In **Chapter 3**, the control system is designed based on the Smith Predictor to manage output delay. System identification is performed to derive an internal model of the MIMO system. Two control strategies are explored: first, by decoupling the MIMO system and controlling it using a decentralized Proportional-Integral-Derivative (PID) controller, and second, by directly controlling the MIMO system with an $\mathcal{H}_\infty$ controller. The closed-loop system is evaluated in **Chapter 4**, where it is tested under various cases and scenarios. Finally, **Chapter 5** presents the conclusions, the limitations of the proposed framework, and corresponding recommendations for future work.

Chapter 2

Light Detection and Ranging (LiDAR) System Design

This chapter begins with introducing some essential basic information about LiDAR and the setup adopted in this work. An examination of the LiDAR sampling results led to the approach of controlling the Helix indirectly by controlling the rotating hub jet. Additionally, the Helix frame transform is presented and applied to map the rotating hub jet into the Helix frame, where it appears static. This chapter concludes with the LiDAR pipeline design, which integrates the aforementioned components to perform data sampling, data processing, hub jet coordinate calculation, and Helix frame transformation.

2-1 LiDAR Configuration Selection

LiDAR, which stands for Light Detection and Ranging, offers a method of remote wind speed measurement. This technique was first demonstrated in the 1970s and has been used in several research applications [36]. The application of LiDAR technology in the wind energy industry has gained more and more attention in recent years [12]. A LiDAR measures the wind speed based on the "Doppler Effect" with different scanning configurations. This will be further looked into in the following content of this chapter. Additionally, this chapter concludes with an explanation of the LiDAR model built for this research, providing the rationale behind the choice, an overview of its technical specifications, and an analysis of the sampling data. The latter is essential in identifying the feature in the Helix wake to be controlled.

2-1-1 LiDAR Measurement Mechanism

When measuring the wind velocity, a LiDAR sends out a laser beam that reflects the LiDAR from particulates in the atmosphere. A comparison of the send and reflected wavelength is then performed, and the Doppler effect is used to derive the wind speed [37]. Fig. 2-1 illustrates the Doppler effect.

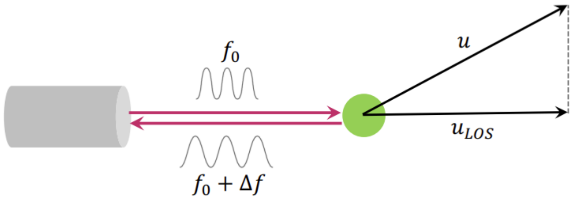

Figure 2-1: Doppler effect of a single beam measurement device. Figure created by Marion Coquelet.

Assume we have a very simple single-direction laser beam measurement device, the original frequency of the Laser beam is f_0, u stands for the speed of the partial, and u_{LOS} is the projection component of u on the line-of-sight of the laser beam. When the laser beam hits the particle, the frequency of the laser beam changes to $f_0 + \Delta f$. As a result, u_{LOS} can be acquired by Eq. 2-1 with c representing the speed of light:

$$u_{\text{LOS}} = \frac{c\Delta f}{2f_0}. \tag{2-1}$$

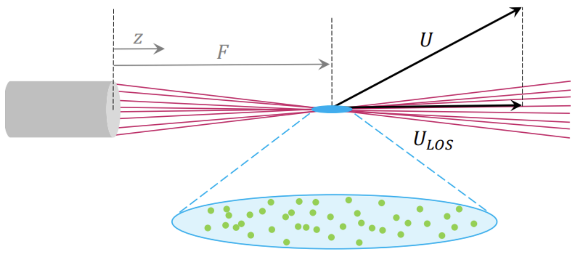

Figure 2-2: Doppler effect of a multi-beams measurement device. Figure created by Marion Coquelet.

The same analysis can be expanded to a multi-beam device as Fig. 2-2 shows. The main difference is that measurement along the beam is also taken into consideration by a weight function. This results in speed measurement of the line-of-sight as Eq. 2-2 shows. $W(z, F)$ symbolizes the weight function, which varies depending on the distance from the laser source to the measurement point up to the focal distance. Consequently, the measured speed of a certain distance is derived as the average weighted sum of measurements taken along this trajectory:

$$u_{\text{LOS}} = \int_{-\infty}^{\infty} \text{W(z, F)} u_{\text{LOS}}(z)dz. \tag{2-2}$$

Fig. 2-3 illustrates examples of weight functions for both continuous-wave LiDAR and pulse LiDAR systems. The peak of each function indicates the primary focal distance, which is the area of greatest interest for data collection. As the distance from this focal point increases, the weighting diminishes progressively and ultimately reduces to zero. This reduction reflects the decreasing relevance of measurements further away from the focal distance.

A bird's view of a nacelle-mounted LiDAR measurement is illustrated in Fig. 2-4. A LiDAR measures the wind speed between the line-of-sight of the laser beam, which can be used to

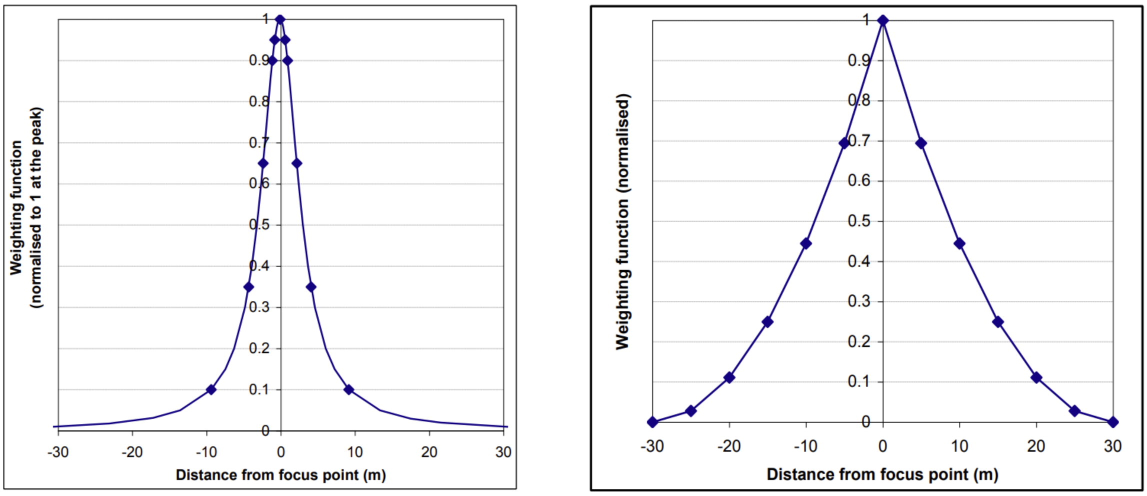

Figure 2-3: Weighting function of a continuous-wave LiDAR (left) and a pulsed LiDAR (right). Figure adapted from [38].

reconstruct the wind velocity. Some studies have been focused on optimizing the LiDAR scanning configuration for different usages. For example, a wider cone angle φ is more desirable when trying to measure wind direction [38].

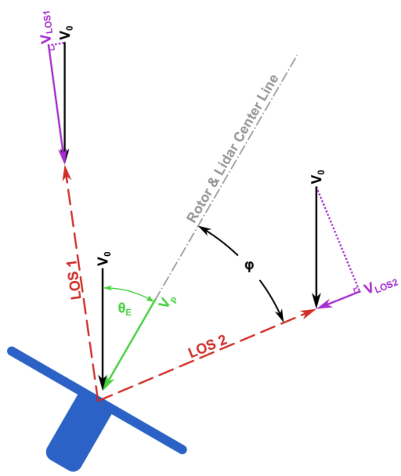

Figure 2-4: Bird view of a nacelle-mounted LiDAR with two LOS beams, V_0 denotes the vector of a uniform wind field while V_p denotes the perpendicular component of the wind corresponding to the rotor disk, φ is defined as the LiDAR's half cone angle. Figure adapted from [12].

2-1-2 Scanning Configuration

Scanning configuration refers to how the laser beam(s) scan the space to get information. There are mainly two types of LiDAR applied in the field of Wind Farm Flow Control (WFFC):

- Continuous-wave LiDAR: A continuous wave LiDAR shoots a continuous beam of light to the atmosphere. A laser beam from a LiDAR system is focused at a predetermined distance ahead, known as the focal distance, where it continuously measures the wind speed. Hence, the LiDAR only measures the wind field information at a specific distance.

- Pulsed LiDAR: The pulsed LiDAR, on the other hand, shoots pulses of light of one particular wave length to the atmosphere. This type of LiDAR uses a timing-based method that records the time it takes for the reflected light to return after a pulse is emitted from the LiDAR. This approach enables the measurement of wind speeds at various distances, or the entire space between the laser source to the focal distance, simultaneously.

The foundational step in constructing a LiDAR model is selecting an appropriate scanning configuration. Continuous-wave LiDAR offers a more economical and eye-safe approach for measuring wind velocity compared to Pulsed LiDAR [39]. Consequently, continuous-wave LiDAR was selected as the preferred scanning configuration for this model. This choice facilitates the LiDAR modeling process in the following chapter.

2-1-3 LiDAR Model

To acquire comprehensive data on the Helix wake, the LiDAR used in this thesis is modeled with the following assumptions:

- A plane can be considered as a collection of many points; when a LiDAR measures information about a plane, it effectively samples data from these individual points by emitting multiple laser beams. Furthermore, it is assumed that these laser beams are emitted simultaneously, with no phase delay among them.
- The half cone angle φ of the LiDAR is configured to encompass the information of the entire plane with the diameter the same as the rotor disk D.
- The weight function $W(z, F)$ is assumed to have a single peak value of 1 at the focal distance while values at other distances are 0.

As discussed in the previous chapter, a LiDAR measures only the line-of-sight speed rather than the absolute speed of a given measurement point, which can be obtained through a simple geometric projection. Specifically, a LiDAR measurement can be modeled as point measurements within the wind field [33]. In the inertial coordinate system, assume the LiDAR measurement point is placed at the origin, the wind vector at point i is denoted by vector $\vec{u_i}$ defined in Eq. 2-3:

$$\vec{u_i} = \begin{bmatrix} u_{i,x} & u_{i,y} & u_{i,z} \end{bmatrix}. \tag{2-3}$$

Assume that the position vector of point i is $\begin{bmatrix} x_i & y_i & z_i \end{bmatrix}$, then the u_{LOS} of measurement point i can be acquired by projecting the wind vector $\vec{u_i}$ onto the normalized laser vector in point i by Eq. 2-4:

$$u_{\text{LOS},i} = \frac{x_i}{f_i} u_{i,x} + \frac{y_i}{f_i} u_{i,y} + \frac{z_i}{f_i} u_{i,z} \tag{2-4}$$

with f_i representing the focus distance defined as:

$$f_i = \sqrt{x_i^2 + y_i^2 + z_i^2}. \tag{2-5}$$

Fig. 2-5 gives a more straightforward take on the LiDAR with the 2-dimensional and 3-dimensional view of the setup. This arrangement is based on the work presented by [33]. In this setup, a LiDAR is mounted on top of the wind turbine nacelle orienting downwind. The LiDAR measures the wind speed information of a plane with the same diameter as the rotor disk with a focal distance of $1D$, shown in both the 2-dimensional and 3-dimensional illustrations.

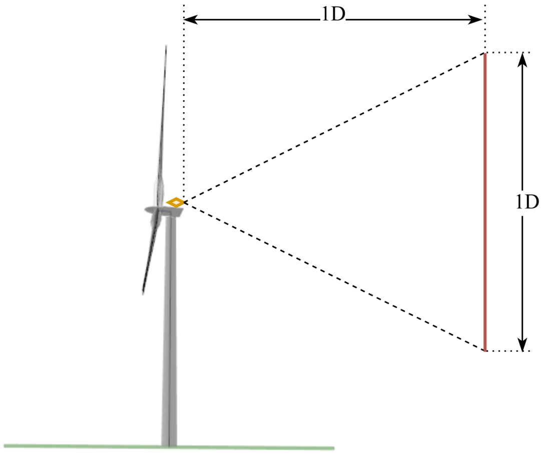

(a) The 2-Dimensional view of the Setup

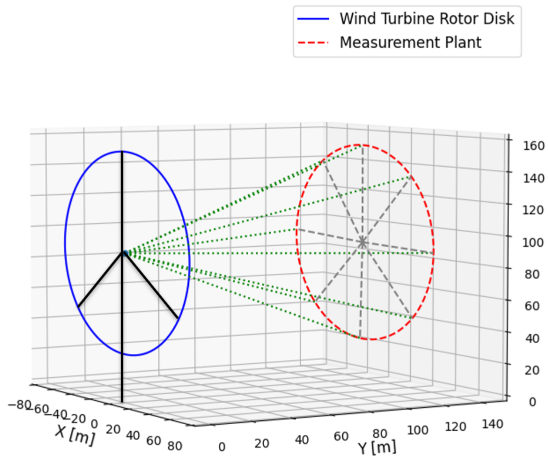

(b) The 3-Dimensional view of the Setup

Figure 2-5: The 2-Dimensional and the 3-Dimensional setup of the LiDAR used in this research.

This chapter provides an overview of LiDAR technology and concludes with the specific LiDAR model utilized in this research. This model has been developed from the ground up within a high-fidelity simulation environment. In the subsequent chapter, the LiDAR sampling results will be examined.

2-2 Helix Feature Identification

The Helix wake exhibits numerous characteristics, making the choice of which property or feature to control a pivotal step in designing the overall system. Accordingly, this chapter addresses the second sub-question of which feature of the Helix wake should be targeted for control. Since closed-loop control for the Helix approach remains uncharted, this study begins by implementing LiDAR sampling functionality within the simulation with the Helix approach being activated to analyze the resulting data. Analysis of the sampling result identifies the hub jet as a promising control target. This is further examined across middle- to high-fidelity levels, validating the concept of controlling the Helix wake via the hub jet. This chapter also introduces the National Renewable Energy Laboratory (NREL)-5MW wind turbine [15] and the QBlade [40] as the object wind turbine of study and the primary simulation tool.

NREL 5-MW Wind Turbine The wind turbine model utilized in this research is the NREL 5-MW baseline wind turbine [15], representing a typical offshore wind turbine in the 5-megawatt range. This model is chosen for two fundamental reasons. First, it is extensively utilized in wind energy research, providing a well-established reference within the field. Second, its simulation speed in the high-fidelity simulation environment is markedly faster than that of larger turbines, such as the IEA 15-MW model, thus enhancing computational efficiency. The technical specifications of the reference turbine are summarized in Table 2-1.

Description	Value
Rated Power	5MW
Rotor Orientation, configuration	Upwind, 3 Blades
Control	Variable Speed, Collective Pitch
Drivetrain	High Speed, Multiple-Stage Gearbox
Gearbox Ratio	97
Rotor, hub Diameter	126m, 3m
Hub Height	90m
Cut-In, Rated, Cut-Out Wind Speeds	3 m/s, 11.4 m/s, 25 m/s
Cut-In, Cut-Out Rotor Speed	6.9 rpm, 12.1 rpm
Rated Tip Speed	80 m/s
Minimum, maximum blade pitch angle	0°, 90°
Max Pitch Rate	$8°/s$
Rated Generator Torque	43093.55 Nm
Maximum Generator Torque	47402.91 Nm
Maximum Generator Torque Rate	15000 Nm/s

Table 2-1: NREL-5MW wind turbine parameters. Data adapted from [15].

QBlade In this study, QBlade is selected as the simulation platform. QBlade is designed as a modular platform incorporating efficient, multi-fidelity solvers for aerodynamic, structural dynamic, and hydrodynamic analyses [40]. Additionally, QBlade employs the free-wake vortex method to simulate turbine wake dynamics [41], making it a more suitable simulation tool for this research compared to lower-fidelity software tools like OpenFAST. The detailed introduction and parameters are covered in Appendix B.

Helix Implementation The parameters regarding the Helix approach that is applied are listed in Table 2-2.

The Helix approach is implemented at below-rated wind conditions, as these conditions lead to more substantial power losses compared to those encountered in above-rated conditions [43]. To support the Helix at the below-rated wind conditions, a $k\omega^2$ torque controller is employed to maintain an optimal Tip Speed Ratio (TSR), maximizing power production. The constant gain k is set as 2.3323 based on the technical report of [15].

LiDAR Sampling Results Figure 2-6 presents LiDAR sampling snapshots over a complete Helix cycle, denoting as T_e. In the figure, the varying colors represent different wind speeds, with brighter colors indicating higher velocities. A notable observation from the figure is the

Description	Value
Inflow Wind Speed	Uniform, 10 m/s
Helix Rotation Orientation	Counterclockwise (CCW)
Strouhal Number	0.3
Turbulence Intensity	0%
Shear Exponent	0.0
Helix Amplitude	3

Table 2-2: Parameter of the Helix simulated. The turbulence properties are defined in the International Electrotechnical Commission (IEC) 61400-1 design standard [42].

presence of a high-speed region rotating at the same frequency f_e as the Helix over time. This feature is known as the hub jet or hub vortex of the wind turbine, existing along the stream-wise direction [44].

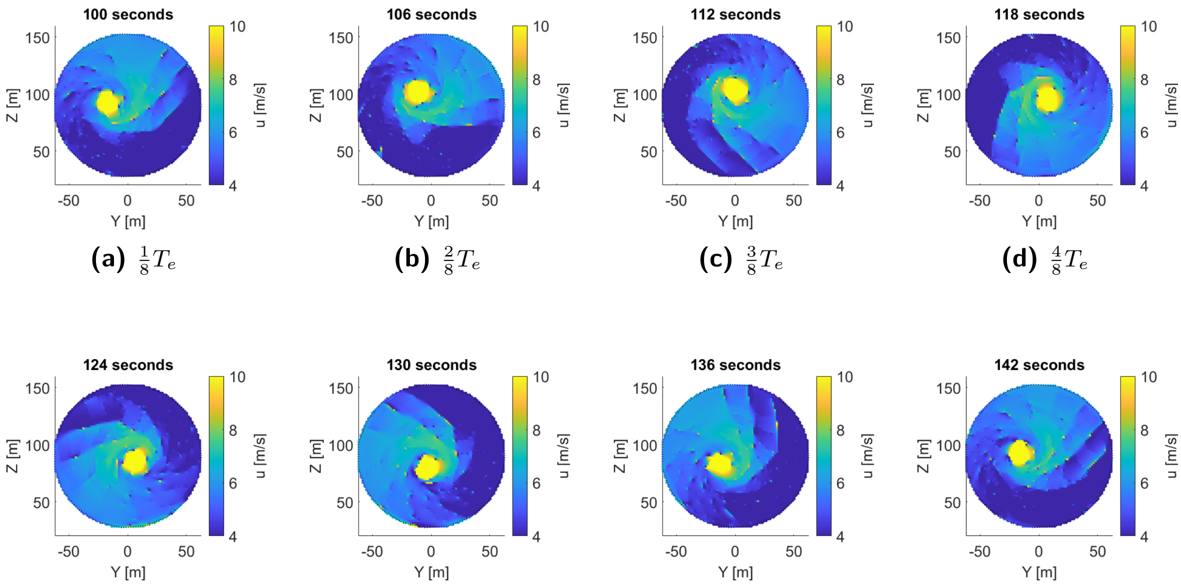

(a) $\frac{1}{8}T_e$ **(b)** $\frac{2}{8}T_e$ **(c)** $\frac{3}{8}T_e$ **(d)** $\frac{4}{8}T_e$

(e) $\frac{5}{8}T_e$ **(f)** $\frac{6}{8}T_e$ **(g)** $\frac{7}{8}T_e$ **(h)** $\frac{8}{8}T_e$

Figure 2-6: LiDAR sampling snapshots over a complete Helix cycle T_e.

The presence of the hub jet can also be confirmed in a high-fidelity Large Eddy Simulation (LES) environment [45], where the Helix approach is applied under identical Helix settings, wind, and turbulence conditions. Figure 2-7 presents a top-down view of the wind turbine flow field, comparing the baseline operation to the case with the Helix approach activated. The varying colors in Fig. 2-7 indicate different wind speeds, with brighter colors representing higher velocities. Two key observations can be made from this figure:

1. The presence of the hub jet, identified by the bright region directly behind the rotor disk, is evident.

2. The rotational behavior of the hub jet is highlighted by the consistent positional shifts of the darker regions.

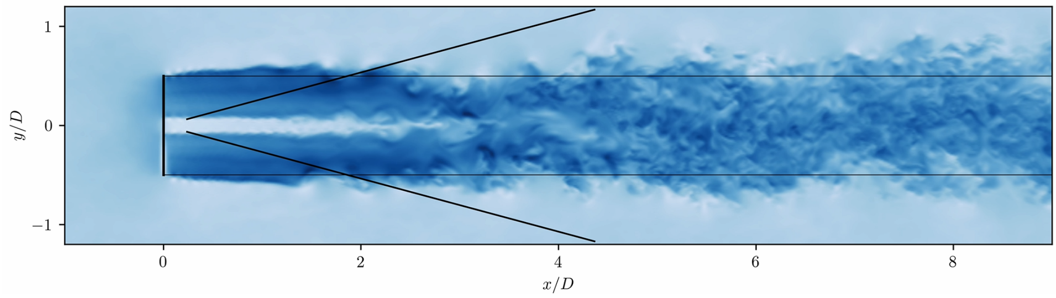

(a) Baseline case

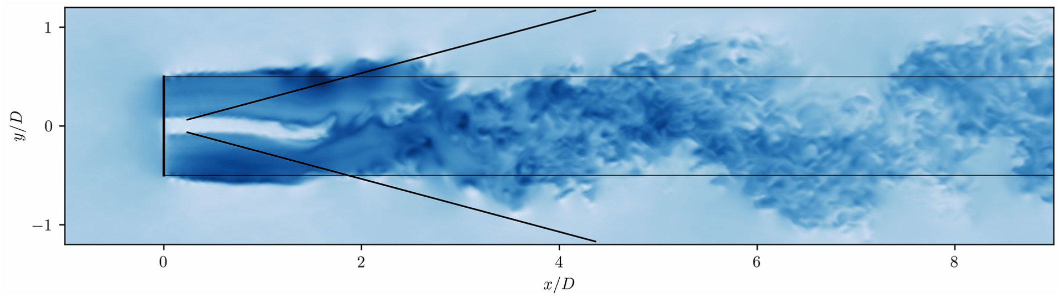

(b) Helix snapshot at $\frac{1}{3}T_e$

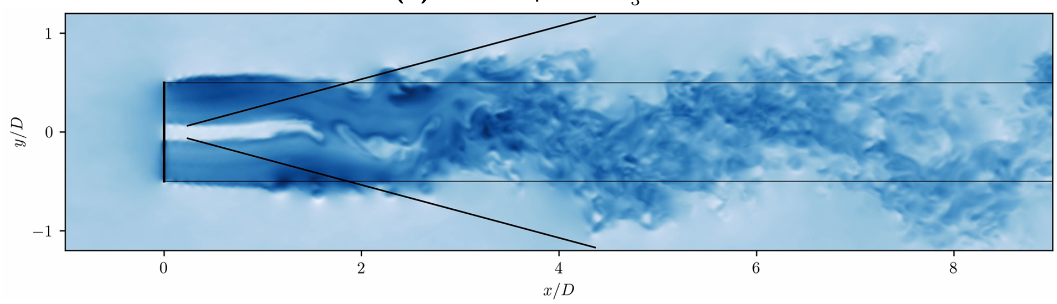

(c) Helix snapshot at $\frac{2}{3}T_e$

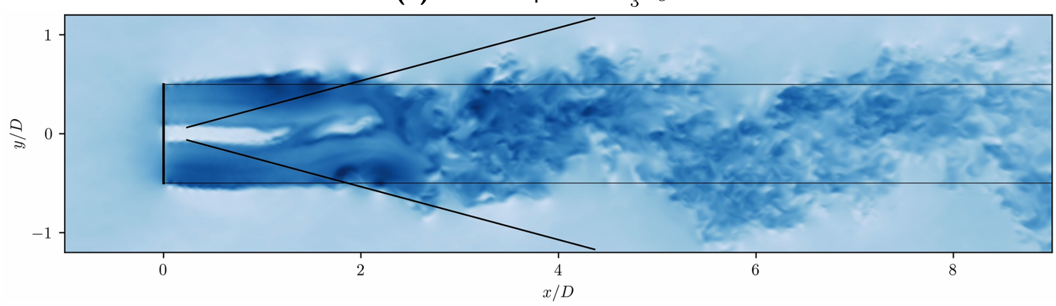

(d) Helix snapshot at $\frac{3}{3}T_e$

Figure 2-7: The bird view of a wind turbine wakes when the Helix approach is activated in LES. Figure adapted from [46].

This illustration confirms that the hub jet is also present in the high-fidelity simulation, suggesting that the controlled feature is intrinsic to the Helix structure.

To validate the hypothesis that controlling the hub jet equates to controlling the Helix, it is essential to confirm a strong link between the movement of the hub jet and the dynamics of the Helix. As discussed in Chapter 1 on the Helix approach, the primary controllable parameters are frequency and amplitude, which are adjusted through the Strouhal number St and Helix amplitude. Thus, if the hub jet reliably reflects these two parameters, it would support the assumption. To examine this, a series of cases were conducted and analyzed. The coordinates of the hub jet are determined by isolating the high-speed region and calculating the average position of the filtered points.

The initial investigation focuses on whether the hub jet can accurately reflect the Helix amplitude. Figure 2-8 presents the result of the hub jet coordinate in the fixed Frame. In this case, the Strouhal number is held constant at 0.3 while the Helix amplitude is incrementally increased from the baseline case (with no Helix generated) up to an amplitude of 4.

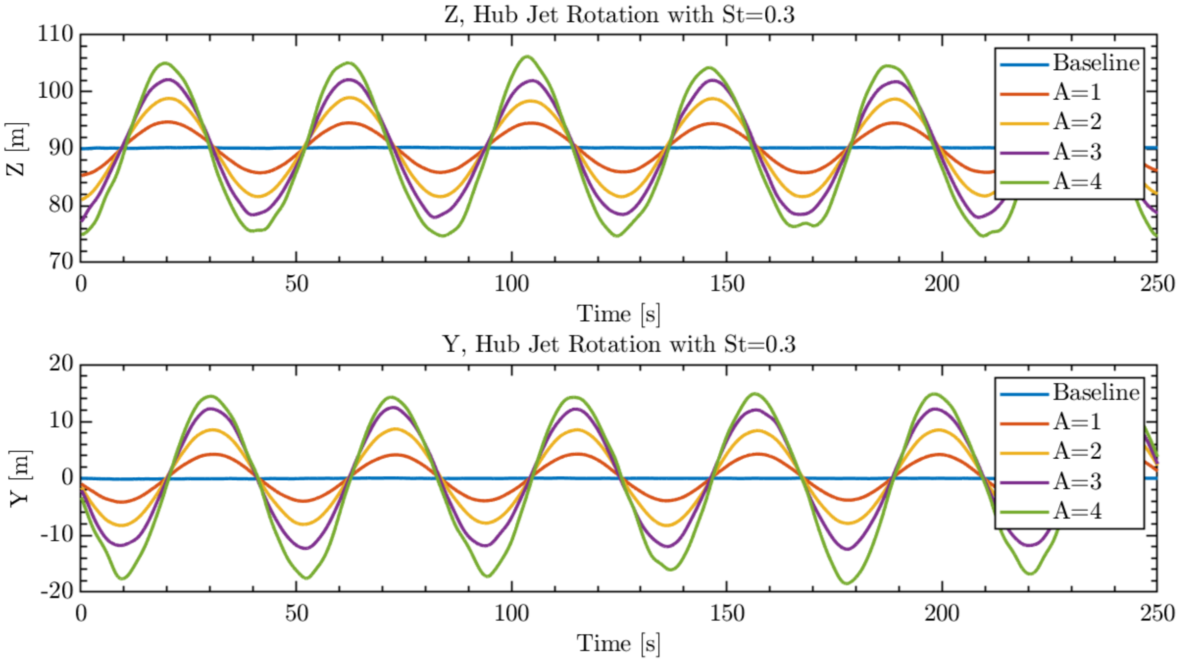

Figure 2-8: Y and Z coordinate of the hub jet when the Strouhal number is held constant $\mathrm{St} = 0.3$ while the Helix amplitude is changing.

and the Fast-Fourier Transform (FFT) of these signals are illustrated in Fig. 2-9

Figure 2-8 and 2-9 indicate that variations in Helix amplitude are indeed reflected in the magnitude of the hub jet's rotation, while the frequency characteristics of the Helix remain consistently accurate. This is evidenced by the identical peak frequency across all cases, matching the frequency of the Helix.

In the second case, the Helix amplitude is held constant at a value of 3, while the Strouhal number is gradually increased from 0.2 to 0.4. This case is designed to assess whether the hub jet can accurately reflect the Helix frequency information. Figure 2-10 first demonstrates the coordinate of the hub jet with changing Strouhal number

and the FFT of these signals are illustrated in Fig. 2-11

The results in Fig. 2-10 and 2-11 demonstrate that all peaks in the FFT analysis of the hub jet align with the calculated Helix frequency, confirming the successful capture of the Helix's

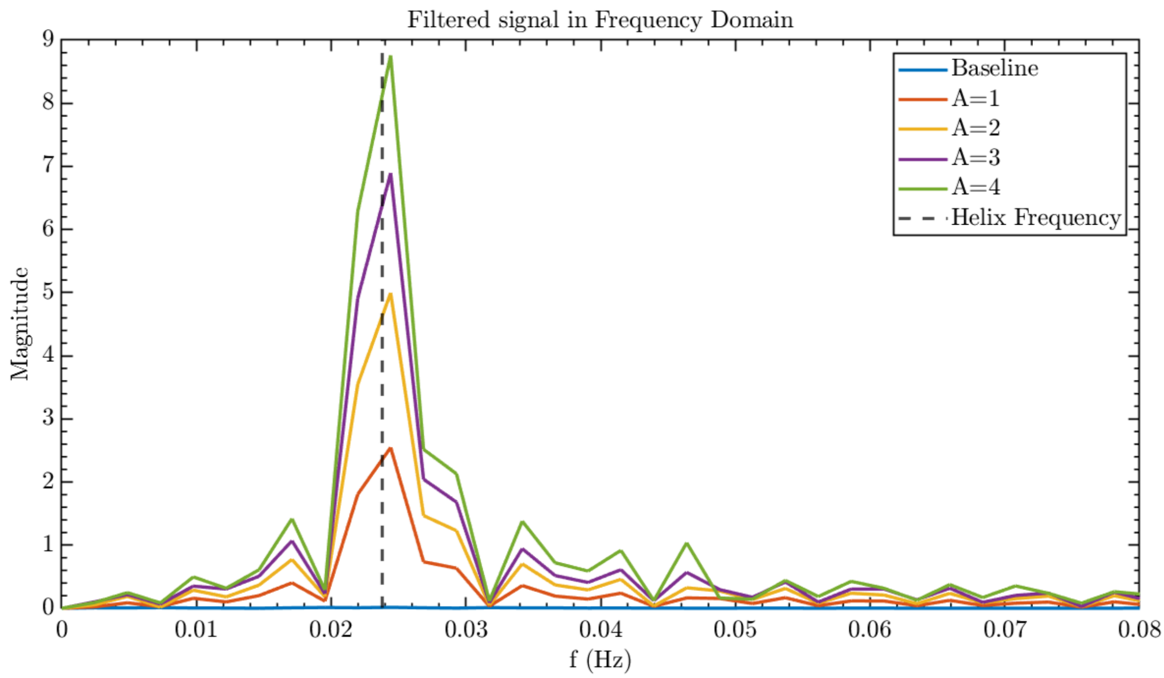

Figure 2-9: FFT of the hub jet coordinate when the Strouhal number is held constant $\mathrm{St} = 0.3$ while the Helix amplitude is changing.

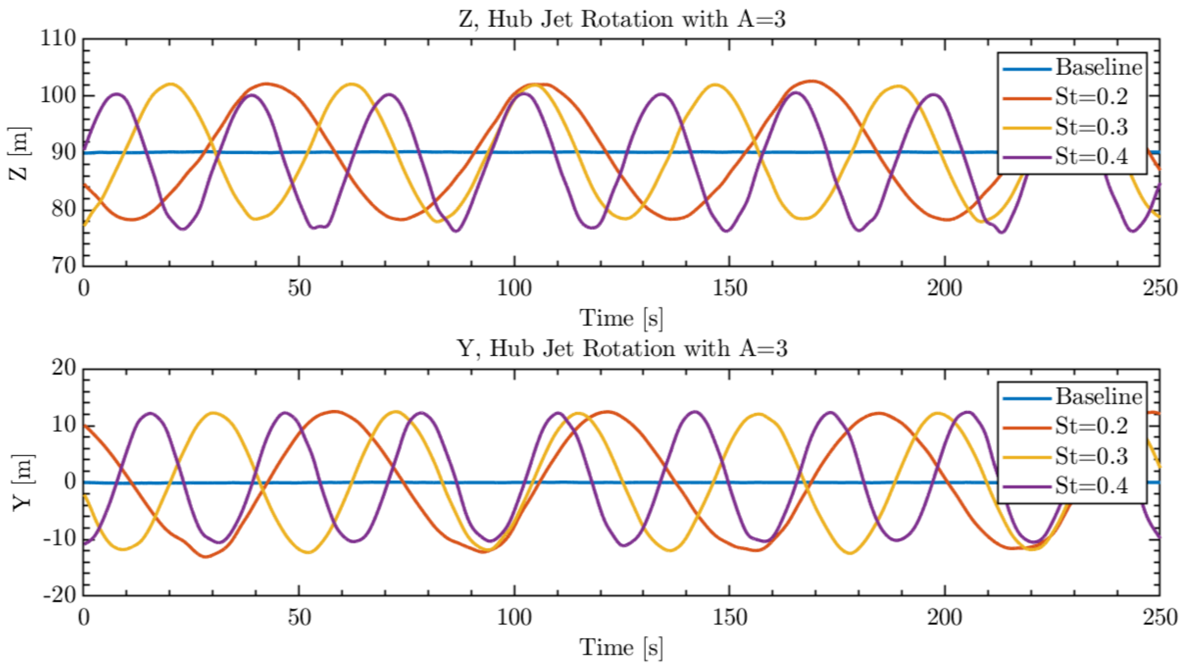

Figure 2-10: Y and Z coordinate of the hub jet when the Helix amplitude is held constant $A = 3$ while the Strouhal number is changing.

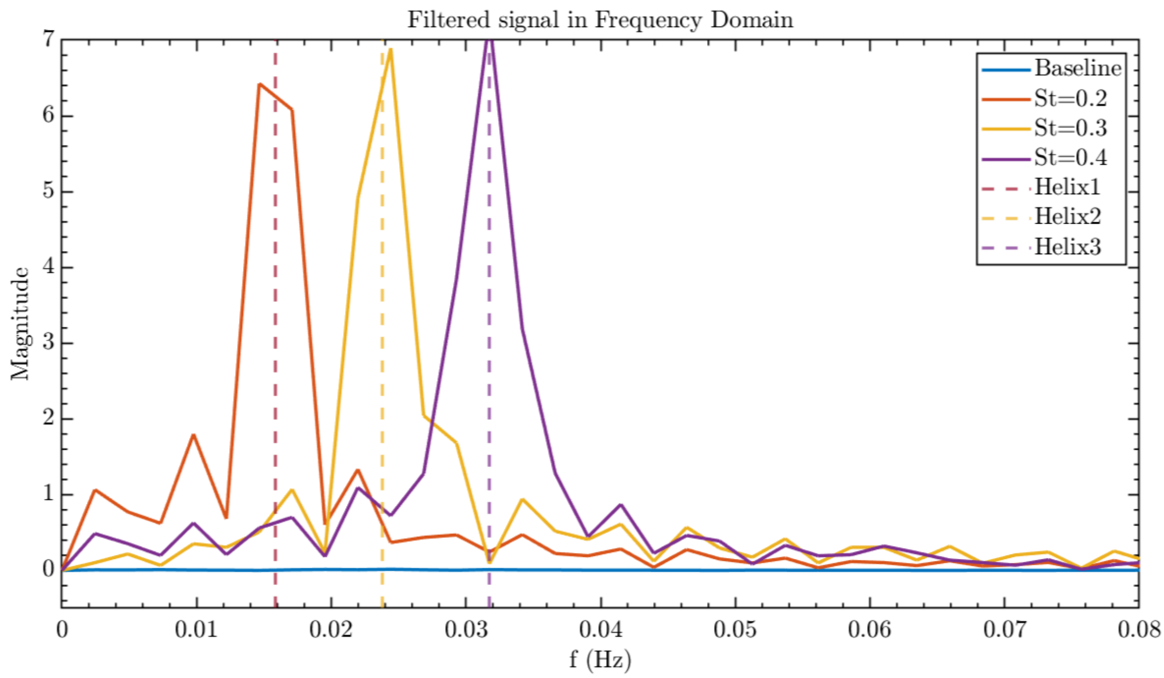

Figure 2-11: FFT of the hub jet coordinate when the Helix amplitude is held constant $A = 3$ while the Strouhal number is changing.

frequency characteristics. Thus, the initial assumption that controlling the hub jet equates to controlling the Helix is validated. Additionally, since the hub jet is a high-speed region within the wake, it can be easily identified through filtering.

In this chapter, the hub jet has been identified as a viable control target, addressing the second sub-question of this research. For simplicity, this thesis focuses on controlling only the Helix amplitude, or equivalently, the magnitude of the hub jet. A defining characteristic of the hub jet is its continuous rotation relative to the fixed frame. Although this rotation frequency is fixed at the Helix frequency of f_e, the rotational behavior can complicate the control problem significantly. This challenge motivates the development of the Helix Frame Transform, introduced in Chapter 2-3.

2-3 Helix Frame Transform

As introduced in the previous chapter, the rotational nature of the hub jet complicates the control process. However, if a mapping can be established from the fixed frame to the Helix frame, that rotates with the Helix in which the hub jet becomes relatively stationary, the control task can be greatly simplified. For instance, reference tracking could then target a static reference rather than a rotating trajectory.

To achieve this, the principle of modulation-demodulation is applied, transforming the rotating coordinate frame of the pitch control system to the Helix coordinate frame. In other words, the demodulation process shifts the $1P + f_e$ Helix rotation (assuming a CCW Helix) to the DC gain. This mapping relationship distinguishes the Helix frame transform from the conventional Multi-Blades Coordinate (MBC) transformation, which maps signals from the rotating frame to the fixed coordinate frame. In other words, map signal from $1P$ and $1P+f_e$ frequency to DC gain and f_e [47].

The derivation of the Helix frame transform resembles the MBC transform. However, the main difference is that the excitation frequency ω_e is included in Eq. 1-5. Therefore, the Helix Frame Transform is written as:

$$\begin{bmatrix} \beta^e_{\text{col}}(t) \\ \beta^e_{\text{tilt}}(t) \\ \beta^e_{\text{yaw}}(t) \end{bmatrix} = \underbrace{\frac{2}{3} \cdot \begin{bmatrix} 1/2 & 1/2 & 1/2 \\ \cos(\psi_1 + \omega_e t) & \cos(\psi_2 + \omega_e t) & \cos(\psi_3 + \omega_e t) \\ \sin(\psi_1 + \omega_e t) & \sin(\psi_2 + \omega_e t) & \sin(\psi_3 + \omega_e t) \end{bmatrix}}_{T(\omega_r t + \omega_e t)} \cdot \begin{bmatrix} \beta_1(t) \\ \beta_2(t) \\ \beta_3(t) \end{bmatrix}. \tag{2-6}$$

For ease of implementation, it is useful to decouple the transform $T(\omega_r t + \omega_e t)$ [47]. This process starts with the sum of the angles by using the angle sum identity matrix as Eq. 2-7 shows:

$$\begin{bmatrix} \cos(\omega_r t + \omega_e t) \\ \sin(\omega_r t + \omega_e t) \end{bmatrix} = \begin{bmatrix} \cos(\omega_e t) & -\sin(\omega_e t) \\ \sin(\omega_e t) & \cos(\omega_e t) \end{bmatrix} \cdot \begin{bmatrix} \cos(\omega_r t) \\ \sin(\omega_r t) \end{bmatrix}. \tag{2-7}$$

Subsequently, Eq. 2-6 can be rewritten as Eq. 2-8 with $R(\omega_e t)$ being the rotation matrix:

$$\begin{bmatrix} \beta^e_{\text{col}}(t) \\ \beta^e_{\text{tilt}}(t) \\ \beta^e_{\text{yaw}}(t) \end{bmatrix} = \underbrace{\begin{bmatrix} 1 & 0 & 0 \\ 0 & \cos(\omega_e t) & -\sin(\omega_e t) \\ 0 & \sin(\omega_e t) & \cos(\omega_e t) \end{bmatrix}}_{R(\omega_e t)} \times \underbrace{\frac{2}{3} \cdot \begin{bmatrix} 1/2 & 1/2 & 1/2 \\ \cos\psi_1 & \cos\psi_2 & \cos\psi_3 \\ \sin\psi_1 & \sin\psi_2 & \sin\psi_3 \end{bmatrix}}_{T(\omega_r t)} \cdot \begin{bmatrix} \beta_1(t) \\ \beta_2(t) \\ \beta_3(t) \end{bmatrix}. \tag{2-8}$$

As shown in Eq. 2-8, the Helix frame transform is implemented simply by multiplying a rotation matrix $R(\omega_e t)$ to the MBC transformation. This provides an intuitive understanding of the Helix frame transform: it allows the original non-rotating frame to rotate at a frequency of ω_e [rad/s]. Consequently, the hub jet, which was previously rotating, should now appear stationary. Conversely, the inverse Helix frame transformation can be derived as shown in Eq. 2-9. Noted that Azimuth offset ψ_{off} is added in the inverse transform for decoupling the tilt and yaw channels:

$$\begin{bmatrix} \beta_1(t) \\ \beta_2(t) \\ \beta_3(t) \end{bmatrix} = \underbrace{\begin{bmatrix} 1 & \cos(\psi_1 + \psi_{\text{off}}) & \sin(\psi_1 + \psi_{\text{off}}) \\ 1 & \cos(\psi_2 + \psi_{\text{off}}) & \sin(\psi_2 + \psi_{\text{off}}) \\ 1 & \cos(\psi_3 + \psi_{\text{off}}) & \sin(\psi_3 + \psi_{\text{off}}) \end{bmatrix}}_{T^{-1}(\omega_r t + \psi_{\text{off}})} \times \underbrace{\begin{bmatrix} 1 & 0 & 0 \\ 0 & \cos(\omega_e t) & \sin(\omega_e t) \\ 0 & -\sin(\omega_e t) & \cos(\omega_e t) \end{bmatrix}}_{R^{-1}(\omega_e t)} \cdot \begin{bmatrix} \beta^e_{\text{col}}(t) \\ \beta^e_{\text{tilt}}(t) \\ \beta^e_{\text{yaw}}(t) \end{bmatrix}. \tag{2-9}$$

Figure 2-12 and 2-13 illustrate the hub jet in the fixed frame and the Helix frame respectively. It is evident that the hub jet, which previously exhibited rotational motion in the fixed frame, appears stationary in the Helix frame after applying the transformation from Eq. 2-8.

It should be noted that mean centering has been applied to the hub jet coordinates to eliminate extra oscillating components, explained in Appendix A. Additionally, the figure reveals a

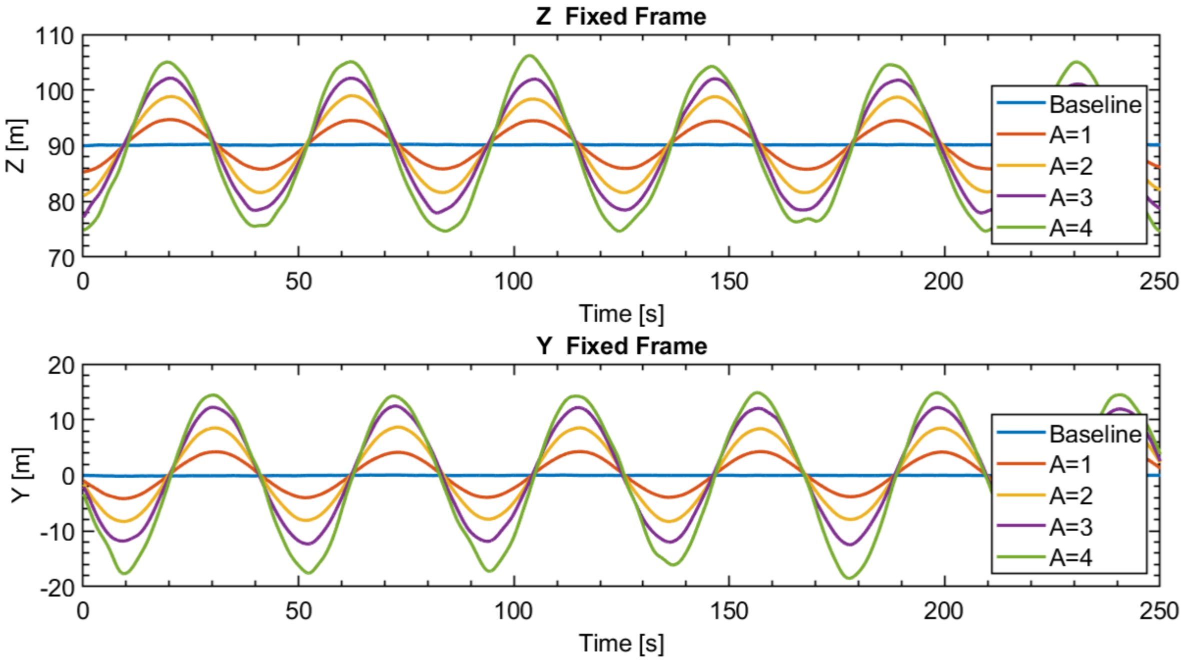

Figure 2-12: The hub jet coordinates in the fixed frame.

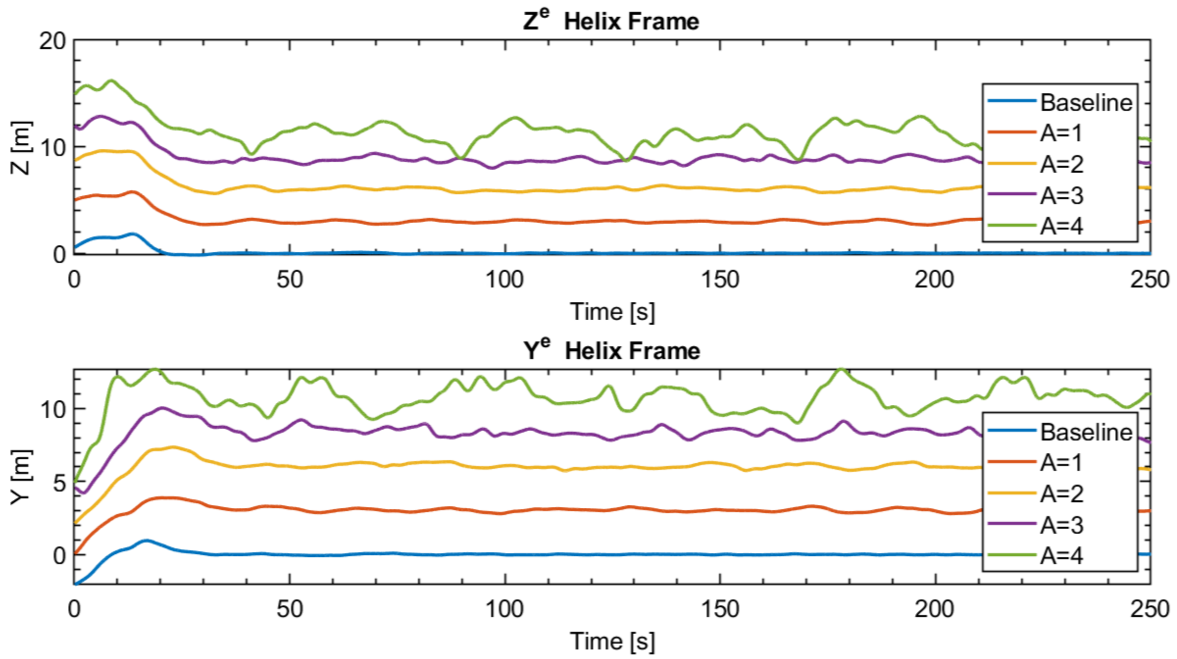

Figure 2-13: The hub jet coordinates in the Helix frame.

positive correlation between the amplitude in the fixed frame and that in the Helix frame. These results confirm the expected functionality of the Helix frame transform.

A similar operation can be applied to the input signals of β_{tilt} and β_{yaw}, converting to β^e_{tilt} and β^e_{yaw} where the sinusoidal signals become steady. Therefore, it can be concluded that the input-output pair $(\beta_{\text{tilt}}, \beta_{\text{yaw}}) \to (z, y)$ can be mapped to $(\beta^e_{\text{tilt}}, \beta^e_{\text{yaw}}) \to (z^e, y^e)$ in the Helix frame via the Helix frame transform. This operation yields a more static representation of the signal, significantly simplifying subsequent control tasks. This transformation, along with the preceding analysis, motivates the development of the overall LiDAR processing pipeline.

2-4 Data Processing Pipeline Design

The above analysis facilitates the design of the flow chart for the data processing pipeline, shown in Fig. 2-14.

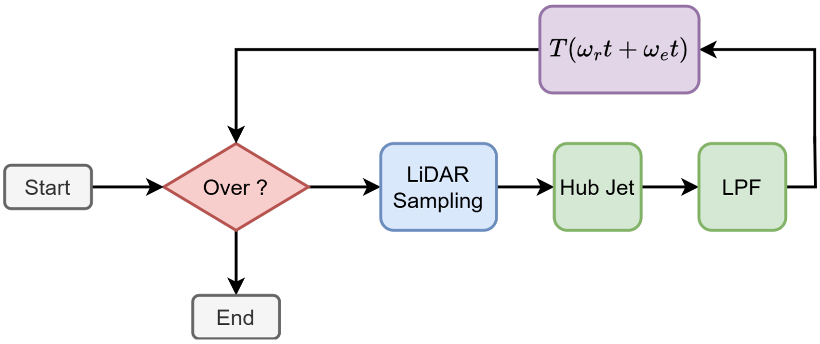

Figure 2-14: Flow chart of the LiDAR subsystem.

The subsystem consists of three parts, the LiDAR sampling, data processing, and Helix frame transform, denoted by the color blue, green, and purple. The functionality of each block is outlined below:

- **LiDAR Sampling**: Capture wind speed data u_{LOS} at the specified focal distance.
- **Data Processing**:
  - **Hub Jet Filter**: Extract the coordinates of the hub jet, (y, z), by isolating the high-speed region and averaging the positions of the filtered points.
  - **Low Pass Filter**: Remove high-frequency noise from the signal. The Finite Impulse Response (FIR) filter is chosen for its desirable properties like guaranteed stability, absence of limit cycles, and linear phase [48]. The filter order is selected as 50 in the trade-off between phase delay and filtering performance, and the cut-off frequency of the low-pass filter is chosen as 0.05 Hz since the Helix is in the frequency of 0.0238 Hz according to Table 2-2.
- **Helix Frame Transform**: Transform the movement of the hub jet from the fixed frame to the Helix frame, where it appears stationary, simplifying control. It is important to note that mean centering is applied to the hub jet data to eliminate additional periodic oscillating components as Appendix A shows.

The overall filtering results are presented in Fig. 2-15 where a Helix configured with the same parameter setting as Table 2-2 is activated during two discrete intervals, specifically from 50 to 150 seconds and from 250 to 350 seconds. Outside of these intervals, the wind turbine operates under standard conditions without Helix engagement. The result demonstrates that the pipeline successfully meets the requirements by mapping the rotating signals from the fixed frame to the Helix frame. While the signal in the Helix frame is not entirely static, likely due to residual noise that the low-pass filter cannot fully eliminate, nonetheless, a clear trend toward a constant value is still observable. Thus, the pipeline functions as intended.

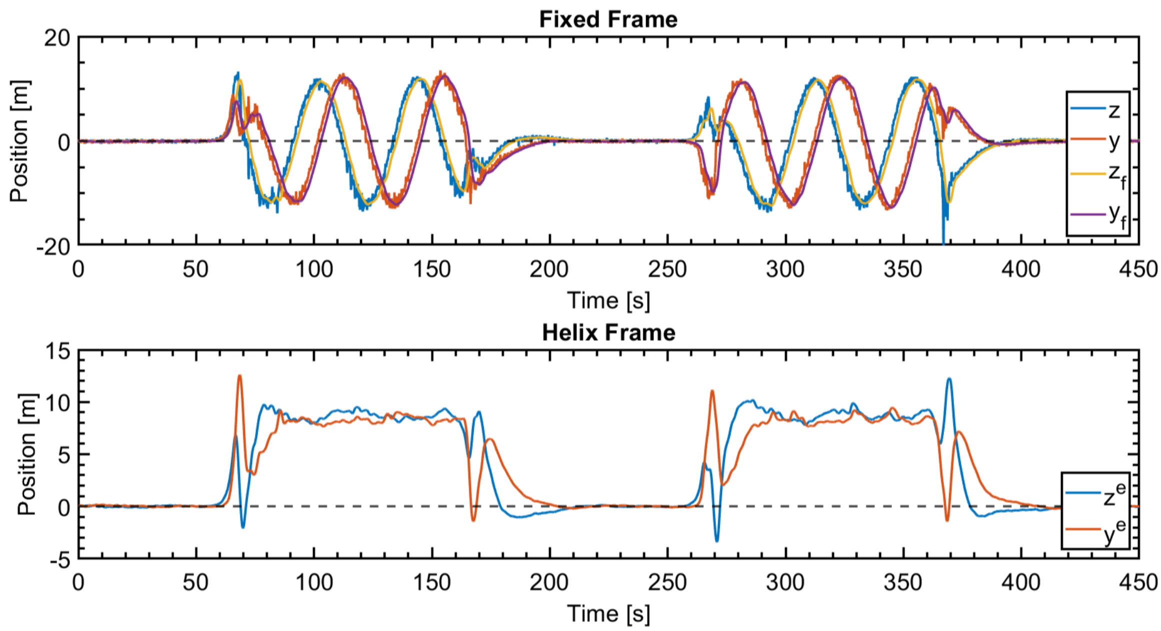

Figure 2-15: Result of a periodic Helix is generated. The top figure displays signals in the fixed frame, while the bottom figure shows signals in the Helix frame. Here, (y, z) denotes the original data, (y_f, z_f) represents the filtered data, and (y^e, z^e) corresponds to data after applying the Helix frame transform.

In this chapter, the LiDAR subsystem is designed and implemented. The LiDAR technology is introduced first. This is followed by an analysis of the sampling data, which supports the selection of the hub jet as a control feature. Several test cases are conducted to validate this idea by demonstrating a strong correlation between the movement of the hub jet and the dynamics of the Helix. Finally, a pipeline is developed to integrate these components into a cohesive system. Using data from the LiDAR system, the control system is designed in Chapter 3.

Chapter 3

Control System Design

This chapter presents the design of the control system, bridging the relation between desired hub jet rotation and blade pitch signal β_i. A feedback controller is therefore designed. Since the reaction of the change in the Helix is measured with a delay τ due to the wake propagation time, the control system has to be designed to overcome this limitation. To manage this delay, the Smith predictor approach [49], grounded in Internal Model Control (IMC) [50], has been utilized.

The following sections of this chapter are planned as below. Chapter 3-1 introduces the concepts of dead-time delay and the Smith predictor and outlines the control block diagram. To enable the Smith predictor approach, system identification is conducted to derive an internal model for the input-output pair $(\beta^e_{\text{tilt}}, \beta^e_{\text{yaw}}) \to (z^e, y^e)$, resulting in a Multiple-Input, Multiple-Output (MIMO) system, with detailed discussion provided in Chapter 3-2. A further study of the system indicates a strong coupling around bandwidth frequency. Consequently, two strategies are explored for controlling the delayed and coupled MIMO system: the decoupled Proportional-Integral-Derivative (PID) control and the $\mathcal{H}_\infty$ control, detailed in Chapters 3-3 and 3-4, respectively. The chapter concludes with a summary of the control system design, synthesizing the overall system, including both the Light Detection and Ranging (LiDAR) and the control subsystem in Chapter 3-5.

3-1 System Delay

In this chapter, the output delay of the system is first looked into. In order to control the system with a delay, a few assumptions are made to simplify the control problem. Subsequently, the Smith predictor based on the IMC strategy is adopted to derive the block diagram of the control system.

3-1-1 Output Delay

One of the challenges for the control system is the existence of a time delay of τ. Specifically, there is a time interval between adjusting the control input of blade pitch signal β_i and measuring the corresponding change of the output y as the wake needs to take time to travel to the measurement location. This delay τ is categorized as the output delay, defined as the delay between the time the system state or output changes and the time this change is observed [51]. As a result, the relationship between the measurement and the output of the wind turbine is characterized by Eq. 3-1 where y_{LiDAR} represents the output of the LiDAR and y_m is the output of the wind turbine:

$$y_{\text{LiDAR}}(t) = y_m(t - \tau). \tag{3-1}$$

The presence of the delay is further illustrated in Fig. 3-1, where the same step response scenario as in Fig. 2-15 is simulated. Consequently, a distinct and constant time interval between the output (dashed line) and LiDAR measurement (solid line) is evident.

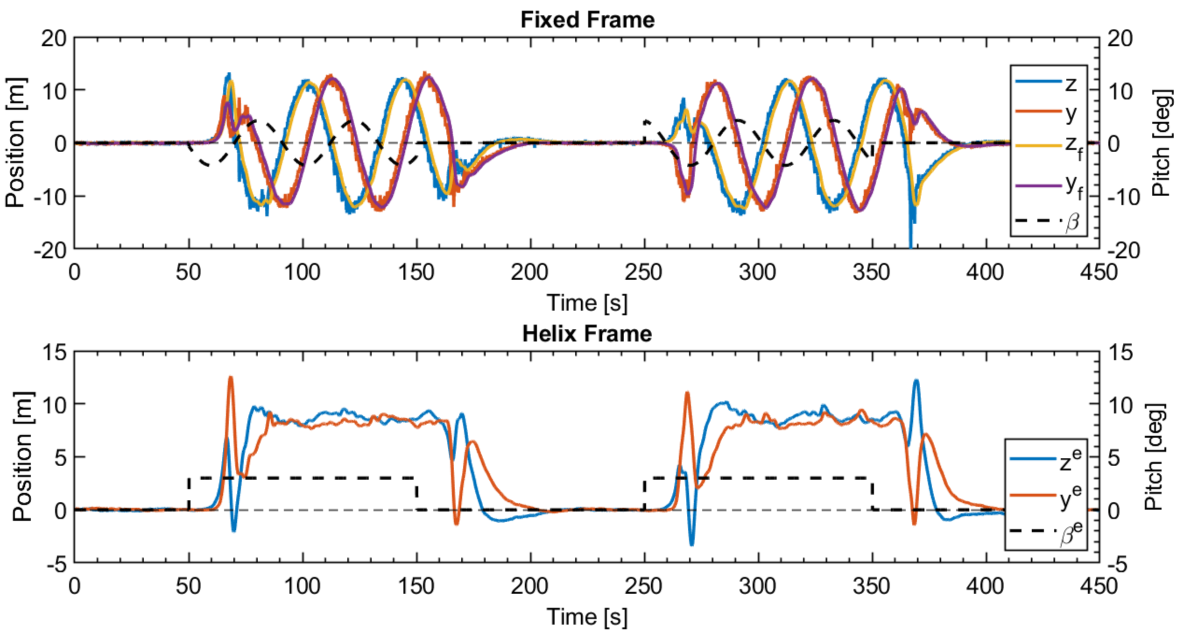

Figure 3-1: Visualization of the output delay τ shown in the system.

For control purposes, three assumptions are made for the delay τ in this research:

- The delay is time-invariant.
- The delay value is assumed to align with Taylor's Frozen Turbulence Hypothesis [52] be only determined by the measurement distance x_{measure} and the average inflow wind speed u_{in} as Eq. 3-2 shows:

$$\tau = \alpha \cdot \frac{x_{\text{measure}}}{u_{\text{in}}}. \tag{3-2}$$

in which α is a constant coefficient for calibrating the value.

- The delay for each output y_i to each input u_j remains the same.

Consequently, the system describing the relationship between $(\beta^e_{\text{tilt}}, \beta^e_{\text{yaw}}) \rightarrow (z^e, y^e)$ is formulated as Eq. 3-3 shows. Note that the delay time $T = \tau \cdot T_s$ is expressed in seconds whereas T_s represents the sampling time of 0.1 seconds

$$\begin{bmatrix} z^e \\ y^e \end{bmatrix} = \underbrace{\begin{bmatrix} G_{11}(z) & G_{12}(z) \\ G_{21}(z) & G_{22}(z) \end{bmatrix} z^{-\tau}}_{\mathbf{G}} \begin{bmatrix} \beta^e_{\text{tilt}} \\ \beta^e_{\text{yaw}} \end{bmatrix}. \tag{3-3}$$

From multiple experiments, a consistent delay time of T is found as $T = 11.2$ seconds. Identifying τ is essential for designing a control system that can effectively stabilize the wind turbine while accounting for the delay. This leads to a control approach based on the structure of the Smith Predictor.

3-1-2 Smith Predictor

Smith Predictor The Smith Predictor was developed to address control challenges in systems with a constant output delay, often referred to as dead-time delay [53]. Fig. 3-2 reveals the structure of the framework in which G denotes a stable, strictly proper rational function representing the delay-free dynamics of the plant, while τ is a positive constant that characterizes the time delay. Furthermore, $\hat{G}$ and $\hat{\tau}$ are nominal plant and delay models respectively, capturing the delay-gree system dynamic and delay information.

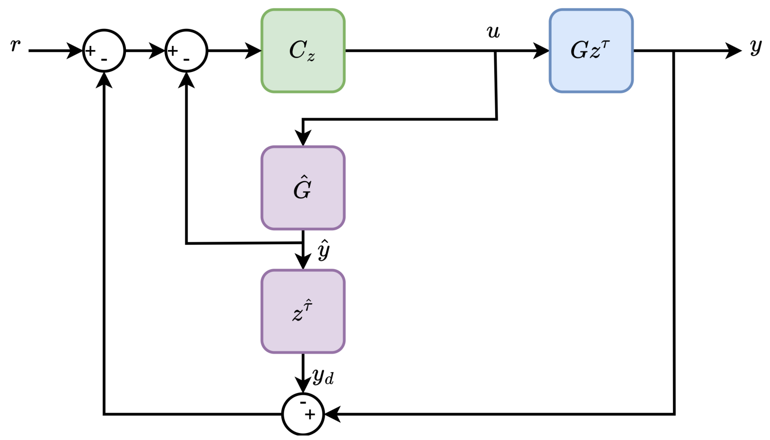

Figure 3-2: The structure of a Smith predictor. Figure adapted by [53].

The nominal model $\hat{G}$ processes the control signal u to produce an estimated undelayed output $\hat{y}$. In addition, a delay factor $z^{\hat{\tau}}$ is applied to estimate the delayed output y_d, which is then subtracted from the actual system output y, isolating the component of the output attributable purely to the system dynamics [53]. This feedback signal is fed into the control loop, allowing the controller to operate as if it were interacting with a delay-free system, canceling out the delay from the control loop. Consequently, the design process is simplified by allowing the primary controller to be designed under the assumption of a delay-free control loop [49]. This approach is adopted in this research and serves as the foundation for developing the general control scheme.

General Block Diagram Inspired by the structure of the Smith Predictor, the designed control scheme is illustrated in Fig. 3-3. It is evident that Fig. 3-3 closely resembles the one presented in Fig. 3-2, with the primary distinction being that the wind turbine replaces the general plant Gz^τ.

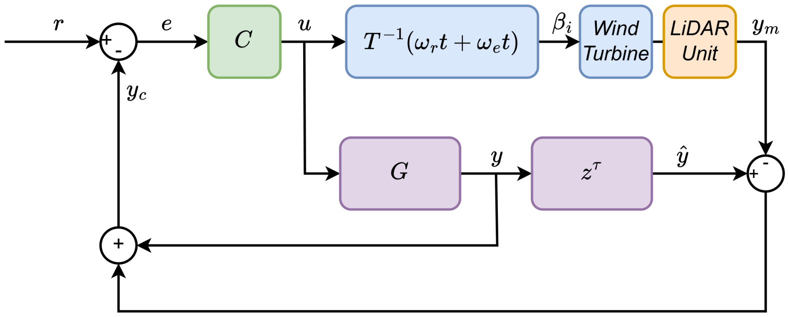

Figure 3-3: The block diagram of the control system. This block diagram is developed under the inspiration of the work of [49] and [33].

The reference signal r is the desired coordinate of the hub jet in the Helix frame, represented by $[z_r^e, y_r^e]^T$. The corresponding control input u denotes the tilt and yaw pitch signal in the Helix frame, expressed as $[\beta^e_{\text{tilt}}, \beta^e_{\text{yaw}}]^T$. However, since the wind turbine cannot directly receive tilt and yaw signals, the inverse Helix frame transformation $T^{-1}(\omega_r t + \omega_e t)$ is applied to convert these inputs into the blade pitch signals β_i. Moreover, the LiDAR unit samples the wind turbine output and converts the hub jet into the Helix frame, as introduced in Chapter 2. The block diagram includes several output signals: y_m represents the actual output of the wind turbine, while y and $\hat{y}$ denote the outputs of the delay-free model and the predicted one respectively. These outputs are subsequently combined into y_c to generate the error signal e by subtracting it from the reference signal r. An alternative construction of the control scheme is shown in Fig. 3-4. The primary distinction lies in replacing the delay factor z^τ with the model Gz^τ that captures the dynamics of the actual wind turbine, offering a different way of implementing the Smith predictor.

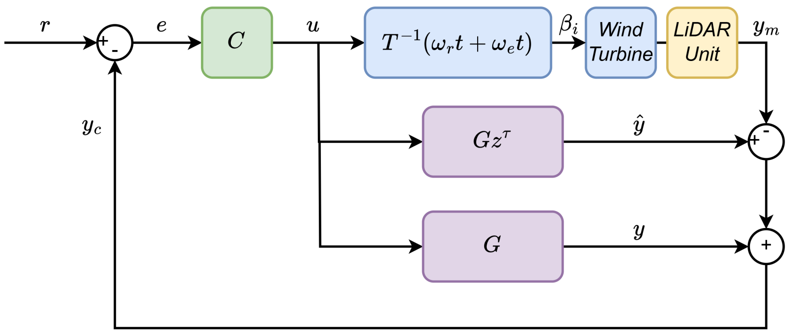

Figure 3-4: An alternative block diagram of the control system.

In this chapter, the system's output delay τ is identified. For control purposes, several assumptions regarding the time delay are established. Following this, the Smith Predictor is examined, based on which the control system's block diagram is developed. The block diagram indicates that an internal model accurately capturing the dynamics of $(\beta^e_{\text{tilt}}, \beta^e_{\text{yaw}}) \rightarrow (z^e, y^e)$

is essential. This requirement facilitates the work of system identification, presented in the following chapter.

3-2 System Identification

System identification is the process of developing mathematical models of dynamic systems based on measured input-output data, enabling the characterization and prediction of system behavior [54]. A typical system identification cycle is illustrated in Fig. 3-5, consisting of four main stages: experiment design, data pre-processing, model fitting, and model validation. This research follows the workflow outlined by this standard cycle strictly. The following sections will discuss each of these stages in detail.

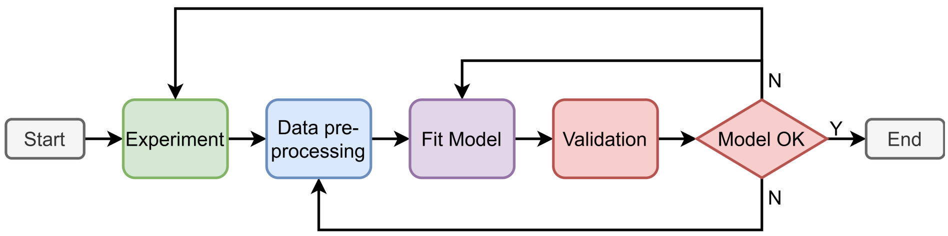

Figure 3-5: Typical system identification cycle. Figure adapted from [54].

Experiment Design The experiment-design considerations rely on the available physical knowledge about the system to be identified [54]. This knowledge will be further used to design important factors about the experiment including the choice of sampling frequency, experiment duration, and input sequence.

According to Shannon's sampling theorem [55], when a band-limited signal with frequency content in the band $[-\omega, \omega]$[rad/s] is sampled with a sampling frequency of $\omega_s = 2\omega$[rad/s], it is possible to reconstruct the signal perfectly from the recorded sample. In system identification, the frequency of interest for the system is primarily around the bandwidth frequency ω_b [54]. Therefore, the system should be excited within the frequency range of $[0, \omega_b]$ [rad/s], and sampling should occur at a minimum frequency of $\omega_s = 2\omega_b$ [rad/s]. Consequently, it is beneficial to have an initial approximation of the system's bandwidth at the outset of the identification process [54], which can be done by using the rise time of the system's step response [56].

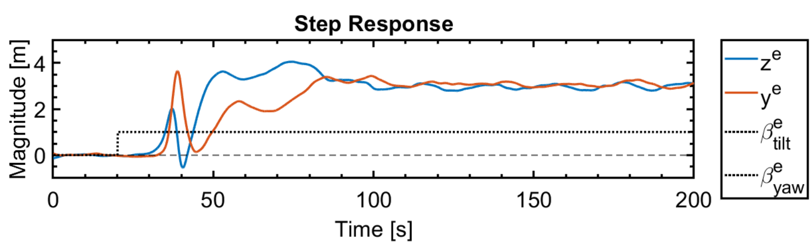

Figure 3-6: The system's step response, where a bandwidth ω_b can be estimated by the rising time.

Figure 3-6 shows the step response of the to-be-identified system. From the figure, a rise time of approximately 25 seconds is observed in both z_e and y_e, leading to an estimated bandwidth of 0.0175Hz. Due to the common rule of thumb of choosing the sampling frequency of approximately $\omega_s = 10\omega_b$ [rad/s] [57], the ideal sampling frequency is 0.175 Hz. However, because the simulation is done iteratively in QBlade, the sampling rate is kept the same as the frequency corresponding to the QBlade simulation time step of 10 Hz.

The Pseudo-Random Binary Noise (PRBN) with a magnitude of 1 is selected as the excitation signal due to its effectiveness in exciting a broad spectrum of system frequencies, facilitating a comprehensive capture of the system's dynamic characteristics [58]. Compared to white-noise, PRBN has a greater resemblance to natural disturbance, whereas white-noise is never found in physical systems for its infinite bandwidth and power [59]. To ensure compatibility with the actuator's bandwidth, the PRBN signal is bandpass-filtered between $[0, 0.03][\text{ Hz}]$. This operation concentrates the input energy around the target bandwidth frequency ω_b, enhancing the system's response quality within the identified frequency range.

Finally, the experiment duration is set to 240 minutes. An Azimuth offset of $\psi_{\text{off}} = 6°$ is used to facilitate decoupling [26]. This value is found in an iterative way that makes the Relative Gain Array (RGA) of the identified system greatly resemble the identity matrix.

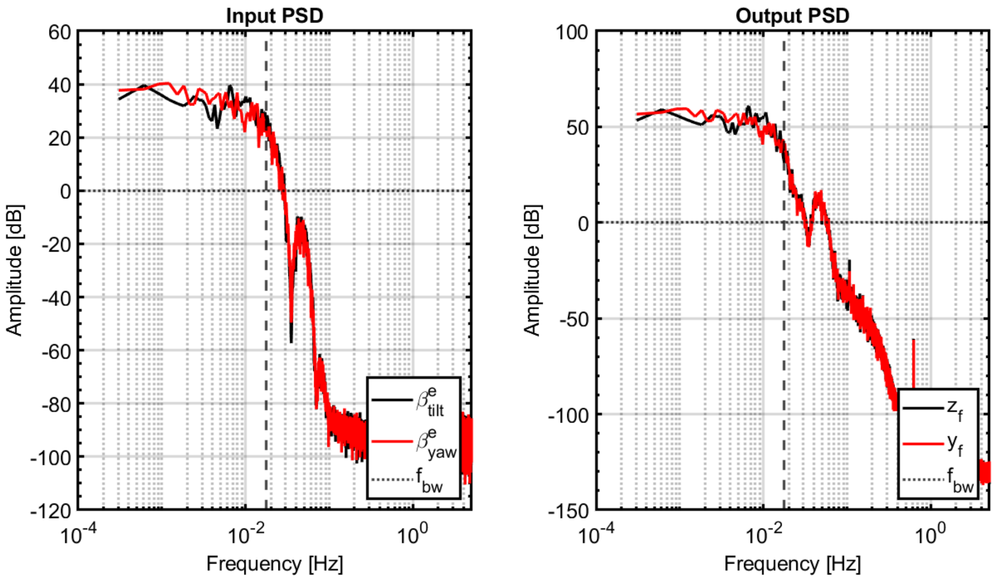

Figure 3-7: Power Spectrum Density (PSD) of both input and output.

Figure 3-7 illustrates the PSD of the input PRBN signal alongside the corresponding output of the wind turbine. As shown, the energy is concentrated within the frequency band $[0, \omega_b]$, aligning with the targeted range for system identification.

Data Pre-processing Following the identification experiment and data collection, the next step is to refine the data to ensure its suitability for system identification. Initially, the first 100 seconds of the raw dataset are excluded to account for wake propagation effects. Moreover, the data is detrended to eliminate any constant offsets. Given that this research employs a linear identification method, the resulting model is Linear Time Invariant (LTI). This means that the identified model is only applicable within a specific operating range. Detrending the data ensures that the model accurately captures the system's dynamic behavior by minimizing the impact of steady-state offsets and trends, thus enhancing model precision within the linear operating range [54].

Model Fit The subsequent step following the data pre-processing is model fit, where an algorithm will be chosen to perform system identification. In this research, the Optimized Predictor-based Subspace Identification (PBSID-opt) is utilized to identify a model. This system identification method is based on the well-established stochastic subspace identification approach, which uses input-output data to estimate a linear model by persistently exciting the system with an input signal containing a wide range of frequencies [47]. The PBSID-opt is selected over output-error parametric model estimation and prediction-error parametric model estimation methods due to its non-parametric nature [54]. Therefore, no prior knowledge of the physical structure is needed for modeling [60]. Moreover, the system model is obtained non-iteratively by solving a number of linear algebra problems rather than conducting non-linear optimizations. Consequently, this approach directly yields a state-space model [54]. Compared to the un-optimized PBSID, PBSID-opt offers improved computational efficiency and reduced estimation error [61]. The sizes of past and future windows are set identically to 200 to achieve a balance among computational speed, noise sensitivity, and accuracy. Analysis of the singular values produced by the PBSID-opt method indicated that a model order of 4 appropriately captures the spectral characteristics of the input-output data. While a higher model order could potentially capture more dynamic detail, an order of 4 was chosen as a balance between model fidelity and computational complexity. The hyperparameters of the system identification method are summarized in Table 3-1.

Description	Value
Method	PBSID-opt
Input Signal Type	PRBN
Input Signal Magnitude	1
Frequency Range	[0, 0.03] Hz
Training set Experiment Length	240 mins
Sampling Rate	10 Hz
Model Order	4
Future Window Size	200
Past Window Size	200
Azimuth Offset	5°
Simulation Time Step	0.1 seconds

Table 3-1: Hyper-parameter for the system identification.

Model Validation and Analysis By adopting the parameters displayed in Table 3-1, a fourth-order LTI system is obtained. The test set is created by exciting the system with a step signal whose magnitude ranges from -1 to 2. For this research, Variance-Account-For (VAF) is selected as an assessment metric. VAF quantifies the percentage of output variance explained by the model, indicating how accurately the model represents the system's behavior. The definition of VAF is shown in Eq. 3-4 in which y and $\hat{y}$ stand for the output of the real plant and the estimated output respectively. As shown in this definition, a high VAF value (close to 100%) suggests that the model accounts for most of the variance in the measured output, indicating a good fit. Conversely, a low VAF value reflects a poorer fit

$$\mathrm{VAF} = (1 - \frac{\mathrm{Var}(y - \hat{y})}{\mathrm{Var}(y)}) \times 100\%. \tag{3-4}$$

The VAF result for the train set and test set is shown in Table 3-2. As shown, the identified model achieves a good fit for both datasets. Additionally, the consistent performance between the training and test sets suggests that overfitting is not an issue as the model generalizes well to new data.

	$\beta^e_{\text{tilt}} \to z^e$	$\beta^e_{\text{yaw}} \to y^e$
Train Set	96.9074%	96.1564%
Test Set	94.9389%	91.5706%

Table 3-2: VAF result of the identified model on train set and test set.

The frequency response of the identified model (orange line) compared with the output of the wind turbine (blue line) is shown in Fig. 3-8. The horizontal dashed line indicates the bandwidth frequency ω_b in the unit of Hz. To calibrate the direction of $(\beta^e_{\text{tilt}}, \beta^e_{\text{yaw}})$ to the direction of (z^e, y^e), a -1 is multiplied by the y_e when identifying the model in consideration of the aerodynamic feature of yaw control.

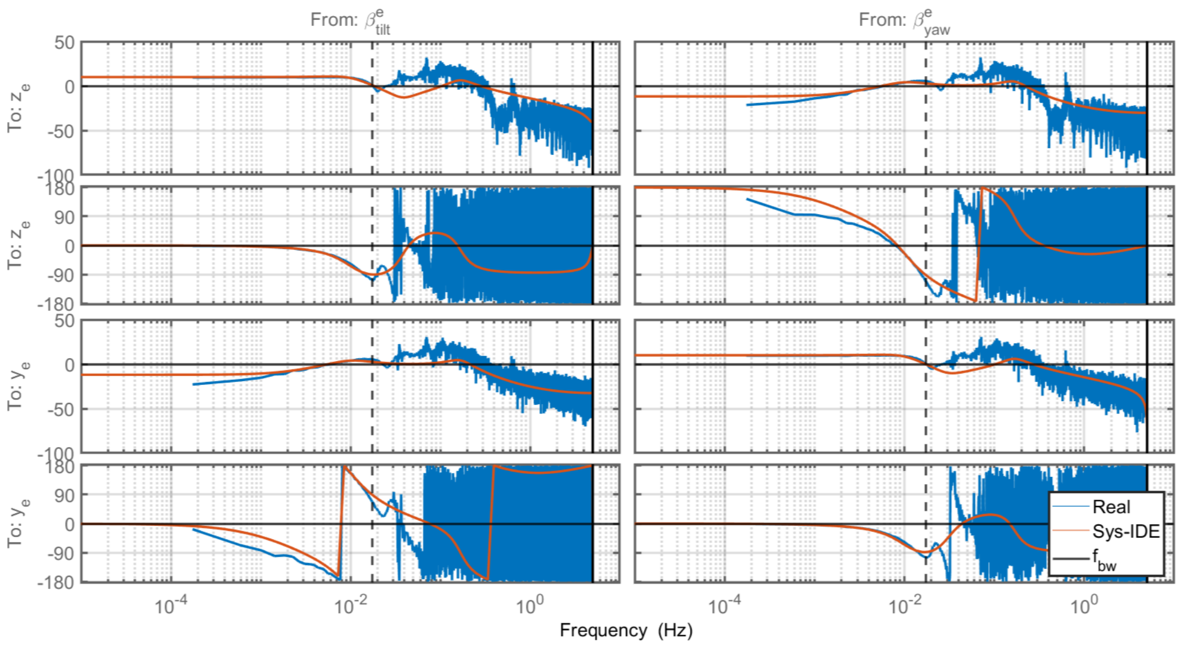

Figure 3-8: Comparison of the PBSID-opt identified model against the spectral averaged input/output data.

There are a few observations from the result of Fig. 3-8:

- First, the identified system successfully captures the system dynamics within the frequency range of $[0, \omega_b]$ [rad/s], while the high-frequency components are not well captured. Generally, the diagonal elements of the system exhibit better dynamic capture compared to the off-diagonal elements, as the former are typically more dominant.

- Second, the difference in steady-state magnitude between the diagonal and off-diagonal transfer functions indicates a degree of decoupling within the system. Specifically, the steady-state gain of G_{11} and G_{22} are positive while those of G_{12} and G_{21} are zero. This implies that β^e_{tilt} influences z^e and β^e_{yaw} influences y^e merely in steady-state frequencies.

The unsuccessful capture of the high-frequency is not problematic, as these frequencies lie outside the range of interest and are not relevant to the control objectives. Additionally, the second observation of the steady-state decoupling can be further supported by the steady-state RGA, which provides a quantitative measure of interaction levels for decentralized control, originally introduced by [62]. Assume a non-singular square matrix G, the definition of steady-state RGA is shown as Eq. 3-5, where G_{ss} represents the steady-state response of G:

$$\text{RGA}(G_{ss}) = \Lambda(G_{ss}) \triangleq G_{ss} \times (G_{ss}^{-1})^T. \tag{3-5}$$

Applying the computation of Eq. 3-5, the steady-state RGA of the identified model is acquired as:

$$\text{RGA}(G_{ss}) = \begin{bmatrix} 0.9935 & 0.0065 \\ 0.0065 & 0.9935 \end{bmatrix}. \tag{3-6}$$

The dominance of the diagonal values and the near-zero values in the off-diagonal elements indicates a strong degree of system decoupling and is desirable for decentralized control. The steady-state RGA also indicates that the process of selecting weights and shaping the plant for certain MIMO controller design is simplified because of the diagonally dominant value [57]. Nevertheless, the system still displays coupling at the bandwidth frequency ω_b. This is evident from the system response shown in Fig. 3-8 as well as from the RGA of $G(e^{j\omega_b T_s})$ with a value of:

$$\text{RGA}(G(e^{j\omega_b T_s})) = \begin{bmatrix} -1.2780 & 2.2780 \\ 2.2780 & -1.2780 \end{bmatrix}. \tag{3-7}$$

This coupling at the bandwidth frequency introduces several challenges for controller design. Specifically, the interactions between variables complicate the implementation of decentralized control. Additionally, the presence of negative elements in the RGA poses a risk to the stability as instability can occur if the sub-controllers are designed independently, and each incorporates integral action. This instability can occur either when all control loops are closed or if the loop associated with the negative relative gain becomes inactive [57].

In summary, this chapter introduces the system identification process, resulting in a model that effectively captures the system's dynamics with high accuracy. Additionally, the identified MIMO system exhibits decoupling at the steady-state frequency, while showing some coupling at ω_b. The decoupling encourages the work of decentralized controller design, which will be explored in the subsequent chapter.

3-3 Single-Input, Single-Output System Control

The goal of decentralized control is to modify the original MIMO system so that the interaction of the cross-term can be eliminated, resulting in a system whose dynamic is dominated by diagonal elements. This simplifies the controller design as the MIMO system can now be seen as a collection of several Single-Input, Single-Output (SISO) systems [63]. The effective decentralized control for a MIMO system relies on pre-compensation techniques [57]. Therefore, the first section of this chapter details the working mechanism of pre-compensators. Building on this foundation, two types of pre-compensators for static decoupling are investigated: the steady-state W_{ss} and the bandwidth W_{bw}. Finally, these pre-compensators are integrated with the control system for performance evaluation.

3-3-1 Decouple the Multiple-Input, Multiple-Output System

A straightforward approach to MIMO control involves a two-step procedure: First, designing a compensator to address the interactions within the plant G, and then developing a diagonal controller using methods similar to those applied in SISO systems [57].

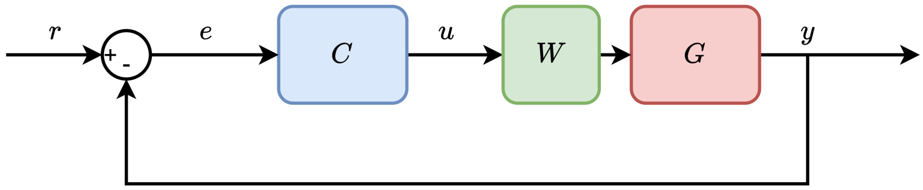

Figure 3-9: One Degree-of-Freedom (DOF) feedback control configuration with a pre-compensator.

Figure 3-9 shows the block diagram after adopting a pre-compensator $W(z)$. This configuration reshapes the plant, resulting in a "new" effective plant as shown in Eq. 3-8. Consequently, the diagonal elements of $G_s(z)$ become the dominant components, while the coupling effects are mitigated:

$$G_s(z) = G(z)W(z). \tag{3-8}$$

Subsequently, a diagonal SISO controller structure can be designed to control the MIMO system $G_s(z)$. For this study, the controller structure looks like Eq. 3-2:

$$\begin{bmatrix} \beta^e_{\text{tilt}} \\ \beta^e_{\text{yaw}} \end{bmatrix} = \begin{bmatrix} C(z) & 0 \\ 0 & C(z) \end{bmatrix} \begin{bmatrix} e_z \\ e_y \end{bmatrix}. \tag{3-9}$$

The choice of the pre-compensator $W(z)$ for decoupling is normally divided into three categories based on the frequency of interest:

- **Dynamic Decoupling** The goal is to make the plant $G_s(z)$ diagonal at all frequencies. Consequently, the pre-compensator is designed as $W(z) = G^{-1}(z)$ so that $G_s(z) = W(z) \cdot G(z) = I$, allowing decentralized control at all frequencies [57].
- **Steady-state Decoupling** Steady-state decoupling only ensures that $G_s(0)$ is diagonal. This is obtained by selecting the pre-compensator as $W(z) = G^{-1}(0)$ so that $G_s(0) = G(0) \cdot G^{-1}(0) = I$.

- **Decoupling at a Specific Frequency** This approach only focuses on one frequency of interest ω_0. Therefore, the goal is to make $G_s(j\omega_0)$ diagonal. The pre-compensator is chosen as $W(z) = G_0^{-1}$ where G_0 is a real approximation of $G(j\omega_0)$ [57].

In this research, dynamic decoupling is not selected due to the non-minimal phase property of $G(z)$. As a result, implementing a dynamic pre-compensator based on the inverse dynamic introduces unstable poles to $G_s(z)$. This complicates the control by inducing instability and imposing constraints on the controller due to the phase lag [57]. Furthermore, dynamic decoupling functions nicely come with the expense of requiring an accurate process model [63]. However, this is not guaranteed in this study. As a result, steady-state decoupling and decoupling at the bandwidth frequency ω_b are attempted. The frequency response of the original system, the system decoupled by the steady-state pre-compensator, and the system decoupled by the bandwidth pre-compensator are presented in Fig. 3-10.

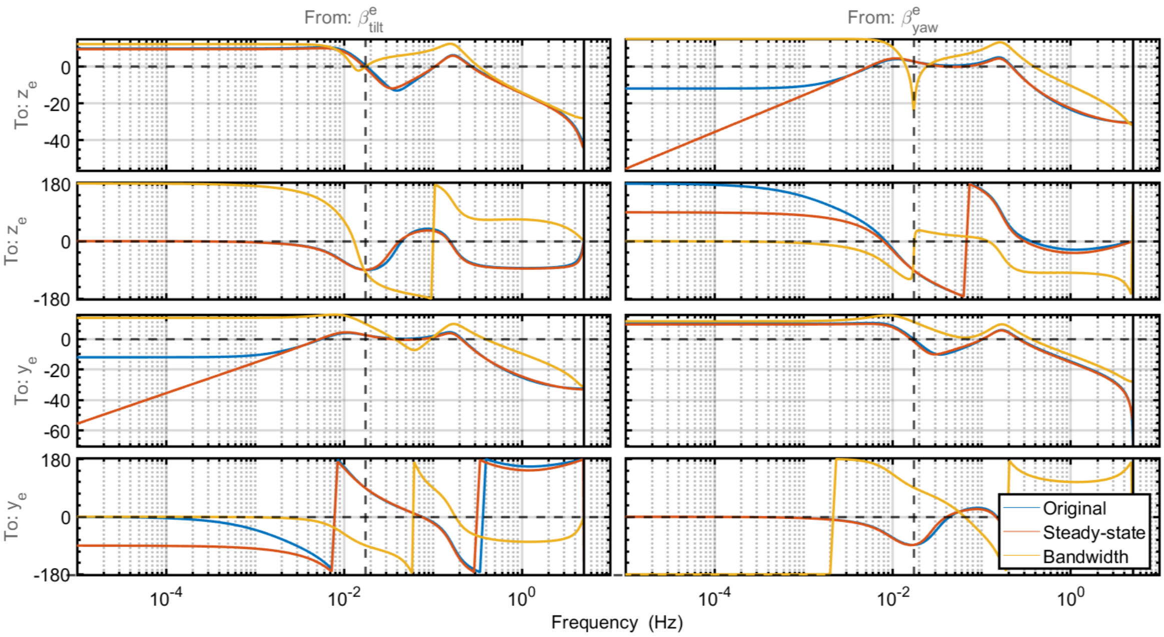

Figure 3-10: Bode plot of the original system and the decoupled system.

Figure 3-10 illustrates the effect of decoupling of the MIMO system through a pre-compensator. Compared to the original system $G(z)$, the steady-state decoupled system $G_{ss}(z)$ exhibits a significantly decreased gain in the non-diagonal elements at the steady-state frequency. Meanwhile, the high-frequency response of $G_{ss}(z)$ remains consistent with that of $G(z)$. This decrease in steady-state gain indicates the successful functioning of the $W_{ss}(z)$. However, $G_{ss}(z)$ still shows a strong coupling of cross-terms at the bandwidth frequency, denoted by the vertical dashed line.

Figure 3-11 illustrates the step response of $G(z)$ and $G_{ss}(z)$. When only β^e_{tilt} is activated. The outputs of $G(z)$ are denoted as $[z^e, y^e]$ while the outputs of $G_{ss}(z)$ are denoted as $[z^e_d, y^e_d]$. Compared to the $G(z)$, z^e in $G_{ss}(z)$ reaches the steady-state value while y^e remains closer to zero.

An expected opposite performance is observed for (z^e, y^e) when only β^e_{yaw} is activated as Fig. 3-12 demonstrates. This indicates the successful decoupling of $G(0)$. Nevertheless, both

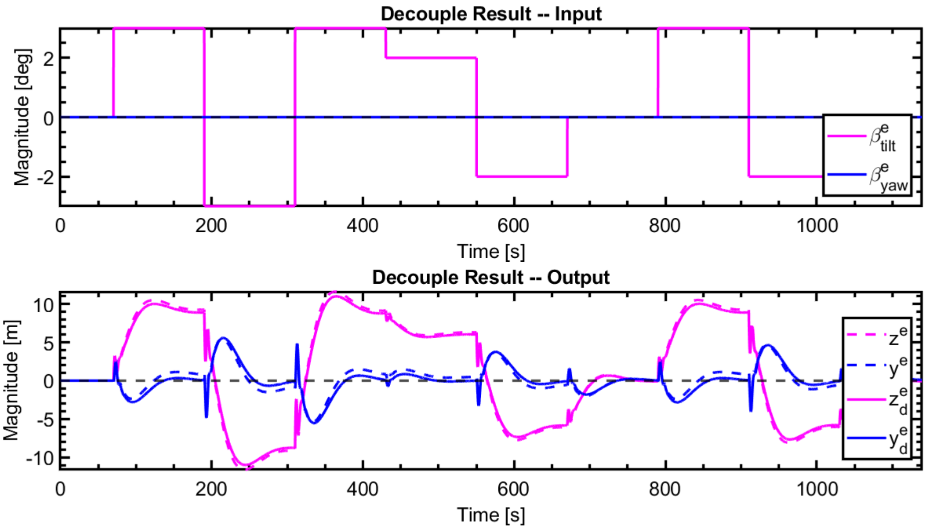

Figure 3-11: Step response of $G_{ss}(z)$ (solid line) compared to $G(z)$ (dash line) when only β^e_{tilt} is functioning.

$\beta^e_{\text{tilt}} \rightarrow y^e$ and $\beta^e_{\text{yaw}} \rightarrow z^e$ still exhibit responses, further supporting the conclusion that only the steady-state frequency is fully decoupled while the other frequency is not.

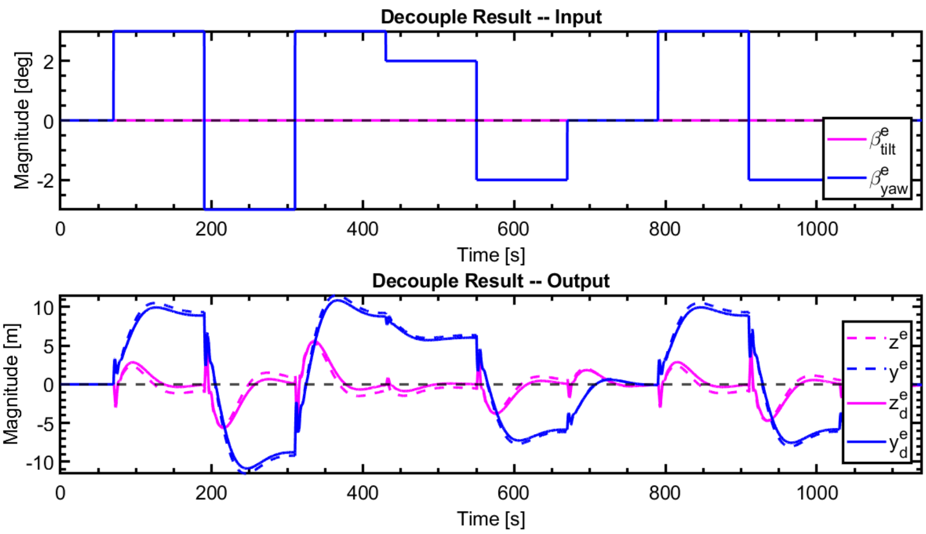

Figure 3-12: Step response of $G_{ss}(z)$ (solid line) compared to $G(z)$ (dash line) when only β^e_{yaw} is functioning.

For $G_{bw}(z)$, the ideal performance would be evidenced by a significant reduction in the gain of the non-diagonal elements of $G_s(j\omega_b)$. While this effect is observed in the $\beta^e_{yaw} \rightarrow z_e$, but not in $\beta^e_{tilt} \rightarrow y_e$. This absence of performance could be attributed to the real approximation of $G_0(j\omega_b)$ used in this study by simply taking the absolute value of the complex number. Despite the simplicity in implementation, this approach omits the phase component of the response, leading to the unsuccessful decoupling of plant $G(z)$. This unsuccessful decoupling effect is further shown in Fig. 3-13 where only the tilt channel is activated.

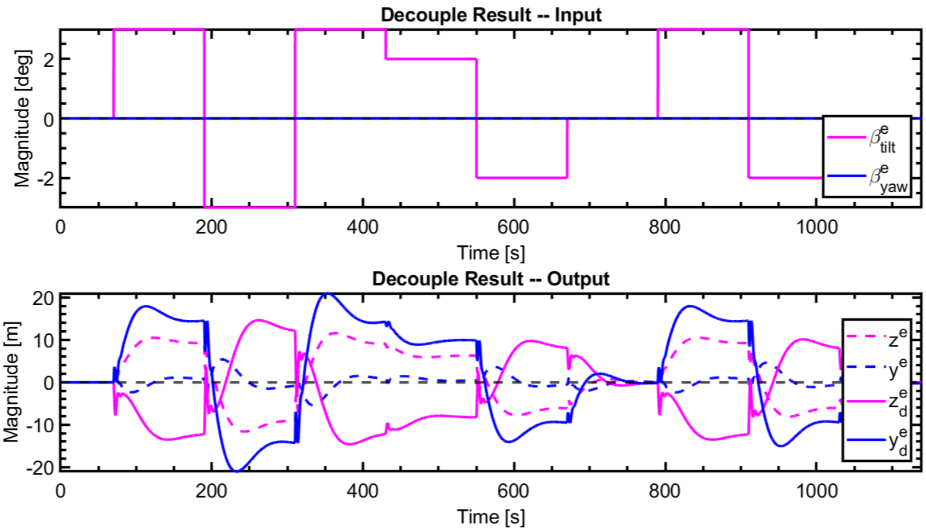

Figure 3-13: Step response of $G_{bw}(z)$ (solid line) compared to $G(z)$ (dash line) when only β^e_{tilt} is activated.

One potential solution is adopting a better real approximation algorithm like the work of [64]. As a result, $G_{ss}(z)$ is selected as the object of study for decentralized control of the original MIMO system.

3-3-2 Decentralized Controller Design

In this chapter, two controllers are designed and implemented for $G_{ss}(z)$ for decentralized control. The primary goal of this study is to follow a reference $r = (z^e_r, y^e_r)$ by adjusting the control input $u = (\beta^e_{\text{tilt}}, \beta^e_{\text{yaw}})$. The step response of the open-loop system indicates linear behavior and inherent stability. This is further confirmed by the positions of poles of $G(z)$ located within the unit circle. This observation indicates that only the steady-state bias needs to be corrected. Consequently, Integral (I) and Proportional-Integral (PI) controllers, defined as Eq. 3-10 shows, are designed for decentralized control. Compared to a simple I controller, the PI is able to handle the response speed additionally through the proportional term, offering more flexibility when regulating the system's response:

$$\begin{aligned} C_{\text{I}}(z) &= K_i \frac{T_s}{z-1} \\ C_{\text{PI}}(z) &= K_p + K_i \frac{T_s}{z-1}. \end{aligned} \tag{3-10}$$

The tuning of the PID controller is achieved through loop shaping. This technique utilizes the open-loop transfer function, defined in Eq. 3-11, to iteratively tune the controller parameters so that the performance objectives of the system are met. Note that only $G_{11}(z)$ is used as an object for the loop shaping given the resemblance of $G_{11}(z)$ and $G_{22}(z)$ in Eq. 3-3:

$$L(z) = C(z)G(z). \tag{3-11}$$

In this study, the controller is tuned so that $L(z)$ satisfies the following three criteria:

1. A Gain Margin (GM) exceeding 6 dB and a Phase Margin (PM) larger than $40°$.
2. High gain at low frequencies and low gain at high frequencies.
3. A crossover frequency ω_c that balances a fast transient response speed with reduced sensitivity to noise.

The first criterion ensures stability and provides sufficient margin in the controller design. The second requirement guarantees the system's performance in reference tracking at low frequencies and disturbance rejection at high frequencies. Consequently, the chosen tuning parameters are provided in Table 3-3. The sampling time of the controller T_s is set to 0.1 seconds, aligning with the configuration of the QBlade simulation. In this study, four PID controllers are designed. Controller I_1 and PI_1 are tuned so that the crossover frequency is placed at $\omega_c \approx 0.5\omega_b$. The controller I_2, on the other hand, was tuned so that $\omega_c < 0.5\omega_b$ so that response speed is sacrificed while emphasizing the stability. Moreover, the controller PI_2 was tuned to achieve faster response speed.

Controller	K_p [deg/m]	K_i [deg^2/(ms)]
I_1	-	0.0206
I_2	-	0.0113
PI_1	0.159	0.0177
PI_2	0.566	0.0337

Table 3-3: Tuned controller parameters by loop shaping.

The corresponding bode plots of the above-mentioned four controllers are given in Fig. 3-14. The two vertical dash lines indicate the bandwidth frequency ω_b and crossover frequency ω_c.

Since the controller has a diagonal structure, the open-loop transfer function $L(z)$ can be written as Eq. 3-12 shows:

$$L(z) = \begin{bmatrix} C(z) & 0 \\ 0 & C(z) \end{bmatrix} \begin{bmatrix} G_{11}(z) & G_{12}(z) \\ G_{21}(z) & G_{22}(z) \end{bmatrix} = \begin{bmatrix} C(z)G_{11}(z) & C(z)G_{12}(z) \\ C(z)G_{21}(z) & C(z)G_{22}(z) \end{bmatrix}. \tag{3-12}$$

Consequently, the property of the open-loop transfer function of $C(z)G_{i,j}(z)$ including crossover frequency ω_c, GM, and PM are listed in Table 3-4.

The results in the table indicate that stability can be achieved through controller I_1, I_2, and PI_1. This can be noticed from all the positive gain margins and phase margins. Some plants indeed have a positive gain margin and a phase margin of infinity. This is treated as a stable system since the infinity of the phase margin implies that the open-loop phase response reaches $-180°$ at no frequency. The controller PI_2 is unable to stabilize the system $G_{21}(z)$. This could be explained by the fact that a larger crossover frequency ω_c brings faster system response, but also introduces a smaller gain margin, and ultimately instability.

The controller PI_1 is selected as $C(z)$ and for the decentralized control implementation as Eq. 3-11 shows. $G(z)$ is only set as the identified model for testing. Figure 3-15 shows

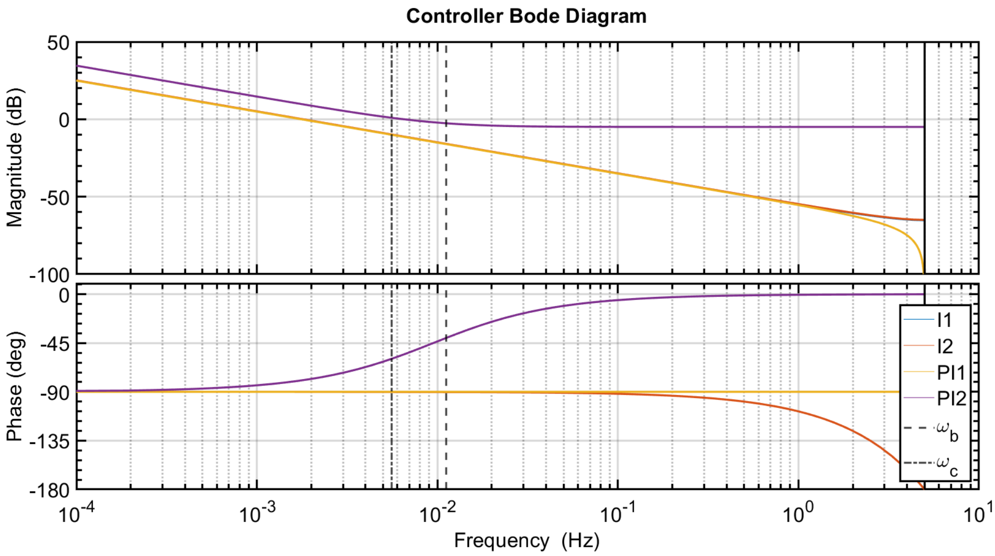

Figure 3-14: Bode diagram of the designed controllers.

Controller	G_{11}			G_{12}		
	ω_c [rad]	GM [dB]	PM [deg]	ω_c [rad]	GM [dB]	PM [deg]
I_1	0.056	14.072	33.159	NaN	11.632	∞
I_2	0.036	18.928	60.034	NaN	10.456	∞
PI_1	0.056	15.521	60.000	NaN	15.536	∞
PI_2	0.089	17.739	60.000	0.095	4.821	68.996
Controller	G_{21}			G_{22}		
	ω_c [rad]	GM [dB]	PM [deg]	ω_c [rad]	GM [dB]	PM [deg]
I_1	NaN	5.599	∞	0.055	45.801	33.211
I_2	NaN	10.456	∞	0.035	50.658	59.343
PI_1	NaN	24.415	∞	0.055	69.605	59.665
PI_2	0.0932	0.981	-106.850	0.085	58.511	59.636

Table 3-4: Key performance index of the decentralized controlled system.

the step response of the MIMO system, from which it can be observed that the closed-loop controlled system is unstable. This instability is likely due to the strong coupling within the MIMO system at the bandwidth frequency ω_b. Moreover, although the poles of individual sub-plant $G_{ij}(z)$ and the plant $G(z)$ are all stable, an analysis of the zeros reveals that the $G_{ij}(z)$ exhibits more unstable zeros compared to $G(z)$. This difference is likely a result of the pole-zero cancellation within $G(z)$. Consequently, when controlling $G_{ij}(z)$ separately, the unstable zeros become prominent, significantly disrupting the system's stability.

This result further supports the fact that checking single-loop margins is inadequate for the MIMO problem [57]. Therefore, despite the system presenting strong decoupling at the steady-state frequency, the decentralized control strategy is unsuccessful. However, since Table 3-4 indicates stability of $[G_{11}, G_{12}]$ and $[G_{21}, G_{22}]$ respectively, another attempt of control is tried where only single channel ($\beta^e_{\text{tilt}} \to z^e$ or $\beta^e_{\text{yaw}} \to y^e$) is controlled. This control approach is referred to as sequential decentralized control in the following content of this thesis.

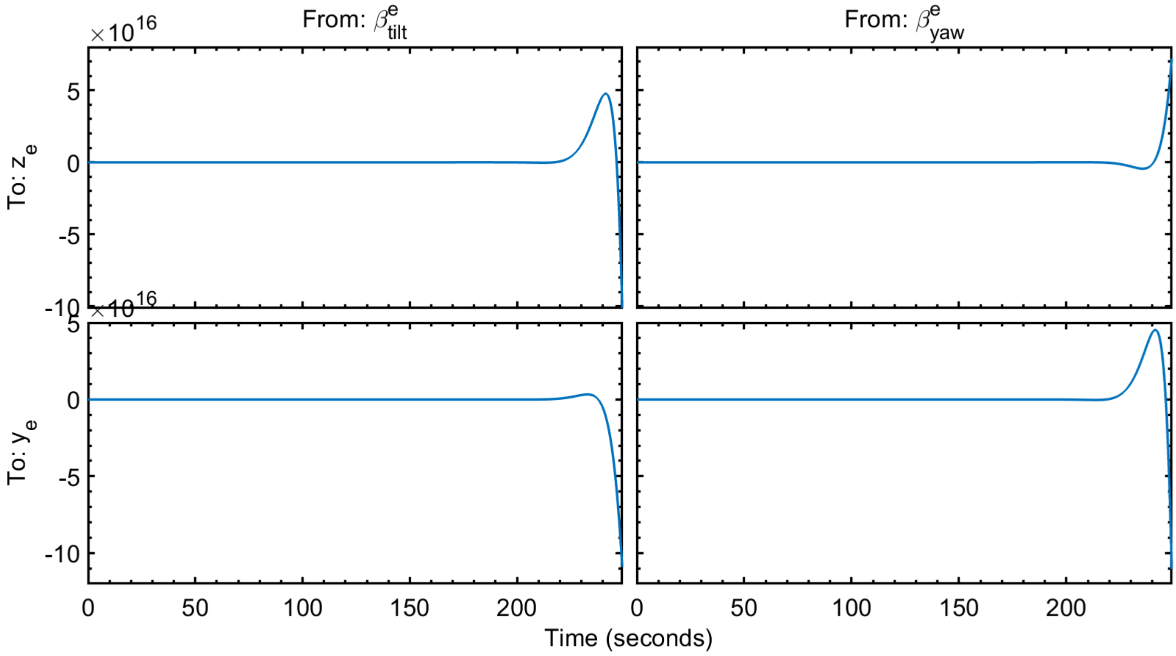

Figure 3-15: Step Response of the MIMO System Controlled by PI_1 as Eq. 3-11.

The open-loop transfer function $L(z)$ when implementing the sequential decentralized control is distinctive from the one shown in Eq. 3-12. Correspondingly, when controlling only $\beta^e_{\text{tilt}} \rightarrow z^e$, the open-loop transfer function $L(z)$ becomes Eq. 3-13:

$$L_1(z) = \begin{bmatrix} C_1(z) & 0 \\ 0 & 0 \end{bmatrix} \begin{bmatrix} G_{11}(z) & G_{12}(z) \\ G_{21}(z) & G_{22}(z) \end{bmatrix} = \begin{bmatrix} C_1(z)G_{11}(z) & C_1(z)G_{12}(z) \\ 0 & 0 \end{bmatrix}. \tag{3-13}$$

Vice versa, controlling only $\beta^e_{\text{yaw}} \rightarrow y^e$ yields the open-loop transfer function $L(z)$ of Eq. 3-14:

$$L_2(z) = \begin{bmatrix} 0 & 0 \\ 0 & C_2(z) \end{bmatrix} \begin{bmatrix} G_{11}(z) & G_{12}(z) \\ G_{21}(z) & G_{22}(z) \end{bmatrix} = \begin{bmatrix} 0 & 0 \\ C_2(z)G_{21}(z) & C_2(z)G_{22}(z) \end{bmatrix}. \tag{3-14}$$

The step responses of L_1 (blue) and L_2 (orange) are shown in Fig. 3-16. This figure demonstrates that the control strategy using individual channels is effective. The success control can be explained by the open-loop transfer function of Eq. 3-13 and 3-14: Controlling the system through individual channels simplifies the MIMO control problem by reducing it to two independent Single-Input, Multiple-Output (SIMO) systems. And due to the inherent stability of $G(z)$, leaving one channel open-loop does not affect overall system stability. Moreover, since one output consistently dominates as shown in Fig. 3-9, each SIMO system resembles a SISO system. This eventually mitigates variable coupling.

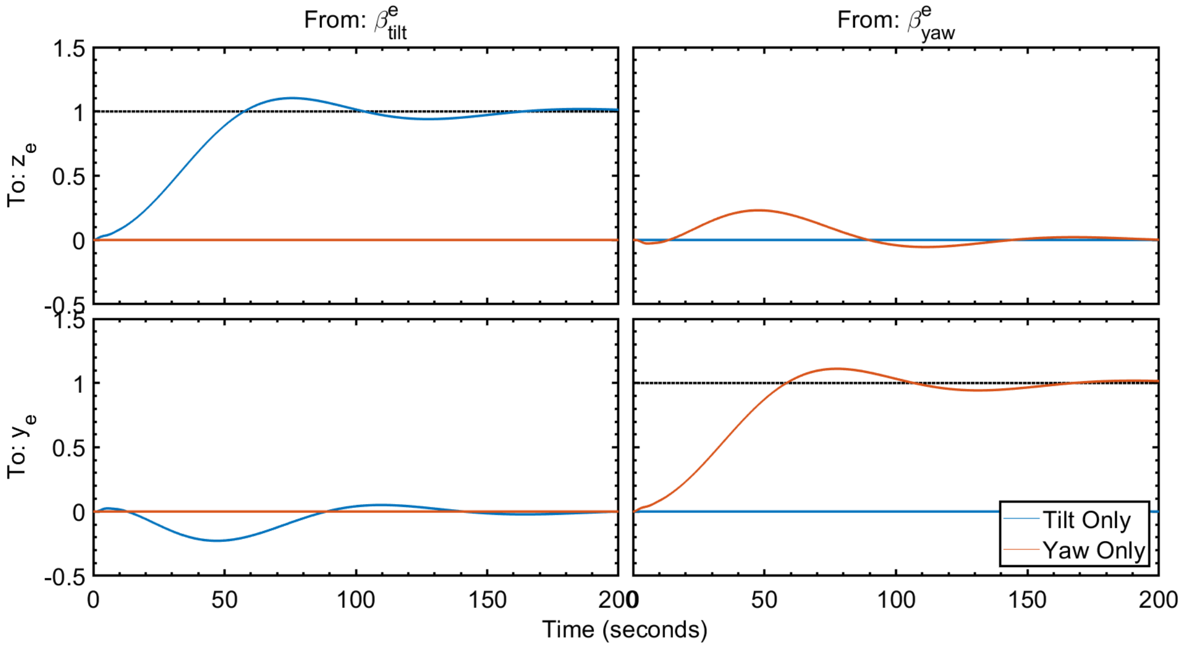

Figure 3-16: Step Response of the MIMO System Controlled with Individual Channels by PI_1 as Eq. 3-13 (blue) and 3-14 (orange) shows.

Thus, based on the above analysis, two potential solutions are proposed to control $G_{ss}(z)$:

- Tune the controller so that the controller primarily functions at the steady-state frequency region where the coupling is the weakest.
- Control the MIMO system by controlling 2 SIMO subsystems individually and in a sequential way.

The first solution requires setting the crossover frequency ω_c of the open-loop transfer function $L(z)$ near the steady-state frequency ω_{ss}. However, the frequency response of $G_{ss}(z)$ in Fig. 3-10 suggests that this solution would result in an excessively slow response speed, making the original open-loop control strategy a clearly superior option. Thus, this solution has not been pursued further.

An alternative solution addresses this problem by utilizing the inherent stability of the plant $G(z)$. Specifically, controlling only the channel $(\beta^e_{\text{tilt}}, 0) \to (z^e, 0)$ through a controller $C_1(z)$ first so that z^e reaches z^e_r while keeping $(0, \beta^e_{\text{yaw}}) \to (0, y^e)$ in open-loop. Once one channel reaches its target, the control can be shifted to the other channel while leaving the previously adjusted channel uncontrolled. Thereby, transferring the control of MIMO system into controlling two SIMO systems sequentially.

The second solution is implemented in this study. The controller PI_1 is selected as $C(z)$ since it outperforms both I_1 and I_1 as Table 3-4 demonstrates. Table 3-5 presents the parameter of the simulated Helix. The Turbulence Intensity (TI) and the shear exponent are defined according to the International Electrotechnical Commission (IEC) 61400-1 design standard [3] [42]. The reference of the Closed-Loop (CL) hub jet is set to the same value as in the Open-Loop (OL) case when the Helix is activated at an amplitude of 3. To simulate the real scenario, the

Helix in the CL case is activated by a ramp signal, with the signal gradually increasing until it reaches the target value over a Helix cycle time T_e of 42 seconds.

Description	Value
Inflow Wind Speed	Uniform, 10 m/s
Helix Rotation Orientation	Counterclockwise (CCW)
Strouhal Number	0.3
Turbulence Intensity	0 %
Shear Exponent	0.0
OL Helix Amplitude	3
CL Hub Jet Reference	$(z_r, y_r) = (8.8, 8.7)$

Table 3-5: Parameter of the Helix and reference.

Fig. 3-17 presents the result of reference tracking in the Helix frame.

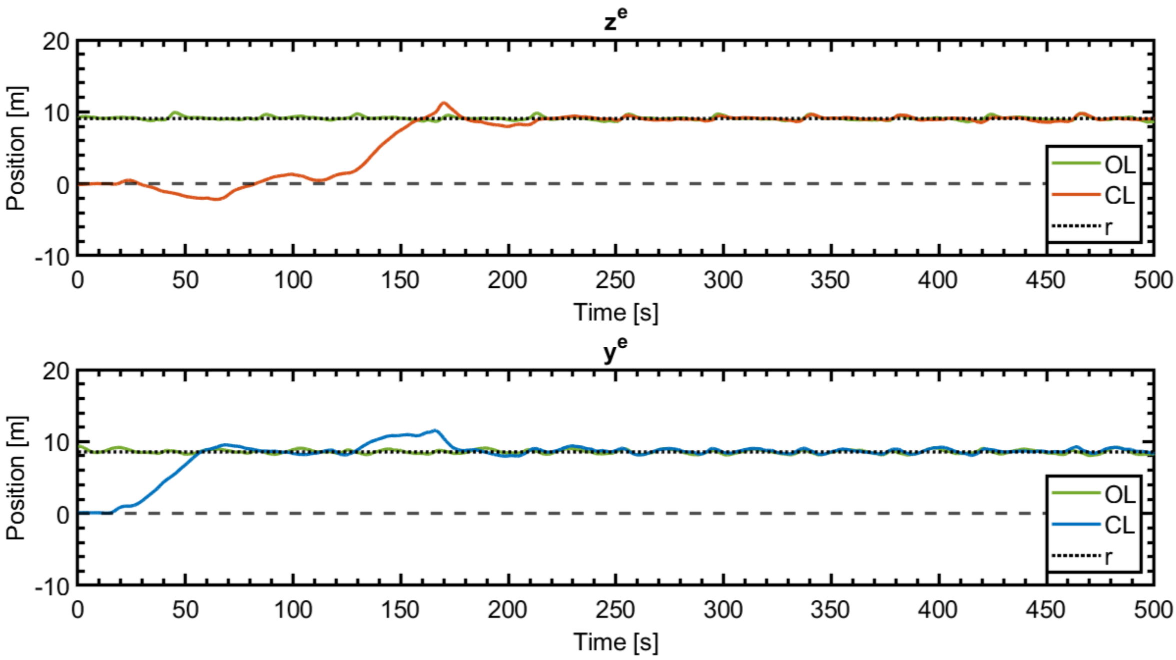

Figure 3-17: The reference tracking performance of the open-loop and closed-loop system.

The corresponding input signals are shown in Fig 3-18. As described, the control of $\beta^e_{\text{tilt}} \rightarrow z^e$ and $\beta^e_{\text{yaw}} \rightarrow y^e$ are activated respectively and sequentially. The switching time is set to $T_{\text{switch}} = 100$ seconds. Prior to this time, only the first channel is activated to rectify the y^e. Once the second channel is activated, the input for the first channel is held at its stabilized value, while the second controller adjusts z^e to reach the reference value. The result in Fig. 3-17 demonstrates that the proposed solution is able to achieve the control goal of the MIMO system.

The above simulation demonstrates that decentralized control of the MIMO system can be achieved using the second proposed solution. However, this solution has three significant limitations:

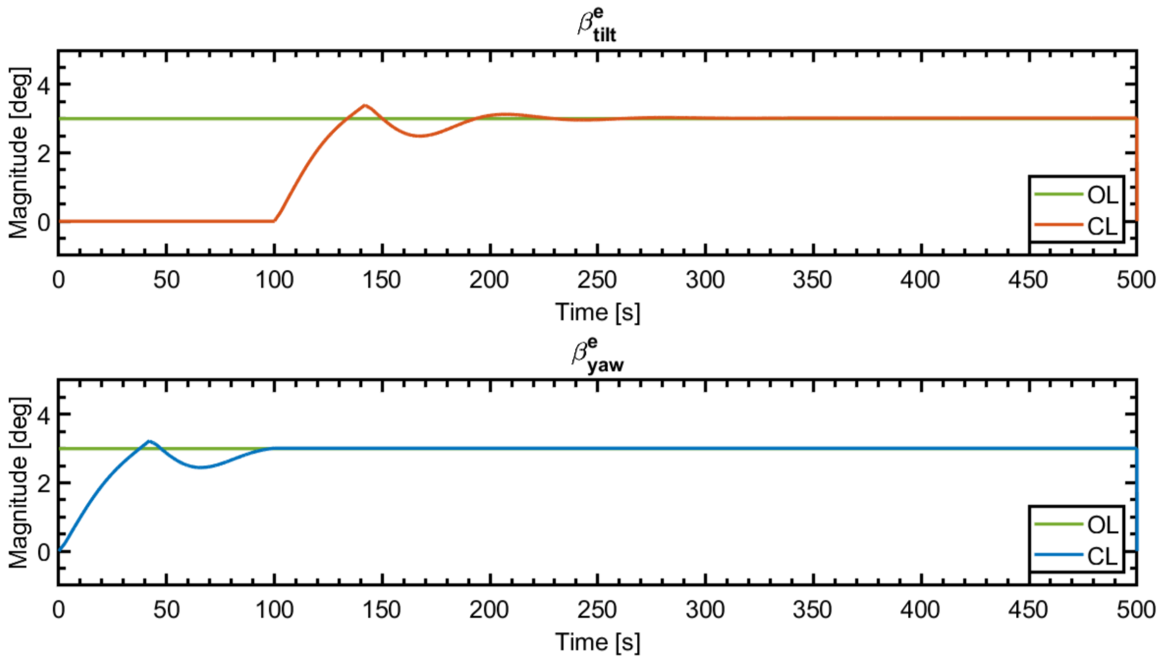

Figure 3-18: Input signals of the reference tracking of the open-loop and closed-loop system.

- It does not allow the adjustment of both channels simultaneously. This brings significant challenges for implementing the controller on a real wind turbine.
- The transition from one individual channel to two channels also brings an additional phase shift to the pitch signal β, this could create additional load because of the inconsistent rotation movement.
- A key to the success of this approach is that the second channel remains unaffected when uncontrolled. However, this condition is not always guaranteed.

These limitations bring more complexity to applying the method in practice. To summarize, the decentralized control approach based on the pre-compensator is explored in this chapter. For simplicity, only $G_{ss}(z)$ is studied. A theoretical analysis suggests that decentralized control is viable. However, the inherent interaction of $G(z)$ hinders the performance of decentralized control. To address this issue, a sequential control approach is proposed and simulated. The result indicates successful control of $G_{ss}(z)$. However, the proposed approach has three primary limitations that restrict its feasibility to real wind turbines. Furthermore, the decoupling itself is highly sensitive to modeling error and uncertainties [57], both of which exist in the identified model. Consequently, a MIMO controller may be required to improve overall performance. This facilitates the work of Chapter 3-4.

3-4 Multiple-Input, Multiple-Output System Control

Based on the analysis of the previous chapter, an $\mathcal{H}_\infty$ controller is designed. At the beginning of this chapter, the basics of MIMO control and its main difference compared to SISO control are introduced. Among all the controller choices, the $\mathcal{H}_\infty$ controller is selected for its ability to handle uncertainty and modeling error. The detailed design details are introduced in Chapter 3-4-2. Finally, the Nominal Stability (NS), the Nominal Performance (NP), and the internal stability of the closed-loop system are examined in Chapter 3-4-3.

3-4-1 Multiple-Input, Multiple-Output System Control

Figure 3-19 illustrates a conventional one DOF feedback control configuration with external disturbance d.

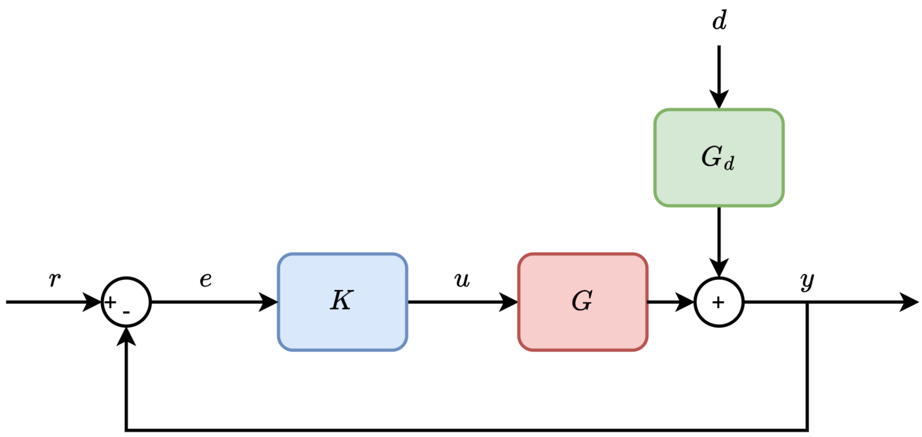

Figure 3-19: Conventional one DOF feedback control configuration with disturbance d.

For preliminary, the open-loop transfer function L, sensitivity S, and complementary sensitivity T are first defined from the output side, respectively as Eq. 3-15 shows:

$$\begin{aligned} L &= GK \\ S &= \frac{1}{1+GK} \\ T &= \frac{GK}{1+GK}. \end{aligned} \tag{3-15}$$

As a result, the output y can be derived as Eq. 3-16:

$$y = \underbrace{\frac{GK}{1+GK}}_{T} \cdot r + \underbrace{\frac{1}{1+GK}}_{S} \cdot G_d \cdot d. \tag{3-16}$$

For a system to track the reference r while rejecting the external disturbance d, T should have a gain of 1 while S should have a small gain ideally at low frequencies. Conversely, at high frequencies, T should have a low gain while S should have a gain of 1. After defining the preliminaries, the main difference between controlling a SISO system and controlling a MIMO system is introduced in the subsequent chapter.

Direction of MIMO Systems A MIMO system is featured by the fact that each input can influence more than one output, leading to interactions between inputs and outputs, which are also referred to as "couplings" in this thesis. This cross-effect between inputs and outputs leads to the presence of directions in controlling a MIMO system [57].

Unlike SISO system, the gain of a MIMO system $G_{\text{MIMO}}(z)$ of a particular input u is given by Eq. 3-17 in which $||\dots||_2$ denotes the vector 2 norm:

$$\frac{||y(e^{j\omega T_s})||_2}{||u(e^{j\omega T_s})||_2} = \frac{||G_{\text{MIMO}}(e^{j\omega T_s})u(e^{j\omega T_s})||_2}{||u(e^{j\omega T_s})||_2}. \tag{3-17}$$

As a result, the gain is represented by a vector instead of a scalar. The gain given by Eq. 3-17 is independent of the input magnitude but depends on the direction of the input u [57]. Correspondingly, the maximum gain as the direction of the input is varied is the maximum singular value of G, shown in Eq. 3-18:

$$\max_{\mathbf{d}\neq 0} \frac{\|Gu\|_2}{\|u\|_2} = \max_{\|u\|_2=1} \|Gu\|_2 = \bar{\sigma}(G) \tag{3-18}$$

whereas the minimum gain is the minimum singular value of G, as shown in Eq. 3-19:

$$\min_{\mathbf{d}\neq 0} \frac{\|Gu\|_2}{\|u\|_2} = \min_{\|u\|_2=1} \|Gu\|_2 = \underline{\sigma}(G). \tag{3-19}$$

The "direction" of gain makes it impossible to simply analogize some concepts between the SISO system and MIMO system. The example from the work [57] shows that eigenvalues can be misleading in judging the performance of a MIMO system since eigenvalues only measure the gain for the special case when the inputs and the outputs are in the same direction of the eigenvectors. Consequently, the maximum and minimum gain offer more comprehensive insights into the performance of a MIMO system. In practice, both the maximum and minimum gain can be acquired through Singular Value Decomposition (SVD) [57]. The SVD is in favor of eigenvalue decomposition for analyzing gains and directionality of a MIMO system since the plant directions obtained from the SVD are orthogonal, and it can be applied to a non-square plant [57]. Therefore, by using the SVD, the largest gain for any input direction is equal to the maximum singular value. Assume the index of the maximum singular value is denoted as max, then this relationship can be expressed as

$$\bar{\sigma}(G) \equiv \sigma_{max}(G) = \max_{d\neq 0} \frac{||Gd||_2}{||d||_2} = \frac{||Gv_{max}||_2}{||v_{max}||_2} \tag{3-20}$$

and vice versa for the lowest gain.

$$\underline{\sigma}(G) \equiv \sigma_{min}(G) = \min_{d\neq 0} \frac{||Gd||_2}{||d||_2} = \frac{||Gv_{min}||_2}{||v_{min}||_2}. \tag{3-21}$$

The singular value not only offers an indication of the direction of the input-output interaction but also the frequency-domain performance and robustness. Take reference tracking for instance, the relationship between the output y and error e can be derived from Eq. 3-16 as

$$e = y - r = \underbrace{\frac{1}{1+GK}}_{S} \cdot y. \tag{3-22}$$

As a result, the gain of $||e(\omega)||_2/||r(\omega)||_2$, which ideally is kept very small, is bounded by

$$\underline{\sigma}\left(S(e^{j\omega T_s})\right) \leq \frac{\|e(\omega)\|_2}{\|r(\omega)\|_2} \leq \bar{\sigma}\left(S(e^{j\omega T_s})\right). \tag{3-23}$$

In terms of performance, it is reasonable to require that the gain $||e(\omega)||_2/||r(\omega)||_2$ remains small for any direction, including the "worse-case" direction which gives a gain of $\bar{\sigma}(S(e^{j\omega T_s}))$. Assume the maximum allowed magnitude of $||e(\omega)||_2/||r(\omega)||_2$ denotes M, then the controller should be designed so that the

$$\bar{\sigma}(S(j\omega)) < M, \forall\omega. \tag{3-24}$$

This property facilitates an alternative way to control the MIMO system compared to decentralized control: Synthesize a MIMO controller $K(z)$ directly based on minimizing some objective functions, or norms [57]. As a result, the general control problem of a MIMO system can be formulated.

General Control Problem Formulation Figure 3-20 demonstrates a general control configuration.

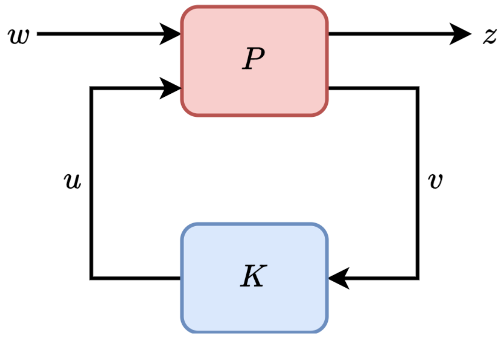

Figure 3-20: General control configuration for the case without model uncertainty. Figure adapted from [57].

Variable u and v denote the inputs of the generalized plant P while w and z denote the outputs. Thus, the controller design problem is to find a controller K which based on the information in v, generates a control signal u which counteracts the influence of w on z, thereby minimizing the closed-loop norm from w to z [57]. The state space representation of the system represented in Fig. 3-20 can be written as Eq. 3-25 shows in which the generalized plant P is partitioned:

$$\begin{aligned} \begin{bmatrix} z \\ v \end{bmatrix} &= \begin{bmatrix} P_{11}(z) & P_{12}(z) \\ P_{21}(z) & P_{22}(z) \end{bmatrix} \begin{bmatrix} w \\ u \end{bmatrix} \\ u &= K(z)v. \end{aligned} \tag{3-25}$$

The generalized plant is an augmented representation of a control system that includes not only the dynamic of the plant but also the external disturbance d, measurement noise n, and reference r. This representation provides a more comprehensive framework by incorporating all elements influencing the system's behavior. A generalized plant P for reference tracking task is shown below.

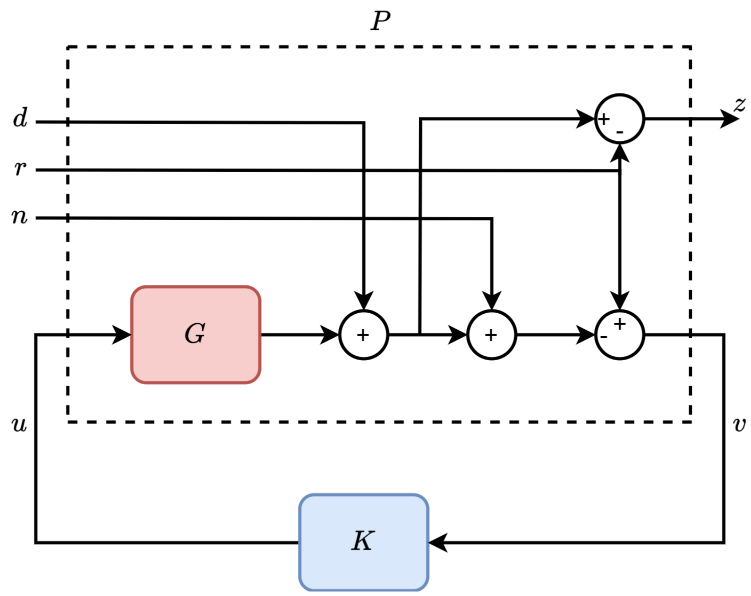

Figure 3-21: The generalized plant P. Figure adapted from [57].

In Fig. 3-21, external disturbance, reference, and measurement noise $[d, r, n]$ are encapsulated as external input w, and the error between the reference signal and the plant's output $z = r - y$ is set as the external output z. Consequently, the state space representation of the system in Fig. 3-21 can be written as Eq. 3-26. This structure is very useful in designing the $\mathcal{H}_\infty$ controller, as the following chapters will show:

$$\begin{bmatrix} d \\ r \\ n \\ u \end{bmatrix} = \begin{bmatrix} I & -I & 0 & G \\ -I & I & -I & -G \end{bmatrix} \begin{bmatrix} z \\ v \end{bmatrix}. \tag{3-26}$$

3-4-2 $\mathcal{H}_\infty$ Controller Design

In this chapter, an $\mathcal{H}_\infty$ controller is designed to achieve the tracking of the hub jet reference in the Helix frame. The $\mathcal{H}_\infty$ controller is selected rather than the Linear Quadratic Gaussian (LQG) controller because the latter requires an accurate model. Even though this requirement is fulfilled in this study, it still limits the application of closed-loop wake mixing control in real engineering scenarios and further hinders the design of a robust controller if uncertainty exists.

The loop shaping focuses on shaping the open-loop transfer function $L(z)$. An apparent problem with this approach is that it does not consider directly the closed-loop transfer function $S(z)$ or $T(z)$, which determines the final response [57]. Therefore, an alternative design strategy is to directly shape the magnitude of the closed-loop transfer function. Such a design strategy can be formulated as an $\mathcal{H}_\infty$ optimal control problem, thus automating the actual controller design and leaving the engineer with the task of selecting reasonable bounds on the desired closed-loop transfer function [57].

$\mathcal{H}_\infty$ Norm The idea of formulating a general control problem is to minimize the $\mathcal{H}_\infty$ norm of the transfer function from input w to output z [57]. For a proper discrete linear stable system $G(z)$, the $\mathcal{H}_\infty$ norm can be acquired by picking out the peak value as a function of frequency using the singular value spatially, generating the definition shown in Eq. 3-27:

$$||G(z)||_\infty \triangleq \max_\omega \bar{\sigma}(G(e^{j\omega T_s})). \tag{3-27}$$

In terms of performance, the $\mathcal{H}_\infty$ norm is the peak of the transfer function magnitude. By introducing weights, the $\mathcal{H}_\infty$ norm can be interpreted as the magnitude of some closed-loop transfer function relative to a specified upper bound [57]. An alternative perspective to understand this term is in the time domain where this term represents the worst-case steady-state gain of a system for sinusoidal inputs at any frequency [57].

$\mathcal{H}_\infty$ Controller Synthesis The $\mathcal{H}_\infty$ controller synthesis uses the general control configuration, as Fig. 3-22 shows.

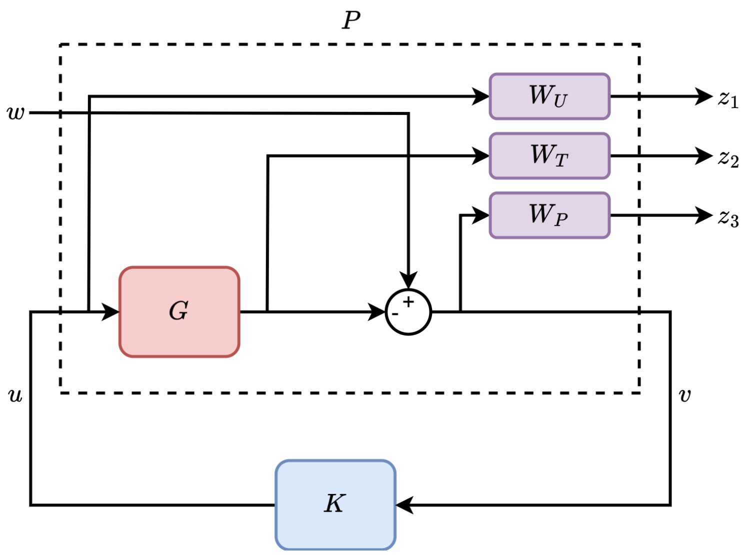

Figure 3-22: Generalized plant P with performance signals z_i and input w.

The idea of formulating a general control problem is to minimize the $\mathcal{H}_\infty$ norm of the transfer function from input w to performance output z [65]. The external input w represents the reference $r = [z_r^e, y_r^e]^T$. Compared to Fig. 3-21, weight functions W_U, W_T, and W_P are now integrated, providing different weighted performance measures as output z_1 to z_3: the sensitivity, the complementary sensitivity, and the controller sensitivity respectively. For the physical interpretation, S gives the transfer function from the disturbance to the system output, T is the transfer function from the reference to the output and is further the complement of S, and $-U$ is the transfer function from the disturbance to the control signal. As a result, the controller K is obtained by minimizing the mixed-sensitivity problem, which is the name given to transfer function shaping problems in which the sensitivity function S is shaped along with one or more other closed-loop transfer functions [57]. Consequently, the optimization problem is represented in Eq. 3-28:

$$\min_K \left\| \begin{matrix} W_P S \\ W_T T \\ W_U U \end{matrix} \right\|_\infty = \min_K \left\| \begin{matrix} W_P(1+GK)^{-1} \\ W_T GK(1+GK)^{-1} \\ W_U K(1+GK)^{-1} \end{matrix} \right\|_\infty . \tag{3-28}$$

In this study, the reference tracking problem is converted to a regulation problem with the error e defined in Eq. 3-22. Thus, for good tracking performance, the closed-loop system should reject a disturbance e. This conversion offers an insight into the ideal pattern of sensitivity functions:

- The disturbance d is typically a low-frequency signal, and therefore it will be successfully rejected if the maximum singular value of S is made small over the same low frequencies. In the high frequency, S should be close to 0 dB. This indicates that the system is less sensitive to high-frequency components, like sensor noise or unmodeled dynamics, which is beneficial for stability.
- The complementary sensitivity function T should be close to 0 dB at low frequencies, indicating an accurate following of the reference. At high frequencies, T should roll off, preventing the system from responding to high-frequency components, which could lead to instability or unnecessary control effort.
- The controller sensitivity function U should have a relatively moderate value at low frequency, reflecting the necessary control effort for tracking the reference signal. A peak of U is expected at the bandwidth frequency, as this is the frequency where the controller is most active. Further, U should decrease nearly to a very small value at the high frequency. This indicates limited control effort at high frequencies, preventing excessive control actions in response to high-frequency noise or disturbances.

As a result, the pattern of ideal mixed sensitivity is summarized in Table 3-6. Note that the magnitudes explained below are not in decibels.

Frequency Range	S	T	U
Low Frequency	Near 0	Close to 1	Moderate
Bandwidth Frequency	Increasing transition	Decreasing transition	Peak
High Frequency	Close to 1	Near 0	Near 0

Table 3-6: Ideal pattern of S, T, and U in all frequency range.

Table 3-6 offers insights into designing the weight functions. However, there are some constraints on S and T when shaping. For example, a system with good disturbance rejection requires $\bar{\sigma}(S)$ small. At the same time, for better noise attenuation or reference tracking, the ideal $\bar{\sigma}(T)$ should be small as well. Nevertheless, these two requirements cannot be fulfilled at the same time. Thus, there are some trade-offs in MIMO feedback design, limited by some theories [57], which are briefly listed below:

- **Sum of** I Ideally, we want S small to obtain the benefits of feedback, and T small to avoid sensitivity to noise. However, because of the sum of I, these requirements are not simultaneously possible at any frequency.

- **The Waterbed Effects** The waterbed effect indicates that sensitivity S cannot be arbitrarily shaped. If we push S down at some frequencies, then it will have to increase at others.
- **Interpolation Constraints** If z is a Right-Hand-Plant (RHP) zero of $L(s)$, then the sensitivity S and complementary sensitivity T at the zero should equal 1 and 0 respectively. These conditions restrict the shaping of S and T as they should equal certain values.
- **Sensitivity Peak** The weighted sensitivity peak of a stable plant $L(s)$ can be given as

$$\begin{aligned} ||W_P S||_\infty &\geq |W_P(z)| \\ ||W_T T||_\infty &\geq |W_T(z)| \end{aligned} \tag{3-29}$$

in which z denotes the RHP zero.

Weight Designs Based on the analysis of the ideal pattern of S, and considering all the restrictions, the weight functions are designed. For a better interpretation, all the weight functions introduced below are in continuous and scalar form. Additionally, the scalar weight functions are scaled to diagonal matrix form when implemented.

Performance Weight First, to fulfill the requirement of sensitivity S as having a small gain at the low frequency, and having a gain close to 1 at the high frequency, $W_P(s)$ is designed as a low pass filter with a form of Eq. 3-30:

$$W_P(s) = \frac{s/M + \omega_{cl}}{s + A\omega_{cl}}. \tag{3-30}$$

The ω_{cl} denotes the desired closed-loop bandwidth, A is the desired disturbance attenuation inside the bandwidth, and M the desired bound on $||S||_\infty$ and $||T||_\infty$ [65]. The upper bound M and lower bound A of S are set to $M = 10$ and $A = 0.625$ respectively. As for the closed-loop bandwidth ω_{cl}, it cannot be placed wherever it wants it to be because of the limitation posed by the unstable zero. The zero of a MIMO system is defined as the value $s = z$ where $G(s)$ loses rank. Therefore, an examination of the transfer function of the MIMO system indicates the existence of an unstable zero that is located outside the unit circle. This can also be noticed in the inverse response of the step response of the original system $G(s)$ shown in Fig. 3-1 or 3-6. This unstable zero limits control by introducing high gain instability and bandwidth limitations. The former will be introduced when designing the $W_U(s)$. The latter is manifested in an upper bound for closed-loop bandwidth ω_{cl} of $z/2$. This bound can be derived from the sensitivity peak, specifically, in the continuous time the relationship shown in Eq. 3-31 is fulfilled in which z denotes the unstable zero

$$||w_p S(s)||_\infty = \max_\omega |w_P(j\omega)| \cdot \bar{\sigma}(S(j\omega)) \geq |w_P(z)|. \tag{3-31}$$

By selecting the weight $w_P(s)$ such that we require tight control at low frequencies and a peak for $\bar{\sigma}(S)$ less than 2, which is the case of this study, it can be derived from Eq. 3-32 that the bandwidth in the worst direction must for a real RHP zero satisfy $\omega_b < z/2$:

$$|w_P(z)| = |\frac{z/M + \omega_B^*}{z + \omega_B^* A}| = z \cdot \frac{1 - 1/M}{1 - A} < 1. \tag{3-32}$$

In this study, the discrete zero is located at 1.0074, which is 0.0737 in the continuous time. Thus, imposing an upper bound for ω_{cl} at 0.0369 [rad/s]. Therefore, the desired closed-loop bandwidth is set to $\omega_{cl} = 0.02$ [rad/s] conversatively.

Controller Weight The presence of a non-minimum phase zero indirectly limits the controller gains for stability requirement [57]. This is because the non-minimum phase zero introduces extra phase lag to the system, which reduces the phase margin and makes the system more prone to instability at high gains. As a result, the weight function $W_U(s)$ is designed as a high-pass filter to attenuate the control input in the high frequency [57]. Equation 3-33 shows the definition of weight $W_U(s)$, whose form is inspired by the work of [65]:

$$W_U(s) = 0.4B^2 \cdot \frac{s^2 + \sqrt{2}\omega_c + \omega_c^2}{s^2 + B\sqrt{2}\omega_c s + (B\omega_c)^2}. \tag{3-33}$$

From the definition, the $W_U(s)$ has the structure of a band-limited high-pass filter. Parameter B scales the frequency at which control effort starts to be limited, and ω_c is related to the cutoff frequency. In this study, B is selected as 10, and the crossover frequency ω_c is set to 0.15 [rad/s] according to the pitch controller changing rate.

Complementary Sensitivity Weight Finally, $W_T(z)$ is kept at 0 since the complementary relationship between S and T [57]. Additionally, the shaping of closed-loop transfer functions by optimizing the stacked cost functions becomes difficult with more than two functions [57].

Figure 3-23 illustrates the bode plot of the designed controller K. The frequency response of the controller K indicates the expected ideal response. At the low frequencies, K functions mildly, this is ideal because the high controller gain might introduce instability as analyzed when designing $W_U(s)$. This mild magnitude of functioning remains until near the bandwidth frequency ω_b, characterized by the peak, and then K rolls off in the high-frequency region.

In this chapter, an $\mathcal{H}_\infty$ controller is designed for reference tracking. This chapter first introduces the main idea of $\mathcal{H}_\infty$ controller design, which is shaping the closed-loop transfer function of the MIMO system. Then, the limitations on the shaping are introduced. Based on those limitations and the ideal form, the weight functions $W_P(s)$ and $W_U(s)$ are designed. In the next chapter, the stability of the controller is analyzed.

3-4-3 Stability Analysis

In this chapter, the NS and the NP of the closed-loop system controlled by the designed $\mathcal{H}_\infty$ controller are analyzed. The NS and NP are defined relative to Robust Stability (RS) and Robust Performance (RP) with the difference being that RS and RP focus on the stability and performance of the system when a bounded uncertainty is presented. Since this study does not consider the uncertainty, only the NS and NP are tested.

Nominal Stability

The NS of the closed-loop system is checked by Theorem 4.1 from [57] which establishes the relationship between system poles and stability. An examination of the poles of complementary sensitivity T indicates that all of them lay within the unit circle. Therefore, closed-loop

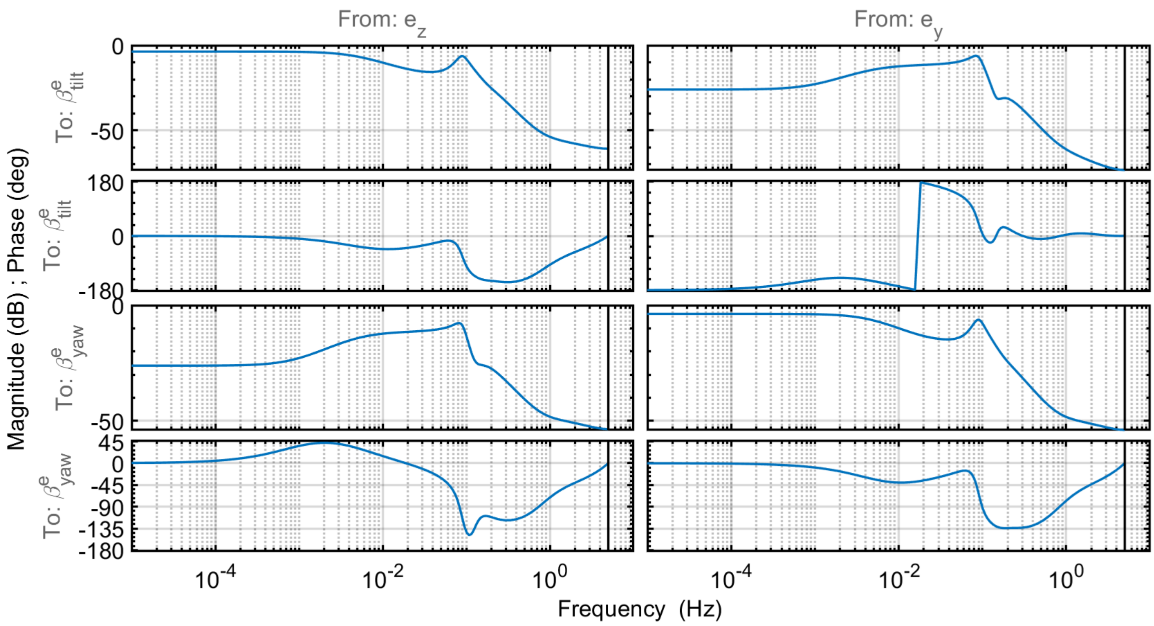

Figure 3-23: Bode plot of the designed $\mathcal{H}_\infty$ controller.

stability is confirmed. This is further validated by the step response, which is shown in Fig. 3-24, where a reference of $r = [z_r, y_r]^T = [1, 1]^T$ is given. Compared to the open-loop system, the closed-loop system follows the reference at a right steady-state value.

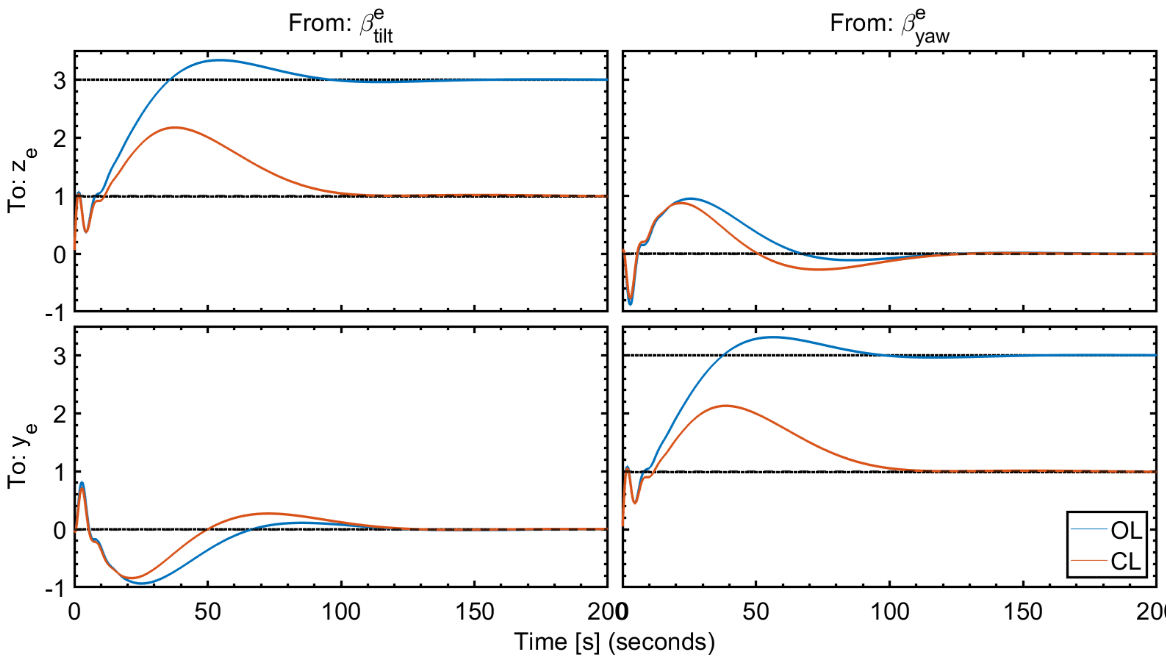

Figure 3-24: Step response of the open-loop (blue) and the closed-loop system (orange).

Internal Stability

Apart from nominal stability, internal stability is checked to avoid problems like actuator saturation, amplified noise, reduced robustness, and so on [57]. Fig. 3-25 shows the normal bode diagram used to check the internal stability, based on which the input u and output y can be written as Eq. 3-34

$$\begin{aligned} u &= (I + KG)^{-1} d_u - K(I + GK)^{-1} d_y \\ y &= G(I + KG)^{-1} d_u + (I + GK)^{-1} d_y. \end{aligned} \tag{3-34}$$

As a result, the internal stability is guaranteed based on theorem 4.4 of [57], stating:

Theorem 3-4.1 (Internal Stability)**.** *Assume that the components G and K contain no unstable hidden modes. Then the feedback system in Fig. 3-25 is internally stable if and only if all four closed-loop transfer matrices in Eq. 3-34 are stable.*

In this work, the poles of G, K, and all the four transfer matrices in Eq. 3-34 are checked, and it has been verified that all of the poles are located in the unit circle. Therefore, the designed closed-loop system is internally stable.

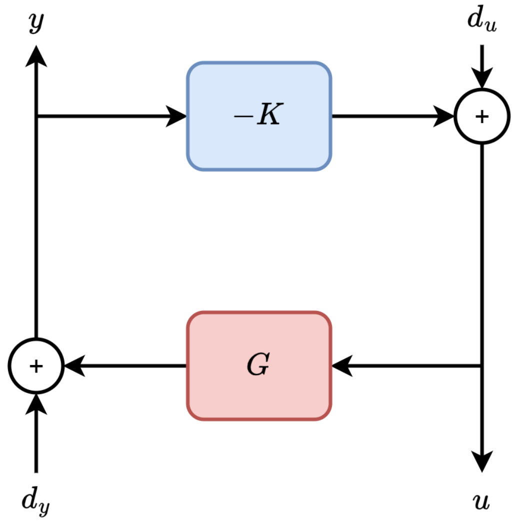

Figure 3-25: Block diagram used to check internal stability of feedback system. Figure adapted from [57].

Nominal Performance

The analysis of the controller performance is crucial as the real object of control is to improve performance, that is, to make the output $y(t)$ behave more desirably [57]. Thus, the performance of the controller is analyzed from the time domain and the frequency domain respectively in this chapter.

Time Domain Performance The time domain performance is evaluated using the step response. As shown in Fig. 3-24, the closed-loop system follows the reference effectively without steady-state error compared to the open-loop system. Nevertheless, the step response exhibits a long settling time and a large overshoot. This behavior can be explained by examining the controller bode diagram as shown in Fig. 3-14, which shows that the controller has a low gain of -3.75 dB at low frequencies, corresponding to a gain magnitude of 0.6494. This low gain value suggests that the controller applies a moderate input u when rectifying the closed-loop system. This gain is deliberately kept very small to account for the existence of the non-minimum phase zero, which could otherwise bring high gain instability.

Frequency Domain Performance The controller performance is checked in the frequency domain by examining the bode plots of S, T, and U as Fig. 3-26 shows.

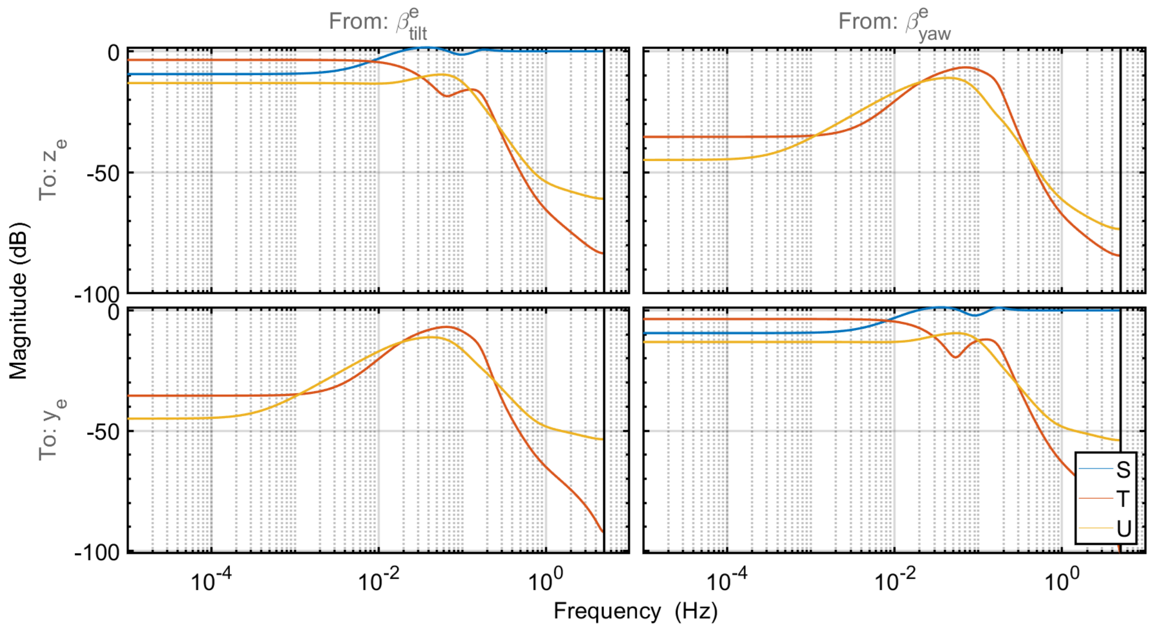

Figure 3-26: Bode diagram of sensitivity, complementary sensitivity, and controller sensitivity.

The acquired transfer functions are first compared with the ideal pattern listed in Table 3-6:

- For the sensitivity S, an ideal pattern is characterized by a low value at low frequencies and a value close to 1 (0 dB) at high frequencies. This pattern is observed in the acquired S, indicating a good disturbance rejection performance.
- Furthermore, for a good reference tracking performance, the complementary sensitivity T should exhibit a value close to 1 (0 dB) at low frequency, and a low value at high frequency. This is also reflected in the acquired T.
- Finally, due to the non-minimum phase zero, the controller should maintain a moderate gain to guarantee stability while remaining active at the bandwidth frequency. Additionally, the controller is expected to roll off beyond the bandwidth frequency so that noises are not amplified. This pattern can also be observed from the acquired U.

Therefore, the sensitivity, complementary sensitivity, and controller sensitivity all achieve the desired pattern.

The controller performance is further examined by using the maximum peak criteria. Equation 3-35 shows the definition of the maximum peaks of the sensitivity and complementary sensitivity function:

$$\begin{aligned} M_S &= \max_{\omega} |S(j\omega)| \\ M_T &= \max_{\omega} |T(j\omega)|. \end{aligned} \tag{3-35}$$

Typically, it is required that the M_S is less than 2 (6 dB) and M_T is less than about 1.25 (2 dB). Otherwise, a large value of M_S or M_T (larger than about 4) indicates poor performance as well as poor robustness [57]. Figure 3-27 illustrates the maximum peak of S and T across frequencies compared to the bound of 6 dB and 2 dB. The result reveals that the peaks remain under the upper bound, further indicating the good performance of the designed controller.

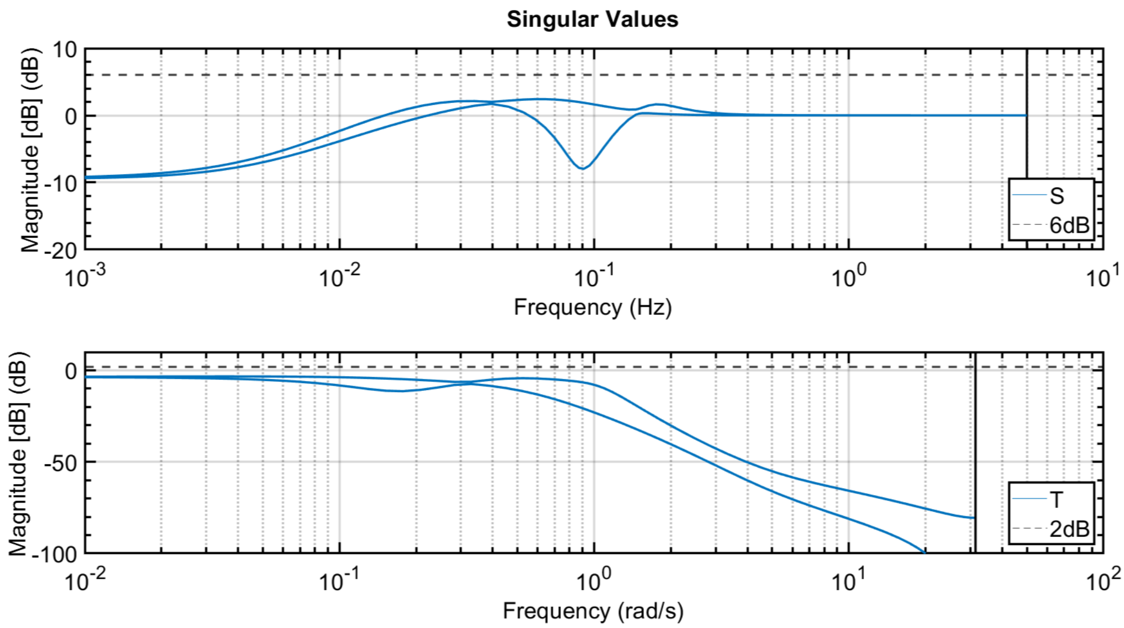

Figure 3-27: Max peaks of S (top) and T (bottom) and their upper bounds.

Lastly, the peaks of the weighted sensitivities are examined. When designing an $\mathcal{H}_\infty$ controller through the optimization of mixed sensitivities, the maximum peak magnitude of mixed sensitivity functions is set to prevent amplification of noise at high frequencies and also introduces a margin of robustness [57]. The equivalence follows from the definition of the $\mathcal{H}_\infty$ norm, which requires that the norm of the weighted sensitivity functions remain less than 1, as expressed in Eq. 3-36:

$$\begin{aligned} ||W_P(s)S||_\infty < 1, \forall\omega \\ ||W_U(s)U||_\infty < 1, \forall\omega. \end{aligned} \tag{3-36}$$

An equivalence of Eq. 3-36 is to check whether the magnitude of the bode plot of sensitivity and complementary sensitivity is bounded by the reciprocal of the weight functions, as below equation shows

$$|S(j\omega)| < \frac{1}{|W_P(j\omega)|}, \forall\omega$$
$$|U(j\omega)| < \frac{1}{|W_U(j\omega)|}, \forall\omega. \tag{3-37}$$

Figure 3-28 illustrates the verification result.

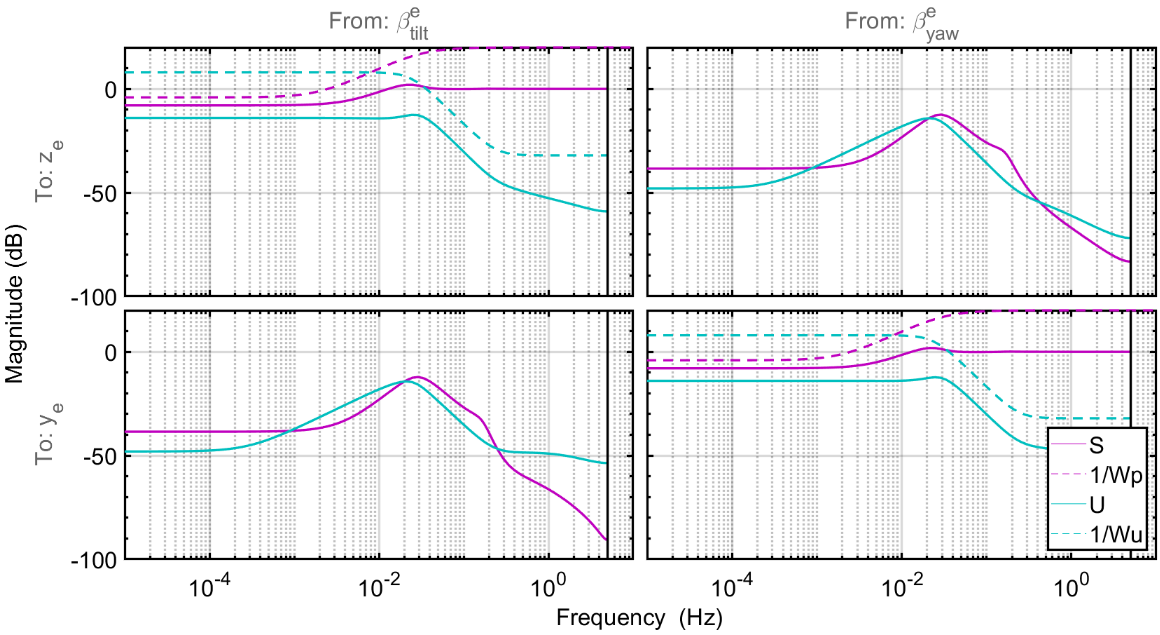

Figure 3-28: Performance evaluation of the controller design, the desired performance boundaries are shown in the dashed line.

As shown in the figure, Eq. 3-36 is satisfied. Therefore, based on the above analysis, it can be concluded that the NP requirements of the closed-loop system are achieved.

3-5 Overall Synthesis

Finally, the designed $\mathcal{H}_\infty$ controller is implemented within the system incorporating the LiDAR subsystem. The Helix with parameters shown in Table 3-5 is simulated.

The corresponding control input generated by the controller is shown in Fig. 3-30.

The tracking result in Fig. 3-29 indicates a successful tracking of $[z^e_r, y^e_r]^T$. Compared to the sequential tracking result of Fig. 3-17, the system can rectify the 2 channels simultaneously. Despite achieving zero steady-state error tracking, the system exhibited increased oscillations during the transient response compared to Fig. 3-24. This discrepancy can be attributed to the fact that Fig. 3-24 considers merely the identified model G while Fig. 3-29 is implemented according to the block diagram shown in Fig. 3-2. In this configuration, the error signal is given by

$$e = \underbrace{(r - y)}_{e_p} + \underbrace{(y_m - \hat{y})}_{e_f} \tag{3-38}$$

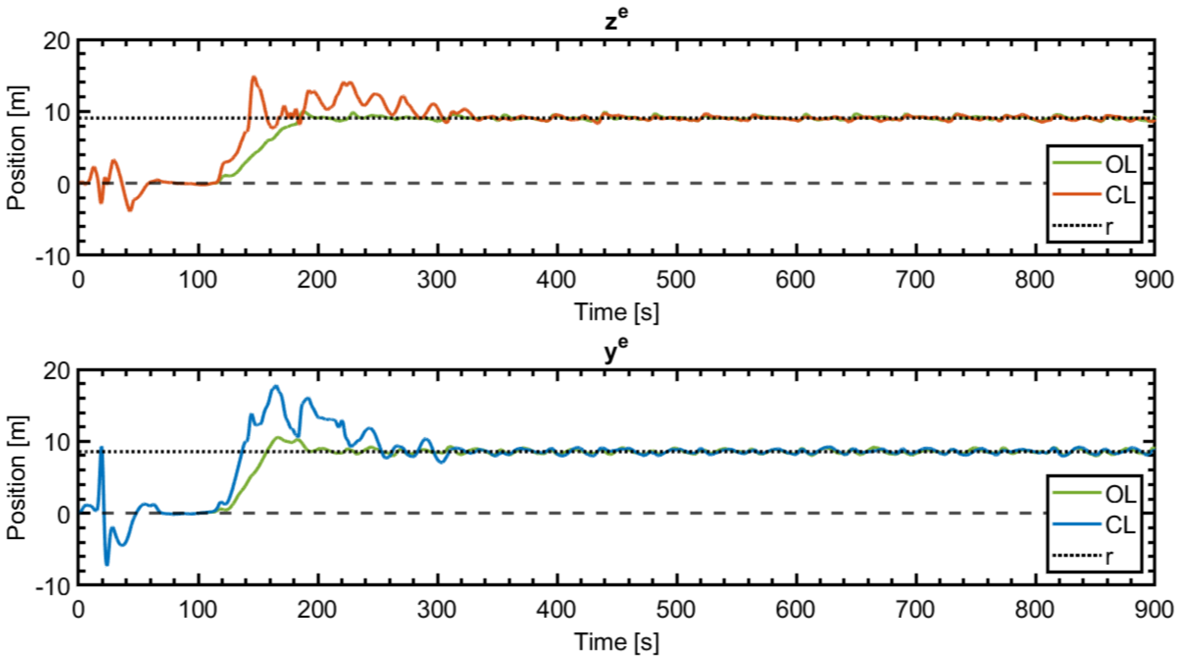

Figure 3-29: Reference tracking comparison between the OL and the $\mathcal{H}_\infty$ controlled system.

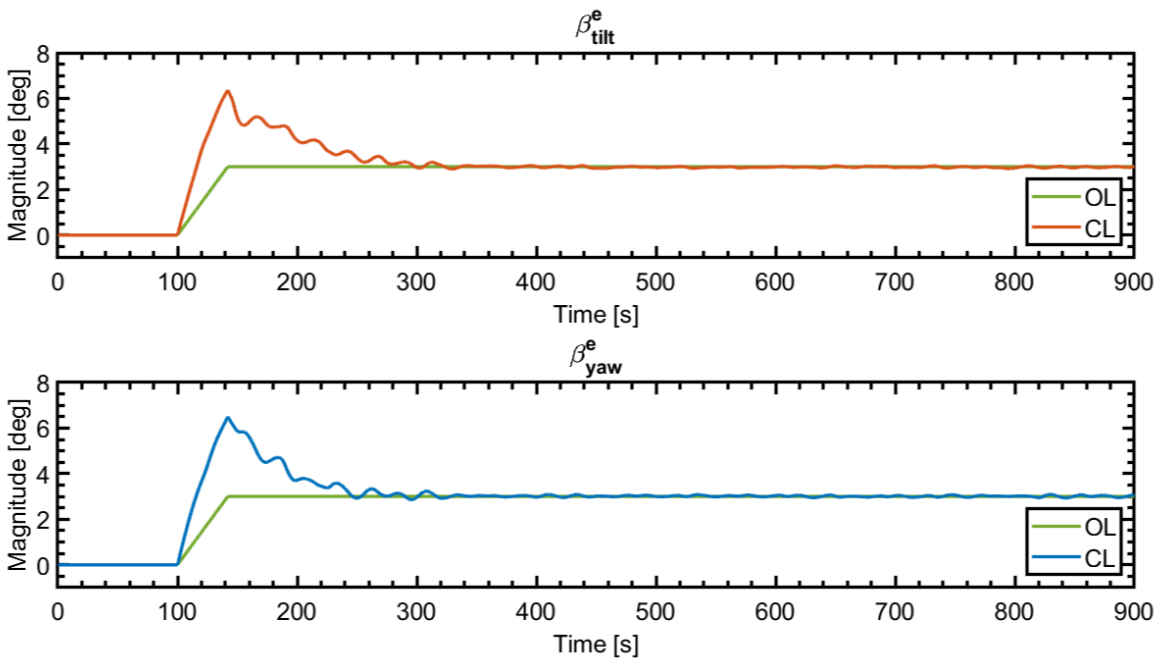

Figure 3-30: Control input comparison between the OL and the $\mathcal{H}_\infty$ controlled system.

where e_p is the difference between the perfect model output and the given reference, and e_f denotes the error between the actual measured output of the wind turbine (y_m) and the predicted output ($\hat{y}$). Subsequently, the inclusion of error e_f in the control loop introduces additional oscillations due to unmodeled dynamics or model mismatch. Consequently, the tracking performance of the controlled system deteriorates.

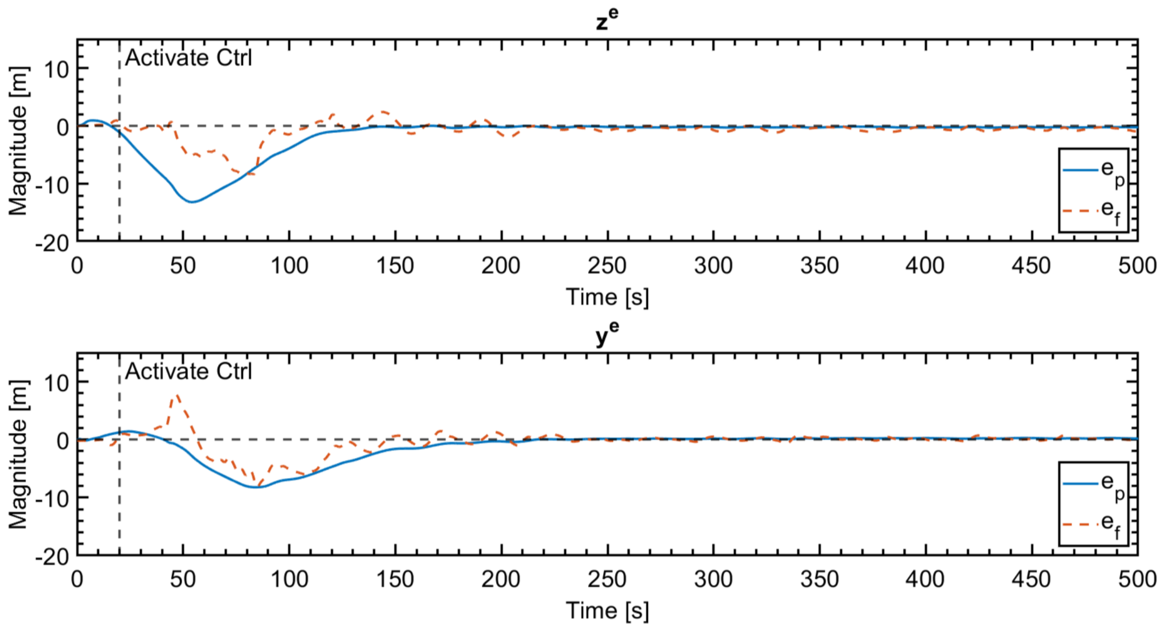

Figure 3-31: Comparison between e_p and e_f when closed-loop control is activated.

Figure 3-31 further validates this explanation, which clearly illustrates the additional oscillations introduced by the error signal e_f. Fortunately, the stability and robustness margins incorporated when designing the $\mathcal{H}_\infty$ controller ensure that the closed-loop system can tolerate this additional error.

To enhance the tracking performance, two potential solutions are proposed:

1. **Incorporating an adaptive filter** One solution is to add an adaptive filter that filters out the unobservable Helix actions, as demonstrated in the work of [33].

2. **Improving model accuracy** An alternative way to solve this problem is to use a more advanced system identification algorithm to develop a more accurate model, thereby eliminating the unmodeled dynamics.

These solutions provide valuable insights into potential directions for future work.

In this chapter, controllers were designed to achieve the goal of tracking the reference hub jet position at the Helix frame. To address the dead-time delay τ, a Smith predictor based on the IMC approach was employed. Subsequently, a fourth-order model was identified using the PBSID-opt method. For control design, a decentralized control strategy was initially attempted. This strategy was not successful because of the system's interaction at the bandwidth frequency and internal pole-zero cancellations. To address this, a sequential control strategy was designed and implemented, which proved to be successful. Nevertheless, a significant drawback of this approach is that it leaves one channel in open-loop operation while the other is being controlled. If a bias is introduced to the open-loop channel, it complicates the control of the remaining channel, making this method less practical for real-world engineering applications. Consequently, an $\mathcal{H}_\infty$ controller was designed to control the MIMO system directly. The weight functions were designed so that the closed-loop transfer functions achieve the desired performance characteristics. Analysis of the closed-loop system confirms that the designed controller satisfies both NS and NP requirements. In the next chapter, the performance of the closed-loop controlled system will be evaluated by testing various scenarios and comparing its performance to the open-loop system.

Chapter 4

Experiment Validation

The initial motivation for designing a closed-loop control framework is to enable dynamic adjustment of the Helix under external uncertainty, ultimately improving the performance of the downstream wind turbine and the wind farm. Different cases are run in QBlade to evaluate the effectiveness of the framework, and the performances of the closed-loop system are compared to those of the open-loop system.

4-1 Simulation Setup

This research uses Qblade [40] as the simulation platform, and the National Renewable Energy Laboratory (NREL)-5MW wind turbine [15] as the object of study. The introduction of these two has already been covered in Chapter 2-2. Several simulation cases were designed to study the proposed control scheme thoroughly. The wind conditions of these cases are summarized in Table 4-1. The Turbulence Intensity (TI) and the shear exponent are defined according to the International Electrotechnical Commission (IEC) 61400-1 design standard [3].

Case	Wind Condition	Control Strategy	WT_1	WT_2
BL	Uniform	-	Greedy	Greedy
OL1	Uniform	Open-Loop (OL)	Counterclockwise (CCW) Helix	Greedy
CL1	Uniform	Closed-Loop (CL)	CCW Helix	Greedy
OL2	Shear 0.2	OL	CCW Helix	Greedy
CL2	Shear 0.2	CL	CCW Helix	Greedy
OL3	TI 6%	OL	CCW Helix	Greedy
CL3	TI 6%	CL	CCW Helix	Greedy
OL4	Shear + TI 6%	OL	CCW Helix	Greedy
CL4	Shear + TI 6%	CL	CCW Helix	Greedy

Table 4-1: Overview of all test cases.

Below are some important notes:

- The wind inflow speed is kept constant for all cases as $u_{\text{in}} = 10\,\text{m/s}$.
- All helical wakes generated rotate in the CCW direction.
- A realistic turbine spacing is $4 - 5D$; therefore, the downstream turbine WT_2 is placed $4D$ (504 meters) from WT_1. This distance balances the trade-off between the QBlade simulation quality and computational speed.
- All cases are simulated for 15 minutes. However, the first 300 seconds of data are excluded from the analysis to account for wake propagation effects. Consequently, the effective simulation time for analysis is 10 minutes, reflecting the turbine's steady-state operating conditions.

The cases presented in Table 4-1 begin with simulation under uniform wind conditions. Subsequently, shear and turbulence are added to further evaluate the performance of the closed-loop system. The exponential factor of shear is set to 0.2 and the TI is set to 6% to mimic the usual condition offshore [3]. Finally, a case is simulated when both shear and turbulence exist. The shear and turbulence in this research are added by using the Turbulence Simulator (TurbSim) unit in QBlade, which generates the wind fields using NREL's TurbSim binary [66]. TurbSim is a stochastic, full-field, turbulence-wind simulator that uses a statistical model to numerically simulate a time series of three-component wind-speed vectors at points in a two-dimensional vertical rectangular grid that is fixed in space [66]. Consequently, the basic wind field information generated by TurbSim used in this study is listed below.

Description	Value
Reference Wind Speed	10 m/s
Grid Width, Height	179, 179 meters
Grid Y, Z Points	20, 20
Turbine Class	I
IEC Standard	61400-1Ed3
Wind Type	Normal Turbulence Model (NTM)
Spectral Model	IEC Kaimal Turbulence Model (IECKAI)
Horizontal & Vertical Inflow Angle	0 deg
Roughness Length	0.01
Wind Profile Type	Power Law
Shear Reference Height	90 meters
Jet Height	100 meters
Turbulence Intensity	Customize
Shear Exponent	Customize

Table 4-2: Parameters of wind field generated by TurbSim

4-2 Experiment Result and Analysis

In this chapter, the simulation results are presented and analyzed. Chapter 4-2-1 first introduces the metrics used for assessment. Subsequently, the performances of the wind turbines while the helical wake is generated in an open-loop manner are examined under shear, turbulence, and combined shear and turbulence, and these cases are compared against the uniform wind scenario. This comparison reveals multiple differences in wind turbines' performance across varying wind conditions relative to the uniform wind case. This observation facilitates the assumption that the objective is to ensure that the wind farm's performance closely resembles that under uniform wind conditions. Therefore, addressing these differences is the goal of the designed controller. Consequently, the performances of the open-loop and closed-loop systems are compared under uniform wind, shear, turbulence, and combined shear and turbulence in Chapters 4-2-3, 4-2-4, 4-2-5, and 4-2-6.

4-2-1 Metric Definition

To decrease the Levelized Cost of Energy (LCoE), it is essential to increase the power production while decreasing the fatigue of the wind turbine. To quantify this, the aerodynamic power, Damage Equivalent Load (DEL), and Pitch Bearing Damage (PBD) are defined to evaluate wind farm performance. Furthermore, since this study focuses on controlling the helical wake, the turbulence intensity and the average inflow speed are used to quantify the flow field quality. The following contents focus on introducing DEL and PBD.

Damage Equivalent Load The DEL quantifies the fatigue in the wind turbine structure, representing the damage that builds up in structures over time due to cyclic loading [31]. This fatigue can be modeled using the Wöhler curve, indicating the number of cycles a structure can endure until failure for the given stress through which it is cycled [3]. The curve's slope is used in DEL calculation, encapsulating the total fatigue damage in one single load. This is equivalent to the total damage of different load cycles experienced by that structure over time [31]. Consequently, the DEL computation requires the ranges and frequencies of various load cycles, which are determined through rain-flow counting. As a result, the DEL is calculated as Eq. 4-1:

$$\text{DEL} = \left(\frac{\sum_{i=1}^{N} (A_i)^m n_i}{n_{eq}} \right)^{\frac{1}{m}}. \tag{4-1}$$

The N is the total count of cycles, m is the inverse Wöhler slope, conventionally taken as 5 for steel tower components and 10 for composite blade structure [47]. Moreover, n_i indicates the number of cycles represented by a range of A_i, and n_{eq} denotes the equivalent cycle, which is set to 1 in this study.

The pitch action of the Helix approach is expected to introduce additional vibrations in the turbine. As a result, these vibrations, which increase with higher Helix amplitude, contribute to the DEL. Moreover, since the DEL calculation sums all cycles, it is also expected that a higher Strouhal number leads to a higher DEL. In this study, the DEL are calculated for the blade using the edge-wise and flap-wise bending moment only because of the availability of data.

Pitch Bearing Damage The Helix approach uses Individual Pitch Control (IPC) command, therefore, the damage to the pitch bearing should also be considered. The definition of PBD is shown in the equation below

$$\text{PBD}(\phi) = \sum_{k=1}^{N} \delta\beta(k) \cdot \left[\max((\cos\phi \cdot M_{\text{flap}}(k) + \sin\phi \cdot M_{\text{edge}}(k)), 0)\right]^m . \tag{4-2}$$

The ϕ is the radial position of the bearing, $\delta\beta$ is the pitch difference, M_{flap} and M_{edge} denote the flap-wise and edge-wise blade bending moment, and m is the inverse Wöhler slope, taken as 3. This study focuses only on the radial position with the largest damage.

Based on Eq. 4-2, PBD is expected to increase with a higher-frequency pitch action due to greater pitch travel. Moreover, a larger Helix amplitude is expected to generate a larger pitch action, which yields larger M_{flap} and M_{edge}, eventually resulting in large PBD.

4-2-2 Helix in Different Wind Conditions

Before evaluating the performance of the closed-loop system, case OL_1, OL_2, OL_3, and OL_4 are first compared to assess the open-loop Helix's behavior when shear, turbulence, and combined shear and turbulence are presented. This comparison is crucial as it offers insights into the objectives of the closed-loop control.

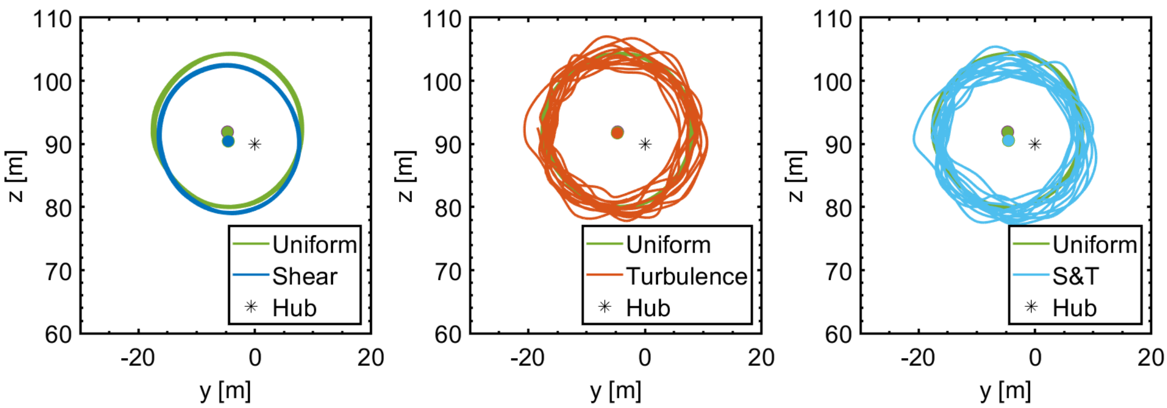

Figure 4-1: Comparison of hub jet trajectory of OL_1 to OL_2, OL_3, and OL_4. "Hub" denotes the hub of the wind turbine.

Figure 4-1 first illustrates the hub jet trajectory in the fixed frame of different wind conditions. The figure reveals a bias in z due to the shear. When turbulence is added, the hub jet trajectory has more oscillation. Finally, when shear and turbulence coexist, the bias in z and oscillation in hub jet trajectory exist simultaneously. The corresponding result in the Helix frame is further shown in Fig. 4-2. Compared to the uniform wind case, both z^e and y^e of OL_2 exhibit periodic components. This can be explained by the Helix frame transform. In OL_3 where turbulence is introduced, the hub jet exhibits more oscillations. However, since the pure turbulence does not change the center of the hub jet, there is no further periodical component. Finally, OL_4 reflects a combination of OL_2 and OL_3.

Consequently, the changes brought by the shear and turbulence influence the power production and the fatigue of the two-turbine setup. Figure 4-3 demonstrates the produced power, flap-wise DEL, and edge-wise DEL. In the figure, the bars in the dashed line represent the

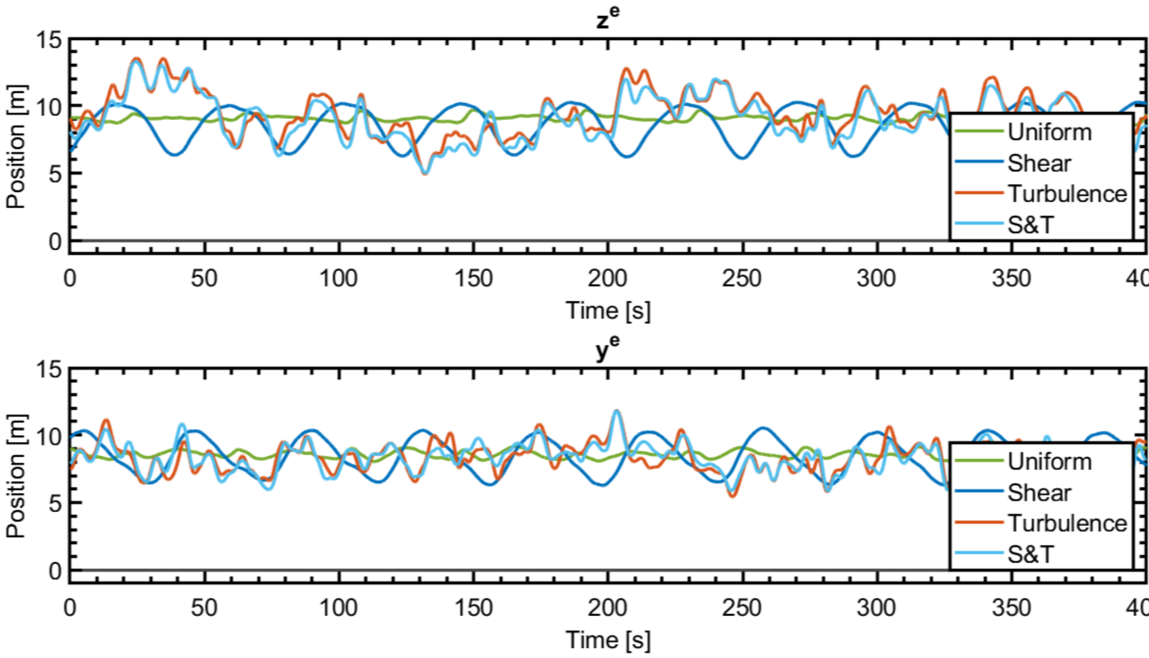

Figure 4-2: The output in the Helix frame for OL_1 (green), OL_2 (Blue), OL_3 (Orange), and OL_4 (sky blue).

wind turbine performance in case OL_1, while the blue, orange, and sky blue denote the one for cases OL_2, OL_3, and OL_4.

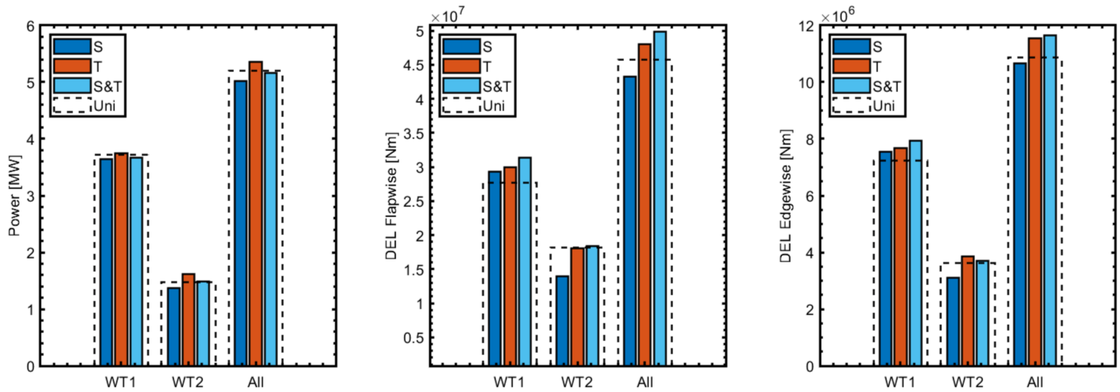

Figure 4-3: The power and DEL of OL_2 (blue), OL_3 (orange), and OL_4 (sky blue) compared to case OL_1 (dashed line). The "Uni", "S", "T", and "S&T" denote "Uniform", "Shear", "Turbulence", and "Shear&Turbulence" respectively.

Table 4-3 summarizes the result in Fig. 4-3 in a more straightforward way by quantifying the delta of change in percentage using OL_1 as a reference. The results in the figure and table reveal that:

- **Shear** When only shear is presented, the power loss of both turbines is evident. However, the cumulative blade edge-wise and flap-wise DEL also decreased. This aligns with the work of [67] which concludes that a higher shear resulted in a reduction in wake recovery and a lower TI in the wake as a whole, indicating the wake deficit reaches farther downstream resulting in a larger power loss of waked turbines downstream [67]. Finally, the PBD of the upstream wind turbine also decreases.

- **Turbulence** Compared to the Helix in the uniform wind case, case OL_2 presents increments in power production and fatigue for both turbines. This can be explained by the increased TI and the natural mixing effects of turbulence [41].
- **Both** Finally, when both shear and turbulence are presented simultaneously, the two-turbine setup had a cumulative loss in power production and cumulative increments in both flap-wise and edge-wise DEL.

	WT_1	WT_2	WT_{1+2}
Power	-2.12% $+0.54\%$ -1.65%	-6.80% $+9.64\%$ 1.19%	-3.45% $+3.12\%$ -0.84%
DEL_f	$+6.00\%$ $+8.43\%$ $+13.66\%$	-23.23% -0.60% $+1.35\%$	-5.59% $+4.85\%$ $+8.78\%$
DEL_e	$+4.27\%$ $+5.85\%$ $+9.53\%$	-13.97% $+6.76\%$ $+2.47\%$	-1.81% $+6.15\%$ 7.17%
PBD	-0.02% $+0.01\%$ -0.01%	-	-

Table 4-3: Summary of change of power, DEL, and PBD of case OL_2 (blue), OL_3 (orange), and OL_4 (sky blue) in percentage compared to OL_1.

This comparison offers a good insight into the expected behavior of the closed-loop controller. Before stating that, *it is important to admit the difficulty in defining a definitive reference point as the interests are diverse.* For example, in the presence of shear, power production decreases but so do the loads. This result could be beneficial depending on the priorities of wind turbine operators. Therefore, there is no universally optimal reference.

This study mainly focuses on controlling the Helix by controlling the hub jet rotation. *Therefore, it is assumed that engineers aim to eliminate variations in the helical wake introduced by external wind conditions. In other words, generating a more consistent Helix relative to the uniform wind case* OL_1. Consequently, the output of OL_1 is used as the reference for all the experiment cases. The corresponding expected behavior of the controller can be summarized as follows:

- CL_1 Uniform: The performance of CL_1 should match that of the OL_1 by generating an identical Helix.
- CL_2 Shear: Compared to OL_2, the controller should be able to rectify the bias. In the Helix frame, this should be represented by the attempt to eliminate the periodic components. This rectification is expected to eliminate the wake deficit introduced by the shear [67].
- CL_3 Turbulence: Under the presence of turbulence, the controller is expected to mitigate the oscillation of the hub jet to a more consistent one. However, due to the high-frequency roll-off characteristic of the designed controller, this mitigation effect may be compromised. For the wind farm, this should result in reduced load because of the more consistent oscillation.
- CL_4 Both: Finally, the two-turbine setup performs the poorest in this case, likely due to both the bias and additional oscillation. Thus, the controller should correct the bias as well as mitigate the oscillation.

4-2-3 Uniform Wind Case

The hub jet trajectory of the steady-state is shown in Fig. 4-4. As the figure reveals, Helix generated in OL_1 and CL_1 are almost identical, indicating the alignment performance of the open-loop and closed-loop systems.

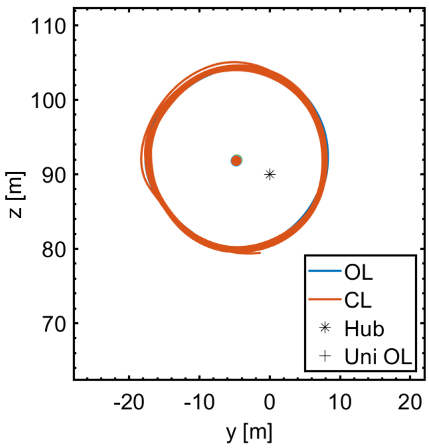

Figure 4-4: The hub jet trajectory comparison between OL_1 and CL_1. "Uni OL" denotes the hub jet center in the uniform case.

The corresponding input and output signal in the Helix frame is illustrated in Fig. 4-5 and Fig. 4-6.

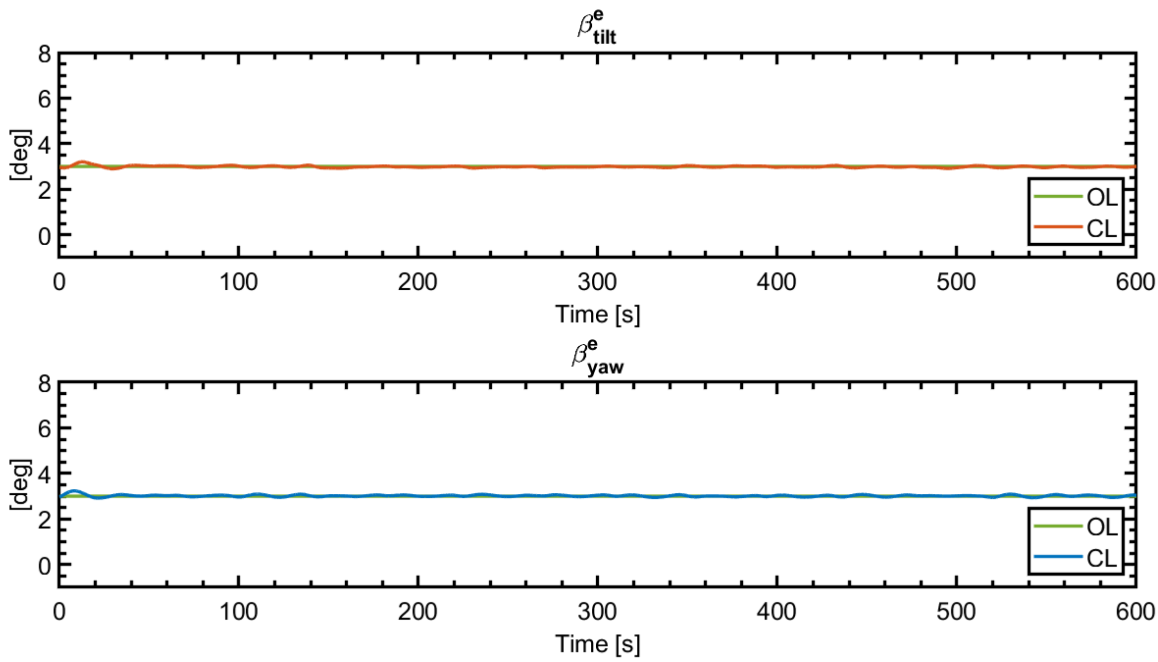

Figure 4-5: The comparison of input signals in the Helix frame between OL_1 and CL_1.

Consequently, the resemblance between OL_1 and CL_1 ends up in similarity of performance at

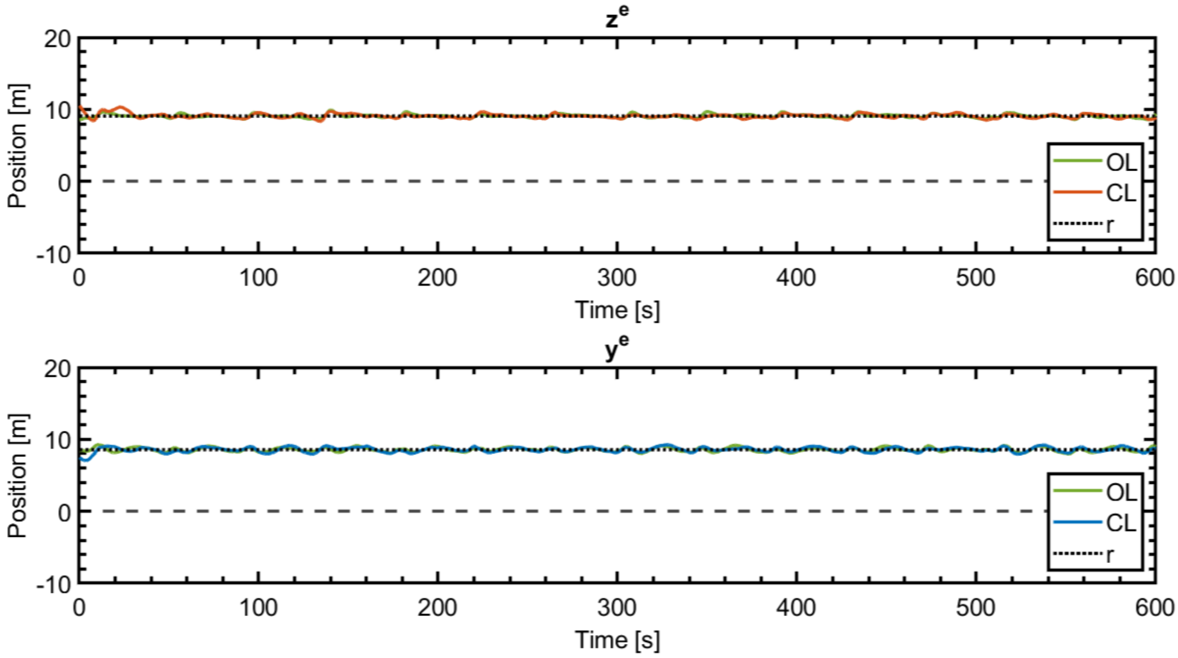

Figure 4-6: The comparison of output signals in the Helix frame between OL_1 and CL_1.

the turbine level. This is further supported by Fig. 4-7 and Table 4-4, in which the delta of change is quantified in percentage using OL_1 as a reference. In this study, the minor change with a magnitude below 0.5% is neglected.

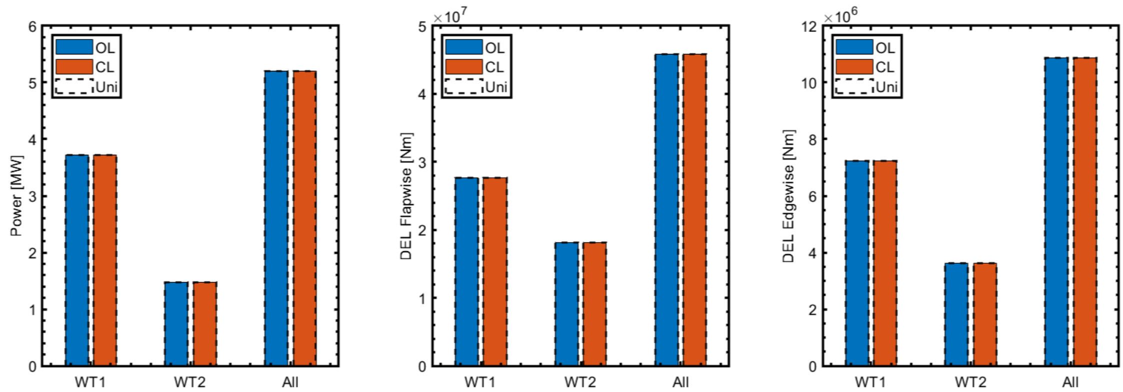

Figure 4-7: The power and DEL of OL_1 and CL_1 case compared to the reference OL_1

	WT_1	WT_2	WT_{1+2}
Power	+0.01%	+0.00%	+0.01%
$\mathrm{DEL_f}$	+0.07%	−0.00%	−0.01%
$\mathrm{DEL_e}$	+0.04%	+0.02%	+0.01%
PBD	+0.01%	-	-
u_{in}	-	+0.01%	-

Table 4-4: Summary of change of power, DEL, and PBD of case CL_1 compared to OL_1.

The results indicate that the performance of the closed-loop system closely aligns with that of the open-loop system as expected. While the DEL for edge-wise and flap-wise directions exhibits some perturbations, the overall sum remains largely consistent.

4-2-4 Pure Shear Case

Figure 4-8 shows the hub jet trajectory of CL_2. The goal of the controller is to eliminate the bias introduced by the shear. This is confirmed by Fig. 4-8. Specifically, compared to OL_2, the center of the hub jet of CL_2 is closer to the position at the uniform case.

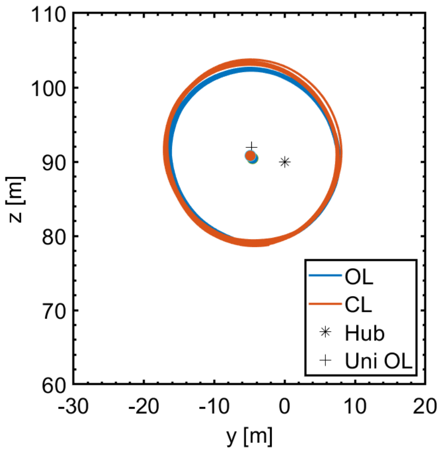

Figure 4-8: The hub jet trajectory comparison between OL_2 and CL_2.

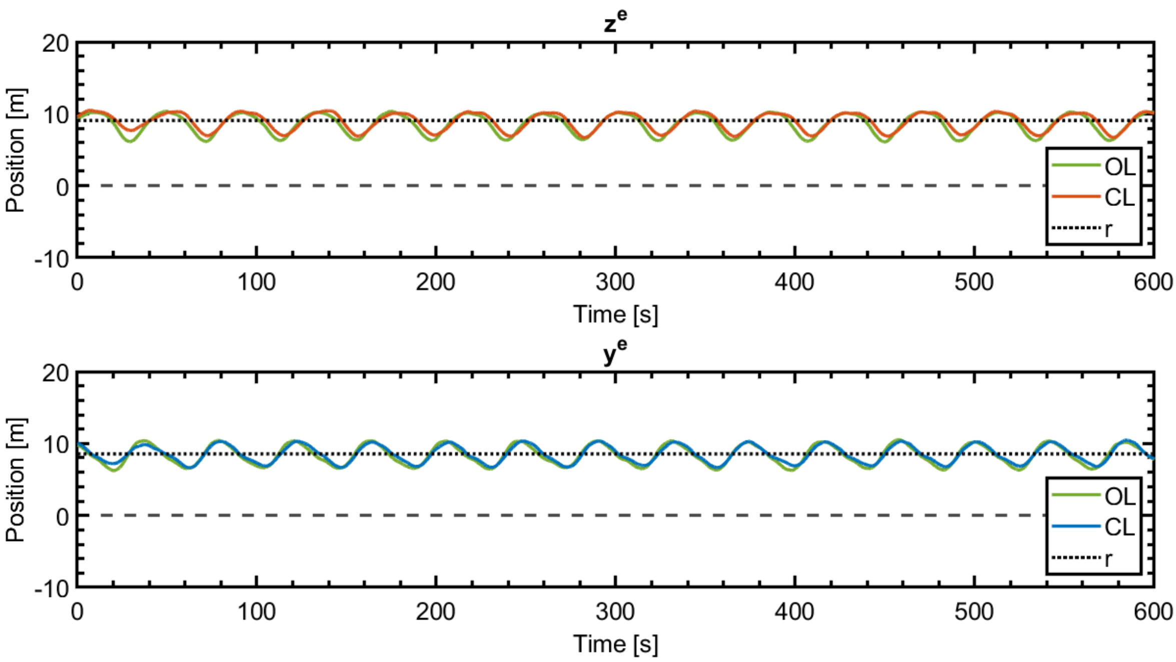

Figure 4-9: The comparison of output signals in the Helix frame between OL_2 and CL_2.

The corresponding output signal in the Helix frame is illustrated in Fig. 4-9. The dashed line r stands for the given reference, based on the above analysis, this is given as the value corresponding to the value of Helix in the uniform wind. The output shows that CL_2 exhibits a slightly reduced periodic component compared to OL_2. This is particularly evident in z^e, where both the peaks and troughs of CL_2 are smaller than those of OL_2. However, since the hub jet center has not fully returned to the reference position, a periodic component remains present.

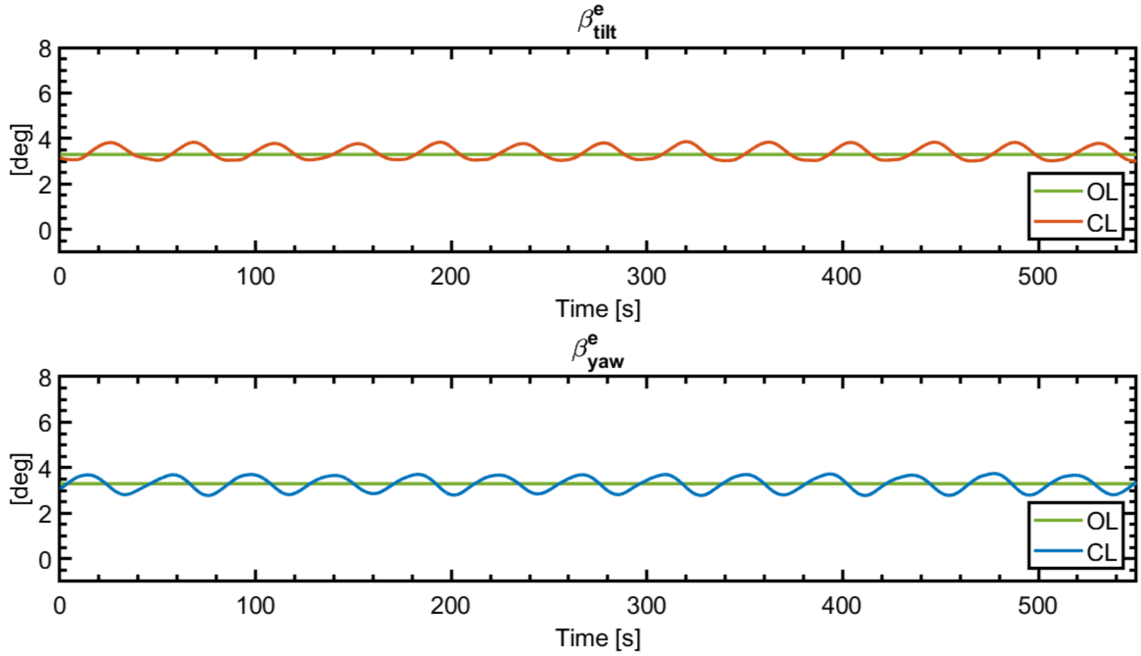

Figure 4-10: The comparison of input signals in the Helix frame between OL_2 and CL_2.

The corresponding input signal is shown in Fig. 4-10. Compared to OL_2, the input signal of CL_2 includes an additional periodic component with the same frequency as the Helix, ω_e. This aligns with the expectation as the controller aims to induce a yaw movement through the IPC command. Specifically, the work of [68] discovered that yaw movement can be achieved through dynamic IPC command. This would require a bias term b adding to the corresponding channel to the blade pitch signal in the fixed frame as Eq. 4-3 shows [68]. As a result, when this input is mapped to the Helix frame, the constant bias b introduces periodic components with a frequency of ω_e to both β^e_{tilt} and β^e_{yaw} as Appdenix A shows:

$$\begin{bmatrix} \beta_1(t) \\ \beta_2(t) \\ \beta_3(t) \end{bmatrix} = \underbrace{\begin{bmatrix} 1 & \cos(\psi_1 + \psi_{\text{off}}) & \sin(\psi_1 + \psi_{\text{off}}) \\ 1 & \cos(\psi_2 + \psi_{\text{off}}) & \sin(\psi_2 + \psi_{\text{off}}) \\ 1 & \cos(\psi_3 + \psi_{\text{off}}) & \sin(\psi_3 + \psi_{\text{off}}) \end{bmatrix}}_{T^{-1}(\omega_r t + \psi_{\text{off}})} \cdot \begin{bmatrix} \beta_{\text{col}}(t) \\ \beta_{\text{tilt}}(t) + b \\ \beta_{\text{yaw}}(t) \end{bmatrix}. \tag{4-3}$$

Consequently, the change of generated power, DEL, and PBD are summarized in Table 4-5. The result shows that the power production of the downstream wind turbine increases with the bias being corrected. This is further supported by the wind measurement at $4D$ position, indicating that the average inflow speed of CL_2 is 6.05 m/s while that of the OL_2 is only

5.95 m/s. However, this increment in power comes at a cost. The blade pitch signal for the upstream wind turbine exhibits a larger magnitude and less consistency, leading to increases in both the DEL and PBD for the upstream turbine.

	WT_1	WT_2	WT_{1+2}
Power	−0.35%	+0.67%	−0.19%
DEL Flap-wise	+1.70%	+1.80%	+6.94%
DEL Edge-wise	+1.80%	+1.14%	+4.61%
PBD	+1.02%	-	-
u_{in}	-	+0.02%	-

Table 4-5: Summary of change of power, DEL, and PBD of case CL_2 compared to OL_2.

To pursue a better rectification, a more aggressive controller is adopted. The generated hub jet trajectory is shown in Fig. 4-11.

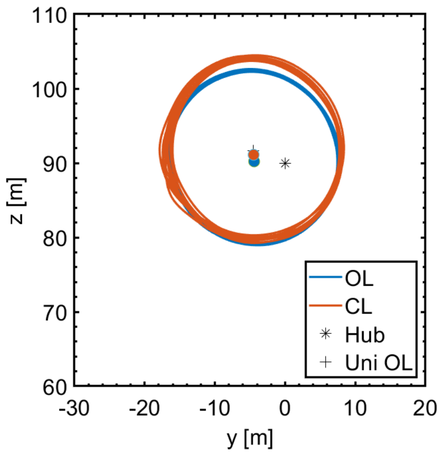

Figure 4-11: The hub jet trajectory comparison between OL_2 and CL_2 with a more aggressive controller.

The corresponding control input is demonstrated in Fig. 4-12.

Compared to Fig. 4-10, the control input generated is notably stronger in terms of oscillation while the average magnitude is kept at 3.0. The pattern of input aligned with the expectation as Eq. 4-3 shows. Consequently, this control action indeed moves the Helix more towards the uniform case as Fig. 4-11 demonstrates. The corresponding performances are summarized in Fig. 4-13 and quantified in Table 4-6.

Figure 4-13 illustrates that the performance of the downstream turbine is more consistent with that of OL_1 as well as the power production for the two turbines setup due to the correction of the bias. This is further supported by the table, demonstrating that the power production of the downstream turbine increased by 4.96%. As previously analyzed, the rectification requires more dynamic control actions from the upstream turbine, resulting in higher loads and reduced power production. Nevertheless, the overall power production of the two-turbine setup increases. However, this gain in power comes at the cost of increased fatigue loads for both the upstream and downstream turbines. The increase in fatigue can be attributed to

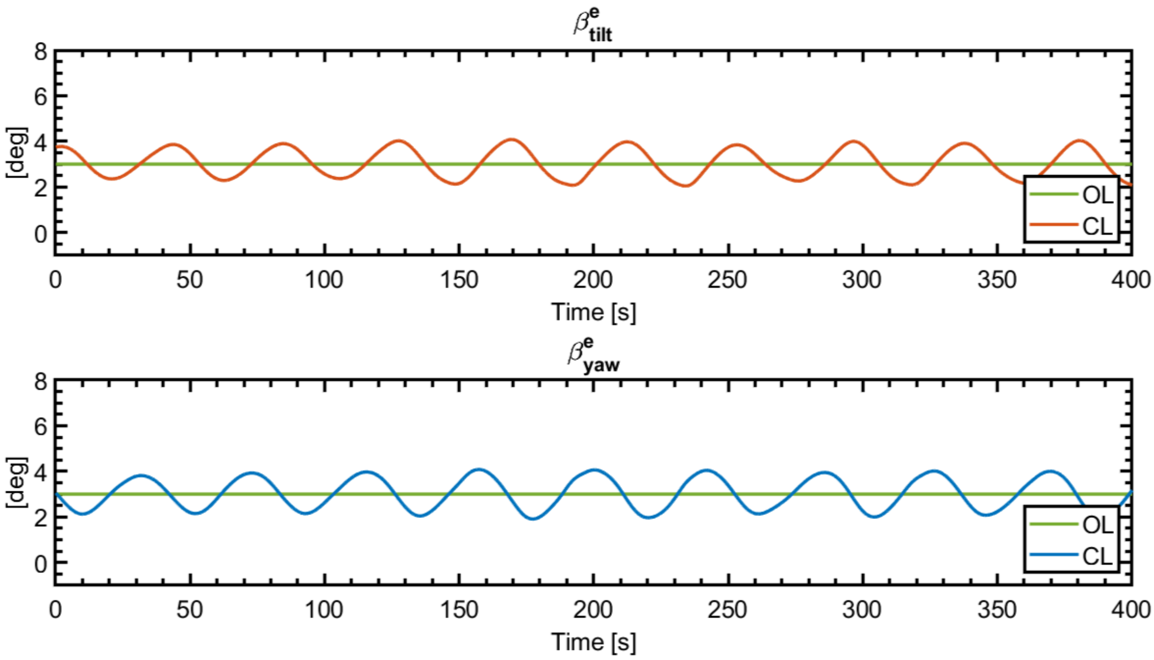

Figure 4-12: The comparison of input signals in the Helix frame between OL_2 and CL_2 with a more aggressive controller.

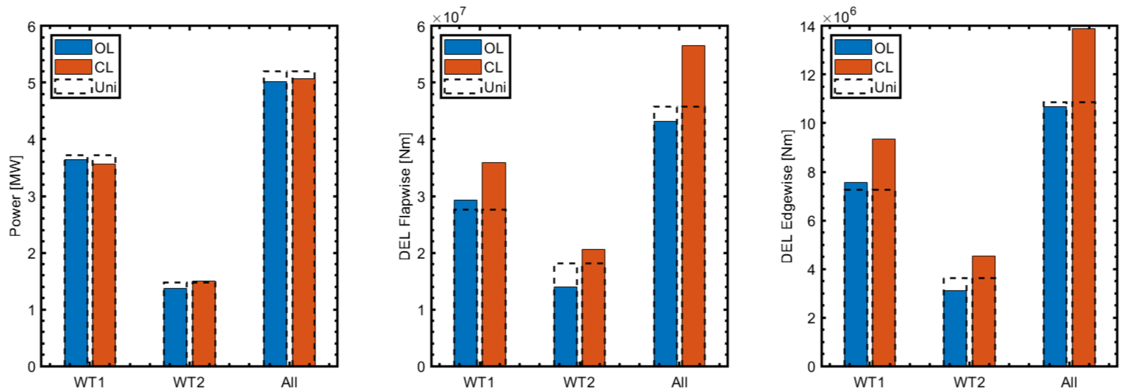

Figure 4-13: The power and DEL of OL_2 and CL_2 case compared to the reference OL_1

	WT_1	WT_2	WT_{1+2}
Power	-0.79%	$+4.96\%$	$+0.79\%$
DEL Flap-wise	$+7.40\%$	$+30.50\%$	$+14.80\%$
DEL Edge-wise	$+10.9\%$	$+20.1\%$	$+13.9\%$
PBD	$+5.67\%$	-	-
u_{in}	-	$+0.05\%$	-

Table 4-6: Summary of change of power, DEL, and PBD of case CL_2 compared to OL_2 with a more aggressive controller.

wind flow measurements at the $4D$ position downwind, which indicate that the average inflow speed of the closed-loop system is 6.27 m/s, significantly higher than the open-loop value of 5.95 m/s. Meanwhile, because of better wake mixing, the TI at the $4D$ position downwind decreases from 2.41% to 2.22%.

4-2-5 Pure Turbulence Case

As analyzed in Chapter 4-2-2, the hub jet rotation becomes more oscillating when turbulence is presented, which is expected to be stabilized by the controller. Fig. 4-14 demonstrates the trajectory of the hub jet in open-loop and closed-loop cases.

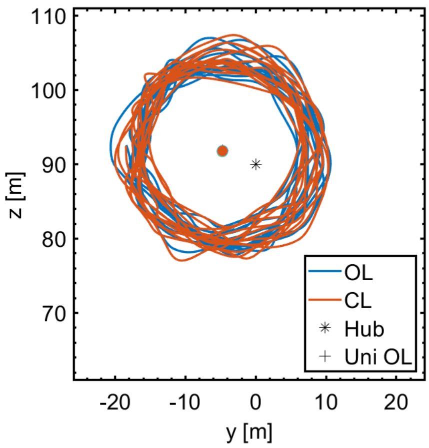

Figure 4-14: The hub jet trajectory comparison between OL_3 and CL_3.

From the figure, there is no obvious improvement of hub jet movement of CL_3 compared to OL_3. To analyze the reason, the system input and output in the Helix frame are shown in Fig. 4-15 and Fig. 4-16.

From the comparison of input signals, it is clear that the controller is trying to stabilize the hub jet. This is evident by the dynamically varying input signals compared to the constant one. However, this rectification was not successfully achieved. Consequently, Fig. 4-17 and Table 4-7 summarized the comparison between OL_3 and CL_3.

	WT_1	WT_2	WT_{1+2}
Power	+0.04%	+0.08%	+0.05%
DEL Flap-wise	−0.18%	+8.80%	+3.19%
DEL Edge-wise	−0.13%	+0.21%	−0.01%
PBD	−0.27%	-	-
u_{in}	-	+0.01%	-

Table 4-7: Summary of change of power, DEL, and PBD of case CL_3 compared to OL_3.

Both the figure and the table indicate a slight increase in the power production of both turbines. The increase of the downstream turbine is attributed to the higher average inflow speed. For the upstream turbine, the increase is linked to a smaller average blade pitch signal magnitude in CL_3 compared to OL_3. As a result, the flap-wise DEL for the upstream turbine

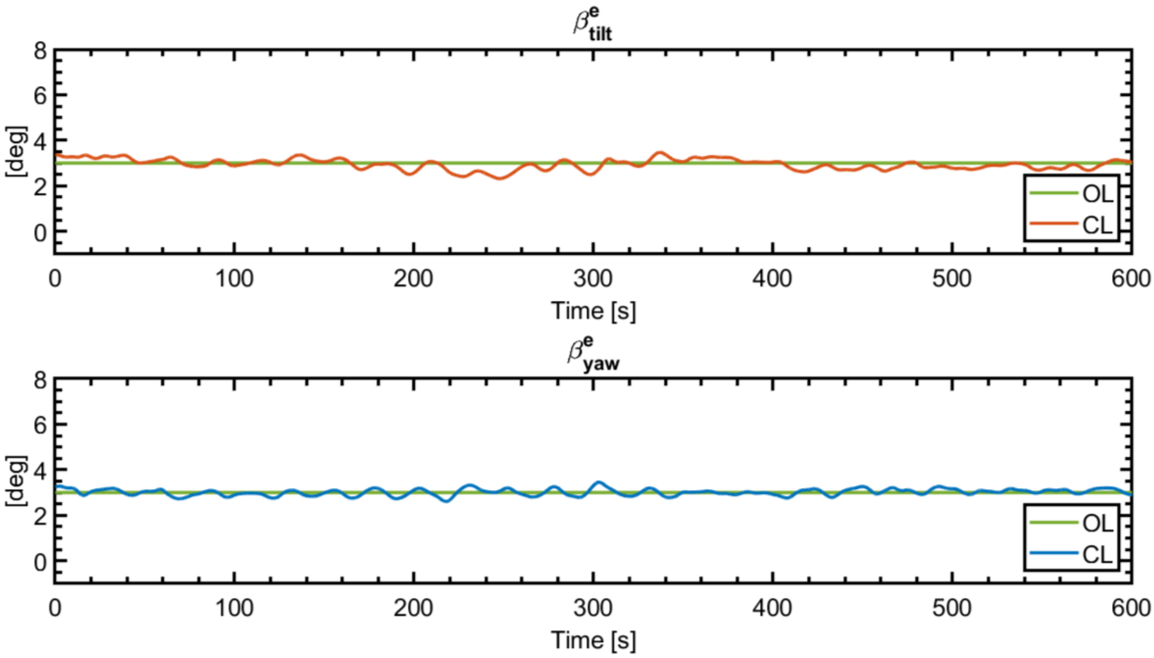

Figure 4-15: The comparison of input signals in the Helix frame between OL_3 and CL_3.

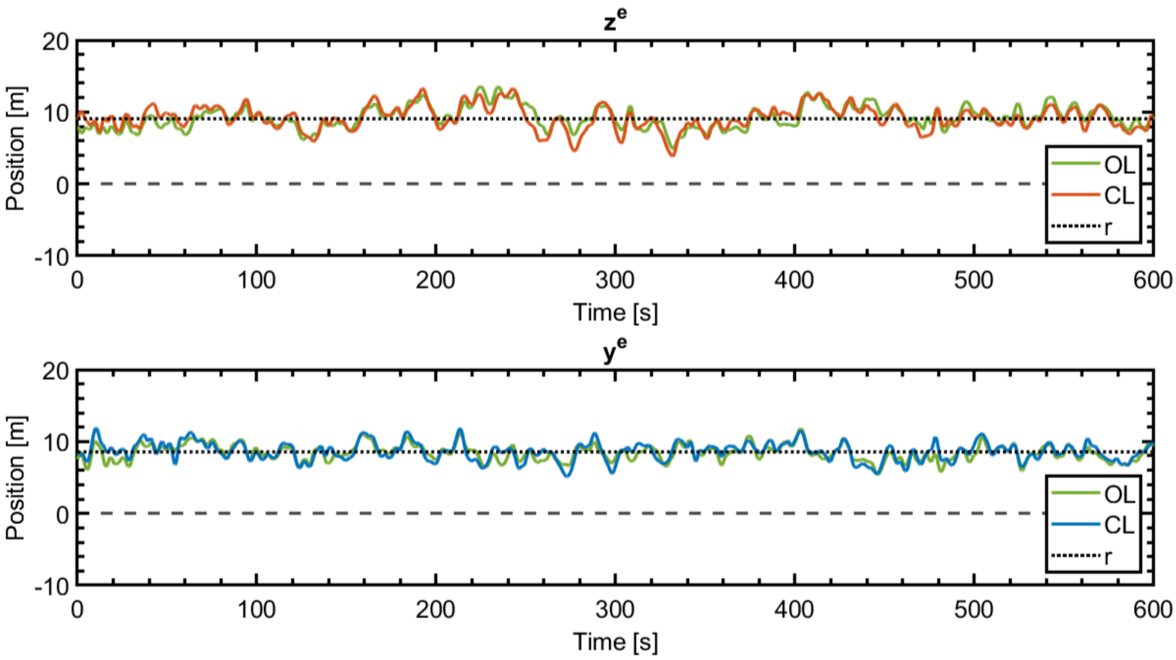

Figure 4-16: The comparison of output signals in the Helix frame between OL_3 and CL_3.

decreases, while it increases for the downstream turbine and the two turbine setup. The edgewise DEL remains nearly unchanged for both cases, consistent with the findings of [31], which highlight that edgewise DEL is less sensitive to changes in Helix magnitude. Finally, since the average blade pitch magnitude in CL_3 is lower than in OL_3, the PBD is also relatively smaller.

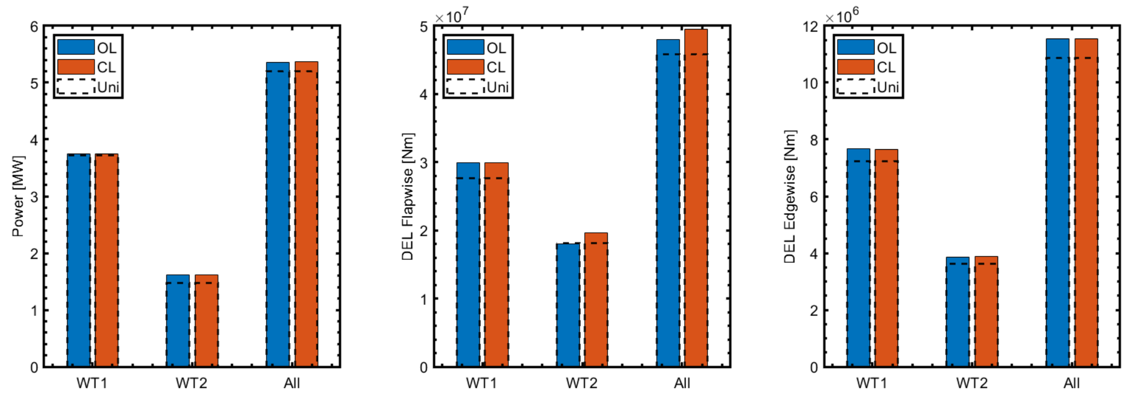

Figure 4-17: The power and DEL of OL_3 and CL_3 case compared to the reference OL_1

Based on the above analysis, the unsuccessful rectification has two potential reasons:

1. The $\mathcal{H}_\infty$ controller is designed to have a roll-off at high frequency, as Fig. 3-14 shows. This is validated by the Fast-Fourier Transform (FFT) of the output, which indicates that some content exists above the controller's roll-off frequency of 0.08 Hz. Consequently, the controller is unable to handle the high-frequency turbulence.
2. The control input u is formed based on the internal model $G(z)$, which is based on data from the uniform wind condition. Thus, the model is incapable of capturing the dynamic of $(\beta^e_{\text{tilt}}, \beta^e_{\text{yaw}}) \rightarrow (z^e, y^e)$ in the turbulent wind.

4-2-6 Shear and Turbulence Case

Finally, the shear and turbulence are added simultaneously. As analyzed, the controller should eliminate the bias introduced by the shear while stabilizing the oscillation.

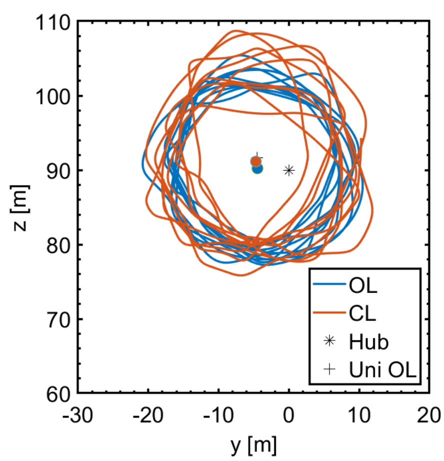

Figure 4-18: The hub jet trajectory comparison between OL_4 and CL_4.

Fig. 4-18 illustrates the hub jet trajectory. Compared to OL_4, the center of CL_4 is rectified more towards the reference. Nevertheless, the controller struggles to stabilize the oscillations as analyzed in the case of pure turbulence. The control input is shown in Fig. 4-19.

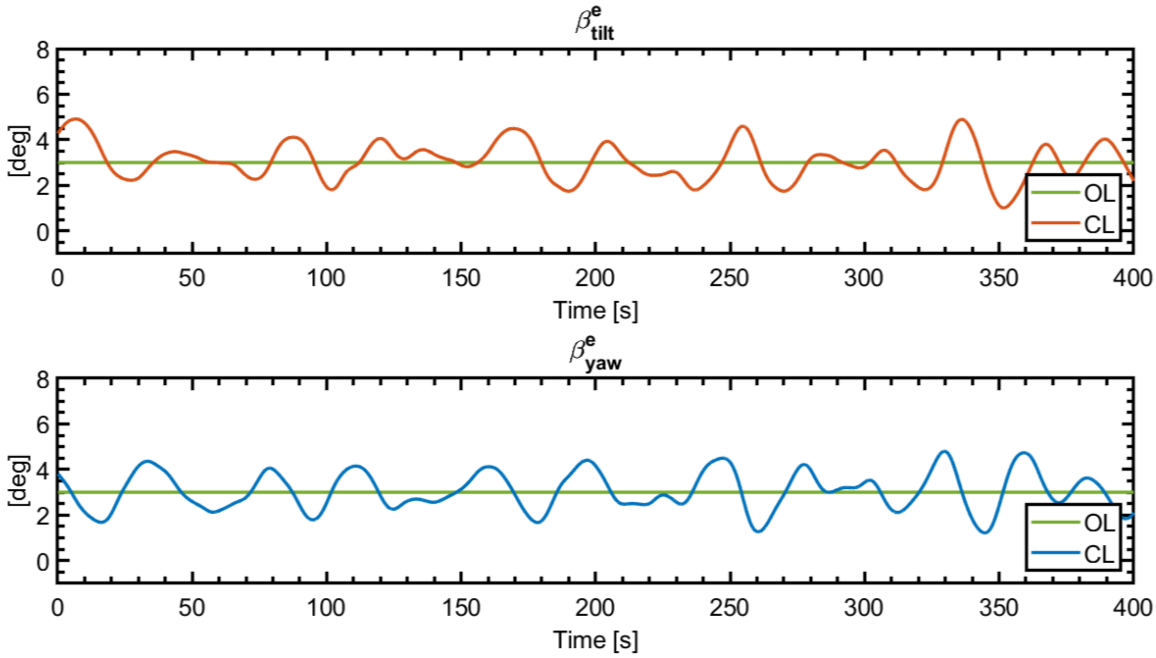

Figure 4-19: The comparison of input signals in the Helix frame between OL_4 and CL_4.

The corresponding output is demonstrated in Fig. 4-20. The above visualizations indicate that

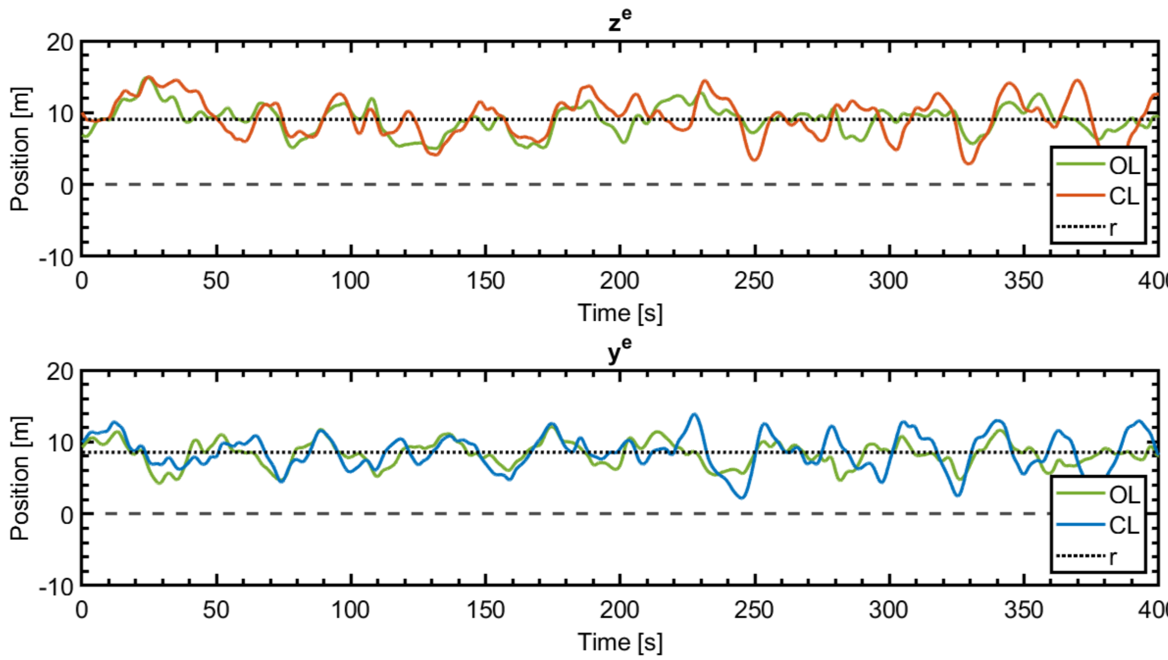

Figure 4-20: The comparison of output signals in the Helix frame between OL_4 and CL_4.

the controller behaves like the combination of case CL_2 and CL_3. As a result, the comparison between OL_4 and CL_4 are summarized in Fig. 4-21 and quantified in Table 4-8.

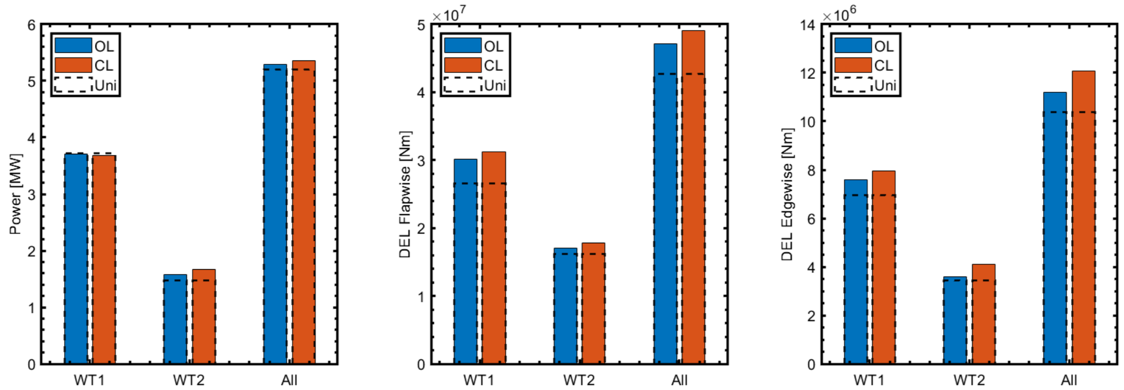

Figure 4-21: The power and DEL of OL_4 and CL_4 case compared to the reference OL_1

	WT_1	WT_2	WT_{1+2}
Power	-0.65%	$+5.89\%$	$+1.32\%$
DEL Flap-wise	$+3.83\%$	$+4.43\%$	$+4.04\%$
DEL Edge-wise	$+4.53\%$	$+14.51\%$	$+7.74\%$
PBD	$+1.17\%$	-	-
u_{in}	-	$+0.07\%$	-

Table 4-8: Summary of change of power, DEL, and PBD of case CL_4 compared to OL_4.

The figure and table show that the designed controller enhances the performance of the two-turbine setup by increasing the power production of the downstream turbine and the overall setup. However, this comes at the cost of requiring the upstream turbine to generate a larger Helix, resulting in power loss and increased fatigue. Compared to the CL_2, the power gain is larger due to stronger mixing caused by the inherent natural mixing in the turbulence [41]. This is supported by measurements at $4D$ downwind, showing that the average inflow wind speed for CL_4 is $6.60\,\mathrm{m/s}$, compared to $6.19\,\mathrm{m/s}$ for OL_4.

Chapter 5

Conclusion

This chapter presents the conclusions derived from the simulation results and outlines recommendations for future work. The first part of this chapter provides a general conclusion, followed by a discussion of the limitations of the proposed framework. Subsequently, the discussion facilitates the recommendation of future work in Chapter 5-3.

5-1 Conclusion

In this study, the closed-loop control framework for the Helix approach with a structure shown in Fig. 1-9 is designed and implemented. Simulations of the Helix activated in an open-loop manner under various wind cases reveal that the helical wake deviates from the uniform wind case as Fig. 4-1 shows. This deviation subsequently influences the performance of the two-turbine setup as Fig. 4-3 depicted. Consequently, the designed framework aims to correct those deviations in the helical wake.

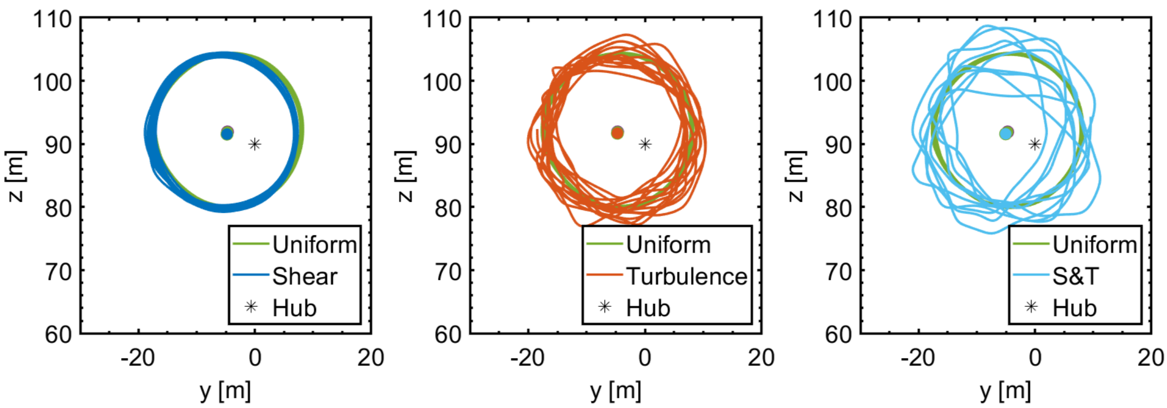

Figure 5-1: Comparison of hub jet trajectory of OL_1 to CL_2, CL_3, and CL_4.

Figure 5-1 shows the hub jet trajectory of all the closed-loop cases. Compared to the open-loop results in Fig. 4-1, *the bias induced by the shear is successfully corrected while a different type of controller needs to be developed to handle the high-frequency oscillation introduced by the turbulence.* The potential reasons are listed in Chapter 4-2-5.

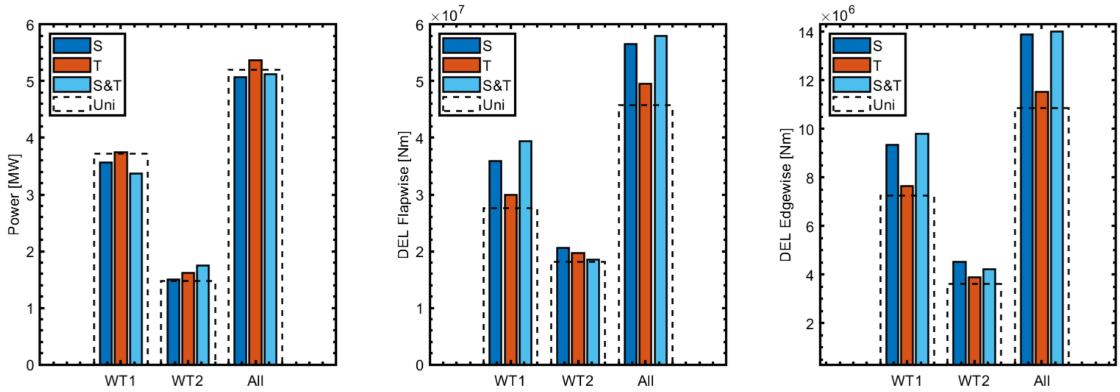

Figure 5-2: The power and Damage Equivalent Load (DEL) of CL_2 (blue), CL_3 (orange), and CL_4 (sky blue) compared to case OL_1 (dashed line).

The performance of the two-turbine setup after correction in the helical wake is summarized in Fig. 5-2. The comparison to all the open-loop counterparts in Fig. 4-3 indicates that:

1. *The power production of the downstream wind turbine generally increases, with the most notable improvements observed in cases when shear and combined shear and turbulence are presented.* This can be attributed to the correction of bias, resulting in better wake mixing. This is further supported by the samples taken at the $4D$ downwind position which shows that the average inflow speed for cases CL_2 and CL_4 is higher than that of OL_2 and OL_4, implying better wake mixing.

2. *Despite the increase in power for the second wind turbine, the overall power gain for the two-turbine setup is limited.* This is because correcting the Helix requires larger and more complex control actions from the upstream turbine. As shown in the study [31], this leads to power losses for the upstream turbine, affecting the total power production of the two-turbine setup.

3. *The increase in power production comes at the cost of higher fatigue for both turbines.* The increased fatigue in the upstream turbine is attributed to the more intensive control actions, while the downstream turbine has higher fatigue likely due to the increased wind speed resulting from improved wake mixing after correcting the Helix deviations. Therefore, a trade-off must be considered between increasing power production and reducing fatigue loads.

In summary: The primary goal of the designed framework is to correct the helical wake distortion caused by external wind conditions. First, the simulation under uniform wind conditions demonstrates that the helical wake generated by the closed-loop framework matches the counterpart generated by the original open-loop method. Furthermore, results from three different wind cases show that the controller effectively corrects the steady-state bias introduced by shear but has a mediocre performance in mitigating the high-frequency oscillations caused by turbulence. This limitation is attributed to the high-frequency roll-off feature of the designed $\mathcal{H}_\infty$ controller. Therefore, a revised controller with enhanced high-frequency responses is required to improve the performance. Correcting the Helix improves power production for the downstream turbine in the presence of shear due to enhanced mixing. However, this correction requires additional control effort from the upstream turbine, leading to reduced power output for the upstream turbine. Additionally, the results highlight a trade-off between increasing power production and reducing fatigue loads. *It is important to re-emphasize the challenge of defining a suitable reference.* This study focuses on correcting deviations in the helical wake caused by external wind conditions, thus, the hub jet rotation trajectory in the uniform wind case is given as the reference. However, this is not a universal objective. I believe that a more optimal reference could be established as our understanding of the Helix approach and its interaction with the wind turbine improves in the future.

Answer to Research Questions Now, the research questions posed at the beginning of this study can now be answered. For the primary research question:

> *How to integrate Light Detection and Ranging (LiDAR) and the Helix approach for closed-loop wake mixing control for wind farms?*

A LiDAR can be integrated into the Helix approach by using the hub jet as a measurement and controlling its rotation to regulate the Helix magnitude. In this setup, a downwind-facing LiDAR provides feedback information, enabling the design of a closed-loop control framework. This approach allows the Helix to be generated and adjusted based on flow information rather than relying on the previous open-loop method.

> *1. Which LiDAR configuration is most suitable?*

A continuous-wave LiDAR is used in this study due to its ability to capture comprehensive information at a measurement position. Certain assumptions are made regarding the scanning pattern, update frequency, and other configurations to simplify the control problem.

> *2. What specific feature in the helical wake should be controlled, and how to acquire it in real-time by using the LiDAR?*

This study focuses on controlling the $\mathrm{Z} - \mathrm{Y}$ position of the hub jet in the Helix frame. The analysis confirms that the hub jet effectively captures the key characteristics of the Helix including the frequency and magnitude, validating the approach of controlling the Helix through the hub jet. By utilizing the characteristics, the hub jet can be efficiently acquired from the LiDAR measurement by using a filter with a threshold to separate it from low-speed wind data.

> *3. How can a control system be developed to adjust the Helix in real-time using a closed-loop approach?*

The system exhibits an output delay τ due to the wake propagation time, to compensate for that, a Smith Predictor based on the Internal Model Control (IMC) is used to control the helical wake. To do so, an internal model $G(z)$ is identified using Optimized Predictor-based Subspace Identification (PBSID-opt). To control the Multiple-Input, Multiple-Output (MIMO) system, a decentralized control strategy was initially attempted by decoupling the system and designing a diagonal controller to control the separate channels. However, this approach proved ineffective. Subsequently, a sequential control method was developed, leveraging the system's inherent stability. While this method achieved reference tracking, it exhibited significant limitations, making it impractical for real-world applications. Consequently, an $\mathcal{H}_\infty$ controller is designed. The controller's design successfully ensures the closed-loop system's Nominal Stability (NS), internal stability, and Nominal Performance (NP).

As wind energy is exploring smarter solutions for control to decrease the Levelized Cost of Energy (LCoE), this method proposes a promising solution for Wind Farm Flow Control (WFFC) for providing a novel framework for implementing wake mixing with dynamic adjustments enabled by feedback information.

5-2 Limitation and Discussion

Like everything in life, perfection is unattainable. Despite being effective, limitations still exist in the designed framework. Some of the limitations stem from the assumptions that were made, while others exist because of the intrinsic nature of the designed controller, the adopted LiDAR, and the lack of prior knowledge of helical wake. Referring to the overall block diagram of the system presented in Fig. 1-9, the system consists of three parts. Thus, the limitations of the proposed system are analyzed accordingly, following the logic of the system structure.

Limitation on LiDAR System

- **LiDAR** This study assumes a perfect continuous wave LiDAR capable of acquiring the information of the measurement plant perfectly. However, that assumption does not hold in reality. In practice, LiDAR is unable to capture complete information simultaneously about the measurement plant. Instead, the LiDAR updates information in an update frequency [69]. Consequently, the assumptions made regarding the LiDAR system introduce limitations for applying the proposed method directly to a real wind turbine.
- **Hub Jet** The hub jet is selected experimentally as a feature to be controlled in the Helix. However, this experimental method yields three problems:
    1. Acquiring the hub jet needs the measurement data of the entire plant, which is not viable in practice.
    2. The hub jet is characterized by a region of high-speed wind surrounded by slow-speed wind, making it relatively easy to access in cases where turbulence is not strong. However, when the turbulence intensity is high, the hub jet is almost impossible to capture using the method in this study as the wind speed distribution

becomes chaotic. Figure 5-3 illustrates the snapshot of LiDAR sample for both uniform and turbulent wind cases. For comparison, the average inflow speed is kept identical to 10 m/s, while a class 'A' turbulence is added to the turbulence case according to [3]. The result reveals the chaotic distribution of wind speed when turbulence exists, increasing the difficulty of capturing the hub jet.

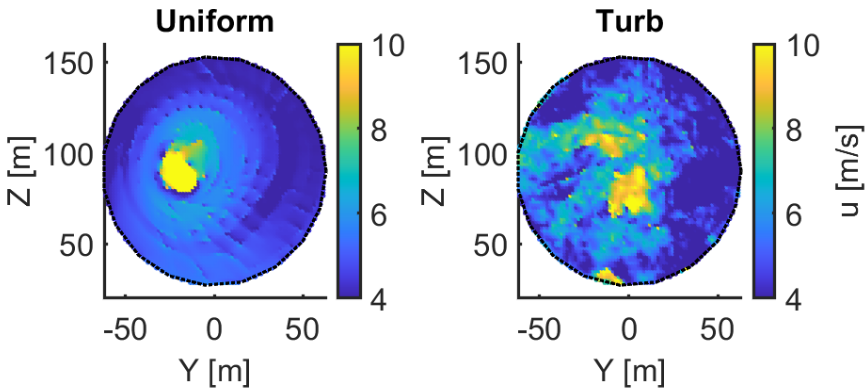

Figure 5-3: LiDAR sampling snapshot at $t = 100$ seconds for uniform and turbulent wind case.

3. Apart from the accessibility issue, the selection of the hub jet is not based on a systematic feature engineering process. A feature is a coherent and identifiable bundle of system functionality that helps characterize the system from the user's perspective [70]. Therefore, a better way involves linking the to-be-controlled feature with the aerodynamic feature that reflects the effectiveness of wake recovery.

These three problems hinder the further implementation of the proposed method on a real wind turbine.

- **Delay** For simplicity, the output delay τ is assumed to be constant and follows Taylor's frozen turbulence assumption [52]. However, in practice, these assumptions are not necessarily fulfilled. For instance, the constantly changing wind speed makes the estimation of τ adopted in this work invalid.

- **Measurement Position** The measurement position of the LiDAR is set to $1D$ in this research. However, in scenarios where turbines are positioned further away from the upstream turbines, say $5D$, the region of interest may extend beyond $1D$. Thus, this could limit the application of the proposed approach in practice.

Limitation on Control System

- **Reference** As reiterated previously, there is no universally optimal reference. This study adopts the simplest reference, based on the assumption that the main goal is to correct deviations in the Helix caused by external wind conditions. However, this reference lacks information related to wind farm performance. Therefore, it is suggested that a more suitable reference be given to the closed-loop system once insights into the Helix and its interaction with wind turbine performance are clearer.

- **Large Overshoot** The step response of the system reveals a large overshoot and a long settling time as analyzed in Chapter 3-5. The former brings more loads to the blade and the pitch bearing as Eq. 4-1 and 4-2 shows. Consequently, the controller can be fine-tuned to improve the performance. For instance, increase the upper bound of controller sensitivity U to increase the controller gain while maintaining stability under the existence of the non-minimum phase zero.

- **Robustness** The $\mathcal{H}_\infty$ controller designed in this research does not consider uncertainty. However, uncertainty is ubiquitous. Thus, when applying this method to a real wind turbine, the $\mathcal{H}_\infty$ controller should be redesigned. Consequently, the Robust Performance (RP) and Robust Stability (RS) should also be examined.

- **Model-based Control** The entire control is based on a Linear Time Invariant (LTI) model. This simplifies the control problem but also restricts the operational range of the system due to the range of linearization. Therefore, for practical implementation, it is advisable to conduct system identification at different operational points and employ gain scheduling. Additionally, the accuracy may degrade under the presence of turbulence and shear. Thus, a nonlinear model could result in a more accurate representation of the system dynamic.

- **No Constraints on Input** While this method does not entirely neglect control input constraints as the weight function $W_U(s)$ is designed to avoid high-gain instability, the designed controller could generate control inputs that shift rapidly. This fast-changing blade pitch signal β_i will result in a higher Pitch Bearing Damage (PBD). Thus, it would be beneficial to design a controller while considering input constraints.

- **Phase Shift** As Eq. A-8 in the Appendix A demonstrates, changing either β^e_{tilt} and β^e_{yaw} in the Helix frame results in a changing phase of β_{tilt} and β_{yaw} in the fixed frame while the phase difference between β_{tilt} and β_{yaw} remains the same. This is not problematic for this work as the primary objective is to track the magnitude of rotation. However, in studies where precise phase information is crucial, such as phase synchronization in [71], this could pose a challenge. Therefore, the changing phase requires further consideration when applying in practice.

Limitation on the Overall System

- **Only Magnitude** This study focuses merely on adjusting the Helix magnitude. This gives the impression that the proposed method is redundant compared to the existing open-loop strategy. This is because the primary goal here is to establish a foundational framework, so only the Helix magnitude is considered. Nevertheless, focusing solely on magnitude control can indeed seem simplistic. Therefore, extending this approach to explore additional control objectives would be worthwhile.

- **Latency between LiDAR and Control** This study is based merely on simulations and does not consider the latency issues that might arise when implemented in practice. Therefore, it appears as a limitation for the overall system.

- **Only Circle** The Helix frame transformation adopted in this study restricts its control to producing a Helix that rotates in a perfect circle. However, what if a more diverse Helix is desired? An ellipse? or even a flower?

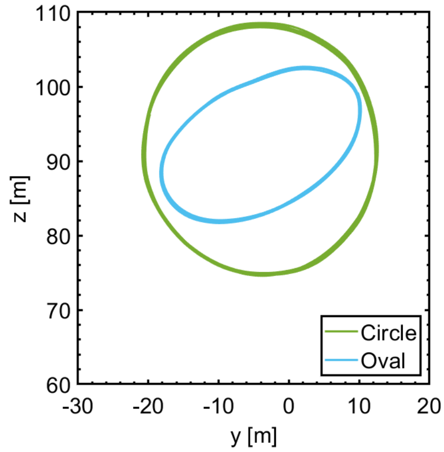

Figure 5-4: Oval Helix.

Fig. 5-4 illustrates a Helix rotating in an elliptical pattern, the corresponding blade pitch input signal in the fixed frame is also shown in Fig. 5-5. Compared to the circle

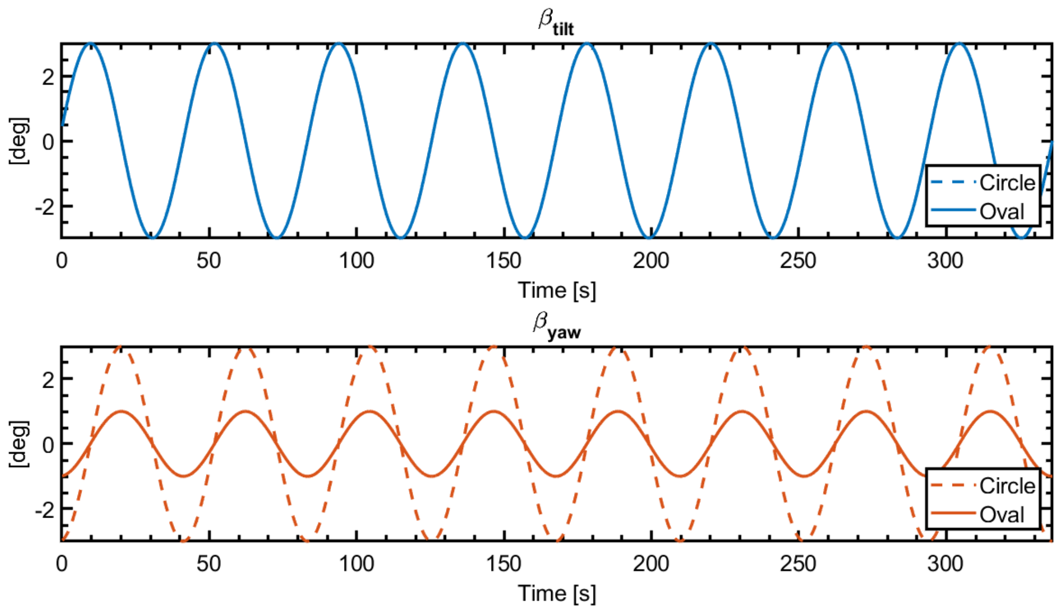

Figure 5-5: Input signal corresponding to an oval Helix.

Helix, denoted in the color blue, the input signals now have different magnitudes. This difference in input magnitude of the two channels can be explained by the mathematical formula of an oval, which is shown below

$$\frac{x^2}{a^2} + \frac{y^2}{b^2} = 1. \tag{5-1}$$

Correspondingly, to enable this flexibility, the Helix frame transform needs to be modified to Eq. 5-2. This modified transformation is different from Eq. 2-8 as the rotational matrix $R(\omega_e t)$ is switched to $R^{'}(\omega_e t)$ in which two scaling factors a and b for the two principle axes are introduced. Furthermore, to rectify a more diver Helix, the rotational matrix $R^{'}(\omega_e t)$ is expected to be more complicated:

$$\begin{bmatrix} \beta^e_{\text{col}}(t) \\ \beta^e_{\text{tilt}}(t) \\ \beta^e_{\text{yaw}}(t) \end{bmatrix} = \underbrace{\begin{bmatrix} 1 & 0 & 0 \\ 0 & a \cdot \cos(\omega_e t) & -b \cdot \sin(\omega_e t) \\ 0 & a \cdot \sin(\omega_e t) & b \cdot \cos(\omega_e t) \end{bmatrix}}_{R^{'}(\omega_e t)} \times \underbrace{\frac{2}{3} \cdot \begin{bmatrix} 1/2 & 1/2 & 1/2 \\ \cos\psi_1 & \cos\psi_2 & \cos\psi_3 \\ \sin\psi_1 & \sin\psi_2 & \sin\psi_3 \end{bmatrix}}_{T(\omega_r t)} \cdot \begin{bmatrix} \beta_1(t) \\ \beta_2(t) \\ \beta_3(t) \end{bmatrix}. \tag{5-2}$$

Lastly, a Helix is created that rotates so that the pattern of the hub jet resembles a flower as Fig. 5-6 shows. This further shows the promising future of creating a more flexible Helix.

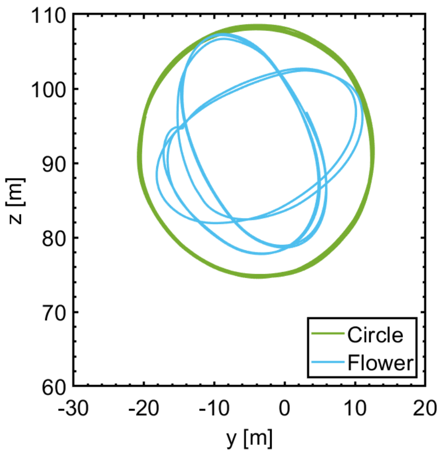

Figure 5-6: Flower Helix.

5-3 Future Work and Recommendations

Based on the above analysis, several potential future works and recommendations can be proposed for enhancement. These recommendations are written in an identical pattern as Chapter 5-2, following the logic of the overall system structure.

- **LiDAR System** This work uses an ideal continuous-wave LiDAR, limiting the practicality of the proposed framework. Furthermore, the selection of the hub jet as the control feature is primarily based on observation rather than rigorous feature engineering where the chosen feature would be more directly correlated with system performance. Thus, it is recommended to:

  1. Adopt a more realistic LiDAR for practical implementation. Moreover, explore the possibility of using a pulsed LiDAR since it offers the information of an entire field instead of a specific plant.

2. Explore a stricter definition of the Helix center, for instance, the center of mass definition as Eq. 5 in the work [72] shows. his approach could help address the challenge of accurately determining the hub jet position under strong turbulence conditions as the previous analysis shows.
3. Have a better estimation of the delay factor τ in the system identification process. Consequently, this more precise information about the system is essential for designing a more effective controller, which will ultimately enhance the overall performance and quality of the control system.

- **Control System** To simplify the development of the framework, several assumptions regarding the output delay have been made. Although these assumptions facilitate the controller design, they also lead to a loss in some system dynamics. Moreover, due to the presence of unstable zeros, the $\mathcal{H}_\infty$ controller is designed to have a roll-off feature at high frequency. This guarantees the stability. However, the conservative design constrains the controller's full potential. Thus, to address these limitations, it is recommended to:

  1. Apply a better real approximation to decouple the MIMO system at the bandwidth frequency. This enables decentralized control, making implementation easier in practice.
  2. Design a robust controller by adding a bounded uncertainty in the design process of the $\mathcal{H}_\infty$ controller.
  3. Explore the option of optimization-based controlled like Linear Quadratic Regulator (LQR) and Model Predictive Controller (MPC) to add constraints on control inputs. Moreover, quantify multiple objectives of control in an optimization framework.
  4. Explore the option of gain scheduling, adaptive control, and data-driven control to increase the generalization of the designed control system.

- **Overall System** Finally, the overall framework is developed and simulated using a mid-fidelity platform. This decision is made based on the available computational resources. While the choice accelerates the development process, it limits the deeper understanding of the proposed framework in wind farms' performance. Additionally, because of the lack of prior knowledge regarding the interaction between the Helix and the wind farm's performance, the reference trajectory used in all closed-loop cases was based on the open-loop hub jet trajectory under uniform wind conditions. However, as emphasized previously, this reference is not universally optimal. Therefore, to comprehensively test the proposed framework and further enhance a better performance, below are the suggested works:

  1. This work uses QBlade to simulate multiple turbine scenarios. As analyzed in Appendix B, QBlade has its own limitations. Moreover, the QBlade platform does not provide access to data on the wind turbine tower response, which is an important aspect to consider. Consequently, it is highly recommended to test the proposed framework in a higher fidelity platform of Large Eddy Simulation (LES), the physical experiment setup, and in multiple turbulence seeds for a comprehensive analysis.

2. Adopt better feature engineering when defining the control problem. This integration of the prior knowledge of wake is believed to enhance the interpretability of the control problem.
3. In this work, the Open-Loop (OL) Helix under a uniform wind of magnitude 3 is used as the reference. However, this assumption may not always hold. Therefore, further investigation is needed to determine a better reference for different wind conditions. In other words, determining the optimal positioning of the Helix to satisfy the specific requirements remains an open research question.
4. Explore the option of controlling the Helix more diversely as the oval and flower Helix show.
5. Explore the difference between the application of the closed-loop system to a Counterclockwise (CCW) Helix and a Clockwise (CW) Helix.
6. Integrate the proposed framework with existing methods, such as phase synchronization [71]. This could further harness the full potential of the designed framework.

Appendix A

Helix Frame Transform

This appendix is created to explain the Helix frame transform. The goal of this appendix is to answer two questions:

1. Why does Helix frame transform work?
2. Why a detrend is needed before applying the Helix frame transform?

Assume two tilt and yaw pitch signals β_{tilt} and β_{yaw} defined in the fixed frame generating the Counterclockwise (CCW) Helix, meaning that the phase difference between β_{tilt} and β_{yaw} equals $-\pi/2$ as defined in Eq. A-1:

$$\begin{aligned} \beta_{\text{tilt}} &= A\sin(\omega_e t + \theta) \\ \beta_{\text{yaw}} &= A\sin(\omega_e t + \theta - \frac{\pi}{2}). \end{aligned} \tag{A-1}$$

Consequently, the corresponding β^e_{tilt} and β^e_{yaw} in the Helix frame can be obtained by applying Eq. 2-8 in which a rotation matrix $R(\omega_e t)$ is multiplied to the original signal, characterized by below equation

$$\begin{bmatrix} \beta^e_{\text{tilt}} \\ \beta^e_{\text{yaw}} \end{bmatrix} = \begin{bmatrix} \cos(\omega_e t) & -\sin(\omega_e t) \\ \sin(\omega_e t) & \cos(\omega_e t) \end{bmatrix} \begin{bmatrix} \beta_{\text{tilt}} \\ \beta_{\text{yaw}} \end{bmatrix}. \tag{A-2}$$

Consequently, β^e_{tilt} and β^e_{yaw} can be written as

$$\begin{aligned} \beta^e_{\text{tilt}} &= \cos(\omega_e t) \cdot \beta_{\text{tilt}} - \sin(\omega_e t) \cdot \beta_{\text{yaw}} \\ \beta^e_{\text{yaw}} &= \sin(\omega_e t) \cdot \beta_{\text{tilt}} + \cos(\omega_e t) \cdot \beta_{\text{yaw}}. \end{aligned} \tag{A-3}$$

By using the trigonometric addition law, Eq. A-3 can be further written into

$$\begin{aligned} \beta^e_{\text{tilt}} &= \sqrt{\beta^2_{\text{tilt}} + \beta^2_{\text{yaw}}} \cdot \cos(\omega_e t + \arctan(\frac{\beta_{\text{yaw}}}{\beta_{\text{tilt}}})) \\ \beta^e_{\text{yaw}} &= \sqrt{\beta^2_{\text{tilt}} + \beta^2_{\text{yaw}}} \cdot \sin(\omega_e t + \arctan(\frac{\beta_{\text{yaw}}}{\beta_{\text{tilt}}})) \end{aligned} \tag{A-4}$$

and because the definition of β_{tilt} and β_{yaw} are constrained to Eq. A-1, the arctan part of Eq. A-4 equals

$$\arctan(\frac{\beta_{\text{yaw}}}{\beta_{\text{tilt}}}) = \arctan\left[\frac{-A\cos(\omega_e t+\theta)}{A\sin(\omega_e t+\theta)}\right] = \frac{\pi}{2} - (\omega_e t+\theta) \tag{A-5}$$

by using the result of Eq. A-5, β^e_{tilt} and β^e_{yaw} in Eq. A-4 can be written as

$$\begin{aligned} \beta^e_{\text{tilt}} &= \underbrace{\sqrt{\beta^2_{\text{tilt}}+\beta^2_{\text{yaw}}}}_{\hat{A}} \cdot \cos(\frac{\pi}{2}-\theta) \\ \beta^e_{\text{yaw}} &= \underbrace{\sqrt{\beta^2_{\text{tilt}}+\beta^2_{\text{yaw}}}}_{\hat{A}} \cdot \sin(\frac{\pi}{2}-\theta). \end{aligned} \tag{A-6}$$

Eq. A-6 answers the two questions at the beginning of this chapter nicely:

1. Because $\cos(\frac{\pi}{2}-\theta)$, $\sin(\frac{\pi}{2}-\theta)$, and $\hat{A}$ are all constant values, β^e_{tilt} and β^e_{yaw} are constant values. Therefore, we successfully transfer rotating signals into constant signals.
2. Detrend is crucial to guarantee signals β_{tilt} and β_{yaw} have the form of Eq. A-1. Otherwise, it brings an additional rotating component to signal β^e_{tilt} and β^e_{yaw}. One can easily derive that by adding a bias B to the β_i definition and following the same computation procedure as this appendix provides.

By adopting the same logic, the inverse Helix frame transform can be analyzed

$$\begin{bmatrix}\beta_{\text{tilt}} \\ \beta_{\text{yaw}}\end{bmatrix} = \begin{bmatrix}\cos(\omega_e t) & \sin(\omega_e t) \\ -\sin(\omega_e t) & \cos(\omega_e t)\end{bmatrix}\begin{bmatrix}\beta^e_{\text{tilt}} \\ \beta^e_{\text{yaw}}\end{bmatrix} \tag{A-7}$$

with the same procedure, the pitch signal β_{tilt} and β_{yaw} in the fixed frame can be written as

$$\begin{aligned} \beta_{\text{tilt}} &= \sqrt{\beta^{e2}_{\text{tilt}}+\beta^{e2}_{\text{yaw}}} \cdot \sin(\omega_e t + \arctan(\frac{\beta^e_{\text{yaw}}}{\beta^e_{\text{tilt}}})) \\ \beta^e_{\text{yaw}} &= \sqrt{\beta^{e2}_{\text{tilt}}+\beta^{e2}_{\text{yaw}}} \cdot \cos(\omega_e t + \arctan(\frac{\beta^e_{\text{yaw}}}{\beta^e_{\text{tilt}}})). \end{aligned} \tag{A-8}$$

Eq. A-8 reveals that changing the pitch signal in the Helix frame changes both the magnitude and phase of the signal in the fixed frame. However, the phase difference between the β_{tilt} and β_{yaw} remains the same as Eq. A-8 demonstrates.

Appendix B

QBlade Simulation Setup

In this chapter, the wake and vortex modeling of QBlade is introduced. QBlade uses the free-vortex method to simulate the flow field. This method is known for its accuracy in the near wake and being computationally more efficient than the Large Eddy Simulation (LES) methods. However, free-wake vortex methods are prone to numerical instability, especially in the far-wake region [41]. In this study, this could be a problem when testing the proposed method in a 2 turbine setup. Additionally, QBlade does not guarantee the accuracy of two turbine simulations. Thus, it is highly recommended that the closed-loop Helix approach be tested in a higher fidelity platform.

The QBlade setup for aerodynamic simulation in this work is chosen under the principle of finding a trade-off between computational time and accuracy. In the free-wake vortex method, this trade-off is primarily dictated by the number of vortex elements in the wake, as computational time grows exponentially with the number of wake elements [41]. The settings that influence computational time and wake accuracy are divided into two groups:

1. Wake Modeling Settings
2. Vortex Modeling Settings

The former directly regulates the number of elements in the wake while the latter are settings that influence vortex performance.

Wake Modeling Settings The parameters for wake modeling are presented in Table B-1. In QBlade, the wake is cut off when either the maximum number of wake elements or the maximum wake distance is reached [41]. The wake relaxation setting influences the blending of the initial vortex and subsequently affects the wake length. When this option is turned on, the resulting Helix wake is insufficient for accurate evaluation. Hence, this option is disabled in this study. The wake reduction factor, setting to 0.001 as QBlade default, determines the removal of wake elements based on their relative vorticity strength compared to newly

Description	Value
Wake Relaxation	1 (No Relaxation)
Max. Wake Elements	200 000
Max. Wake Distance	100 Rotor Diameters
Wake Reduction Factor	0.001
Near-Wake Length	0.5 Revolutions
Wake Zone 1/2/3 Length	6/12/6 Revolutions
Simulation Time Step	0.1 seconds

Table B-1: Wake modeling settings of QBlade adopted in this study.

generated vortices. Consequently, the final length of the wake is primarily determined by a balance between these parameters.

In QBlade, the full wake is subdivided into four distinct areas as Fig. B-1 illustrates.

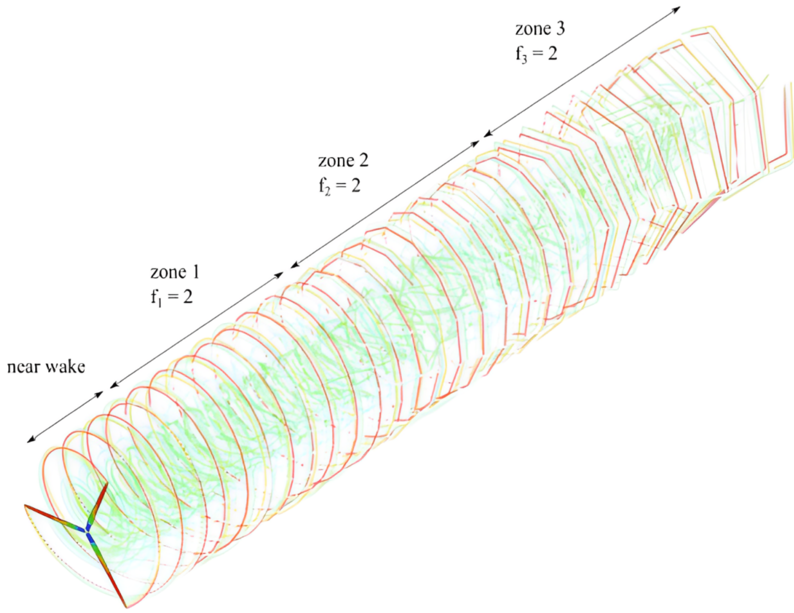

Figure B-1: Wake zone settings in QBlade. Figure adapted from the QBlade official website.

The near wake region refers to a highly resolved region of the wake immediately downstream of the turbine, influencing the performance of the turbine predominately. For accuracy, the length of the near wake region is typically set to half a rotor diameter [73]. Beyond the near wake, the wake transitions into wake zone 1, followed by zones 2 and 3 consecutively where the wake is increasingly sparsely resolved [41]. As the wake travels among zones, vortex filaments are merged to reduce the number of wake elements, resulting in an increase in computational efficiency. These wake zones are defined in terms of turbine revolutions, which, can be translated to a physical distance based on the average velocity in the wake. The study of [41] investigated the effect of different wake zone lengths on the velocity using a grid search method. The study found that the transition of wake to zone 2 impacts the wake stability slightly and results in a small increase in wind speed. Nevertheless, keeping the velocity field of interest in zone 2 seems to provide a trade-off between accuracy and computational time [41]. Thus, this study adopted the wake zone length of 6, 12, and 6 respectively for zone 1, 2, and 3. This configuration is the same as the work of [41] since the 2 turbine setup is identical.

Vortex Modeling Settings Finally, settings that influence vortex modeling are summarized in the below table. The shown parameters are majorly the default setting of QBlade.

Description	Value
Initial Core Radius	0.05 % Chord
Vortex Viscosity	800
Vortex Strain	Disabled
Trailing Vortices	Enabled
Shed Vortices	Enabled

Table B-2: Vortex modeling settings of QBlade adopted in this study

As the table shows, the initial core radius is kept as the 0.05% of the chord as it significantly impacts wake stability. Generally speaking, a larger core radius enhances stability. However, having a too-large core size can also limit the wake mixing dynamics [41]. The vortex viscosity is set to 800 to achieve a balance between wake modeling accuracy and computational efficiency. Lastly, both trailing and shed vortices are activated to improve the precision of the wake representation.

Bibliography

[1] Fernando Porté-Agel, Majid Bastankhah, and Sina Shamsoddin. "Wind-turbine and wind-farm flows: a review". In: *Boundary-layer meteorology* 174.1 (2020), pp. 1–59.

[2] Daniel R Houck. "Review of wake management techniques for wind turbines". In: *Wind Energy* 25.2 (2022), pp. 195–220.

[3] Tony Burton et al. *Wind energy handbook*. John Wiley & Sons, 2011.

[4] Takanori Uchida. "Effects of inflow shear on wake characteristics of wind-turbines over flat terrain". In: *Energies* 13.14 (2020), p. 3745.

[5] Martin Hansen. *Aerodynamics of wind turbines*. Routledge, 2015.

[6] H Korb, H Asmuth, and S Ivanell. "The characteristics of helically deflected wind turbine wakes". In: *Journal of Fluid Mechanics* 965 (2023), A2.

[7] Johan Meyers et al. "Wind farm flow control: prospects and challenges". In: *Wind Energy Science Discussions* 2022 (2022), pp. 1–56.

[8] Sjoerd Boersma et al. "A tutorial on control-oriented modeling and control of wind farms". In: *2017 American control conference (ACC)*. IEEE. 2017, pp. 1–18.

[9] Kenneth Thomsen and Poul Sørensen. "Fatigue loads for wind turbines operating in wakes". In: *Journal of wind engineering and industrial aerodynamics* 80.1-2 (1999), pp. 121–136.

[10] MS Adaramola and P-Å Krogstad. "Experimental investigation of wake effects on wind turbine performance". In: *Renewable energy* 36.8 (2011), pp. 2078–2086.

[11] Andrew Kusiak and Zhe Song. "Design of wind farm layout for maximum wind energy capture". In: *Renewable energy* 35.3 (2010), pp. 685–694.

[12] Andrew Scholbrock et al. "Lidar-enhanced wind turbine control: Past, present, and future". In: *2016 American Control Conference (ACC)*. IEEE. 2016, pp. 1399–1406.

[13] Mahmoud Huleihil and Gedalya Mazor. "Wind turbine power: The betz limit and beyond". In: *Advances in wind power*. IntechOpen, 2012.

[14] MA Yurdusev, RAŞİT Ata, and NS Çetin. "Assessment of optimum tip speed ratio in wind turbines using artificial neural networks". In: *Energy* 31.12 (2006), pp. 2153–2161.

[15] J Jonkman. “Definition of a 5-MW Reference Wind Turbine for Offshore System Development”. In: *National Renewable Energy Laboratory* (2009).

[16] Evan Gaertner et al. *IEA wind TCP task 37: definition of the IEA 15-megawatt offshore reference wind turbine.* Tech. rep. National Renewable Energy Lab.(NREL), Golden, CO (United States), 2020.

[17] Daan van der Hoek et al. “Effects of axial induction control on wind farm energy production-a field test”. In: *Renewable energy* 140 (2019), pp. 994–1003.

[18] Pieter MO Gebraad, Paul A Fleming, and Jan-Willem van Wingerden. “Comparison of actuation methods for wake control in wind plants”. In: *2015 american control conference (ACC).* IEEE. 2015, pp. 1695–1701.

[19] Luis A Martínez-Tossas et al. “Numerical investigation of wind turbine wakes under high thrust coefficient”. In: *Wind Energy* 25.4 (2022), pp. 605–617.

[20] Ali C Kheirabadi and Ryozo Nagamune. “A quantitative review of wind farm control with the objective of wind farm power maximization”. In: *Journal of Wind Engineering and Industrial Aerodynamics* 192 (2019), pp. 45–73.

[21] Wim Munters and Johan Meyers. “Towards practical dynamic induction control of wind farms: analysis of optimally controlled wind-farm boundary layers and sinusoidal induction control of first-row turbines”. In: *Wind Energy Science* 3.1 (2018), pp. 409–425.

[22] Joeri A Frederik et al. “The helix approach: Using dynamic individual pitch control to enhance wake mixing in wind farms”. In: *Wind Energy* 23.8 (2020), pp. 1739–1751.

[23] Sherif El-Henaoui. “Individual pitch control and its impact”. In: *Wind Systems Magazine* 5 (2012), pp. 1–6.

[24] Gunjit Bir. “Multi-blade coordinate transformation and its application to wind turbine analysis”. In: *46th AIAA aerospace sciences meeting and exhibit.* 2008, p. 1300.

[25] Gunjit S Bir. “User’s guide to MBC3: Multi-blade coordinate transformation code for 3-bladed wind turbine”. In: (2010).

[26] Sebastiaan Paul Mulders et al. “Analysis and optimal individual pitch control decoupling by inclusion of an azimuth offset in the multiblade coordinate transformation”. In: *Wind Energy* 22.3 (2019), pp. 341–359.

[27] Wim Munters and Johan Meyers. “An optimal control framework for dynamic induction control of wind farms and their interaction with the atmospheric boundary layer”. In: *Philosophical Transactions of the Royal Society A: Mathematical, Physical and Engineering Sciences* 375.2091 (2017), p. 20160100.

[28] Joeri Alexis Frederik et al. “Periodic dynamic induction control of wind farms: proving the potential in simulations and wind tunnel experiments”. In: *Wind Energy Science* 5.1 (2020), pp. 245–257.

[29] Jay P Goit and Johan Meyers. “Optimal control of energy extraction in wind-farm boundary layers”. In: *Journal of Fluid Mechanics* 768 (2015), pp. 5–50.

[30] Ahmed Lasheen and Abdel Latif Elshafei. “Wind-turbine collective-pitch control via a fuzzy predictive algorithm”. In: *Renewable energy* 87 (2016), pp. 298–306.

[31] Aemilius AW Van Vondelen et al. “Enhanced wake mixing in wind farms using the Helix approach: A loads sensitivity study”. In: *2023 American Control Conference (ACC)*. IEEE. 2023, pp. 831–836.

[32] Bart M Doekemeijer, Daan van der Hoek, and Jan-Willem van Wingerden. “Closed-loop model-based wind farm control using FLORIS under time-varying inflow conditions”. In: *Renewable Energy* 156 (2020), pp. 719–730.

[33] Steffen Raach, David Schlipf, and Po Wen Cheng. “Lidar-based wake tracking for closed-loop wind farm control”. In: *Wind Energy Science* 2.1 (2017), pp. 257–267.

[34] David Schlipf et al. “Prospects of optimization of energy production by lidar assisted control of wind turbines”. In: (2011).

[35] Paul A Fleming et al. “Field-test results using a nacelle-mounted lidar for improving wind turbine power capture by reducing yaw misalignment”. In: *Journal of Physics: Conference Series*. Vol. 524. 1. IOP Publishing. 2014, p. 012002.

[36] M Harris, M Hand, and A Wright. *Lidar for Turbine Control: March 1, 2005-November 30, 2005*. Tech. rep. National Renewable Energy Lab.(NREL), Golden, CO (United States), 2006.

[37] Torben Mikkelsen. “Lidar-based research and innovation at DTU wind energy–a review”. In: *Journal of Physics: Conference Series*. Vol. 524. 1. IOP Publishing. 2014, p. 012007.

[38] EA Bossanyi, Avishek Kumar, and Oscar Hugues-Salas. “Wind turbine control applications of turbine-mounted LIDAR”. In: *Journal of Physics: Conference Series*. Vol. 555. 1. IOP Publishing. 2014, p. 012011.

[39] Eric Simley et al. “Analysis of wind speed measurements using continuous wave LIDAR for wind turbine control”. In: *49th AIAA Aerospace Sciences Meeting including the New Horizons Forum and Aerospace Exposition*. 2011, p. 263.

[40] David Marten. “QBlade: a modern tool for the aeroelastic simulation of wind turbines”. In: (2020).

[41] Daniel van den Berg, Delphine De Tavernier, and Jan-Willem van Wingerden. “The dynamic coupling between the pulse wake mixing strategy and floating wind turbines”. In: *Wind Energy Science* 8.5 (2023), pp. 849–864.

[42] Takeshi Ishihara, Atsushi Yamaguchi, and Muhammad Waheed Sarwar. “A study of the normal turbulence model in IEC 61400-1”. In: *Wind Engineering* 36.6 (2012), pp. 759–765.

[43] Joeri A Frederik and Jan-Willem van Wingerden. “On the load impact of dynamic wind farm wake mixing strategies”. In: *Renewable Energy* 194 (2022), pp. 582–595.

[44] Giacomo Valerio Iungo et al. “Linear stability analysis of wind turbine wakes performed on wind tunnel measurements”. In: *Journal of Fluid Mechanics* 737 (2013), pp. 499–526.

[45] Paul J Mason. “Large-eddy simulation: A critical review of the technique”. In: *Quarterly Journal of the Royal Meteorological Society* 120.515 (1994), pp. 1–26.

[46] Marion Coquelet et al. “Simulating the helix wake within an actuator disk framework: verification against discrete-blade type simulations”. In: *Journal of Physics: Conference Series*. Vol. 2505. 1. IOP Publishing. 2023, p. 012017.

[47] Aemilius AW van Vondelen et al. "Control of Periodically Waked Wind Turbines". In: *IEEE Transactions on Control Systems Technology* (2024).

[48] Yrjo Neuvo, Dong Cheng-Yu, and S Mitra. "Interpolated finite impulse response filters". In: *IEEE Transactions on Acoustics, Speech, and Signal Processing* 32.3 (1984), pp. 563–570.

[49] Naoto Abe and Kazuo Yamanaka. "Smith predictor control and internal model control-a tutorial". In: *SICE 2003 Annual Conference (IEEE Cat. No. 03TH8734)*. Vol. 2. IEEE. 2003, pp. 1383–1387.

[50] Sahaj Saxena and Yogesh V Hote. "Advances in internal model control technique: A review and future prospects". In: *IETE Technical Review* 29.6 (2012), pp. 461–472.

[51] Huanshui Zhang and Lihua Xie. *Control and estimation of systems with input/output delays*. Vol. 355. springer, 2007.

[52] Geoffrey Ingram Taylor. "The spectrum of turbulence". In: *Proceedings of the Royal Society of London. Series A-Mathematical and Physical Sciences* 164.919 (1938), pp. 476–490.

[53] Otto JM Smith. "A controller to overcome dead time". In: *iSA journal* 6.2 (1959), pp. 28–33.

[54] Michel Verhaegen and Vincent Verdult. *Filtering and system identification: a least squares approach*. Cambridge university press, 2007.

[55] Abdul J Jerri. "The Shannon sampling theorem—Its various extensions and applications: A tutorial review". In: *Proceedings of the IEEE* 65.11 (1977), pp. 1565–1596.

[56] Gene F Franklin et al. *Feedback control of dynamic systems*. Vol. 4. Prentice hall Upper Saddle River, 2002.

[57] Sigurd Skogestad and Ian Postlethwaite. *Multivariable feedback control: analysis and design*. john Wiley & sons, 2005.

[58] KR Godfrey. "Introduction to binary signals used in system identification". In: *International Conference on Control 1991. Control'91*. IET. 1991, pp. 161–166.

[59] George C Anderson, Brian W Finnie, and Gordon T Roberts. "Pseudo-random and random test signals". In: *Hewlett-Packard Journal* 19.1 (1967), pp. 2–17.

[60] Johannes Wartmann and Susanne Seher-Weiss. "Application of the predictor-based subspace identification method to rotorcraft system identification". In: *39th European rotorcraft forum*. 2013.

[61] Alessandro Chiuso. "On the relation between CCA and predictor-based subspace identification". In: *IEEE Transactions on Automatic Control* 52.10 (2007), pp. 1795–1812.

[62] Edgar Bristol. "On a new measure of interaction for multivariable process control". In: *IEEE transactions on automatic control* 11.1 (1966), pp. 133–134.

[63] Lu Liu et al. "A review of industrial MIMO decoupling control". In: *International Journal of Control, Automation and Systems* 17.5 (2019), pp. 1246–1254.

[64] Basil Kouvaritakis. "Characteristic locus methods for multivariable feedback systems design." PhD thesis. University of Manchester Institute of Science and Technology, 1974.

[65] Steffen Raach et al. "H infinity controller design for closed-loop wake redirection". In: *2017 American Control Conference (ACC)*. IEEE. 2017, pp. 703–708.

[66] BJ Jonkman and L Kilcher. "TurbSim user's guide: version 1.06. 00". In: *National Renewable Energy Laboratory: Golden, CO, USA* (2012).

[67] Anand Parinam et al. "Large-Eddy Simulations of wind turbine wakes in sheared inflows". In: *Journal of Physics: Conference Series*. Vol. 2505. 1. IOP Publishing. 2023, p. 012039.

[68] ST Navalkar, JW Van Wingerden, and GAM Van Kuik. "Individual blade pitch for yaw control". In: *Journal of Physics: Conference Series*. Vol. 524. 1. IOP Publishing. 2014, p. 012057.

[69] Thinal Raj et al. "A survey on LiDAR scanning mechanisms". In: *Electronics* 9.5 (2020), p. 741.

[70] C Reid Turner et al. "A conceptual basis for feature engineering". In: *Journal of Systems and Software* 49.1 (1999), pp. 3–15.

[71] Aemilius AW van Vondelen et al. "Phase Synchronization for Helix Enhanced Wake Mixing in Downstream Wind Turbines". In: *IFAC-PapersOnLine* 56.2 (2023), pp. 8426–8431.

[72] Emanuel Taschner et al. "On the performance of the helix wind farm control approach in the conventionally neutral atmospheric boundary layer". In: *Journal of Physics: Conference Series*. Vol. 2505. 1. IOP Publishing. 2023, p. 012006.

[73] K Shaler et al. "Preliminary introduction of a free vortex wake method into OpenFAST". In: *Journal of Physics: Conference Series*. Vol. 1452. 1. IOP Publishing. 2020, p. 012064.

Glossary

List of Acronyms

AIC	Axial Induction Control
CCW	Counterclockwise
CL	Closed-Loop
CW	Clockwise
DEL	Damage Equivalent Load
DIC	Dynamic Induction Control
DOF	Degree-of-Freedom
FFT	Fast-Fourier Transform
FIR	Finite Impulse Response
GM	Gain Margin
I	Integral
IEC	International Electrotechnical Commission
IECKAI	IEC Kaimal Turbulence Model
IMC	Internal Model Control
IPC	Individual Pitch Control
LCoE	Levelized Cost of Energy
LES	Large Eddy Simulation
LiDAR	Light Detection and Ranging
LQG	Linear Quadratic Gaussian
LQR	Linear Quadratic Regulator
LTI	Linear Time Invariant
MBC	Multi-Blades Coordinate
MIMO	Multiple-Input, Multiple-Output
MPC	Model Predictive Controller

NP	Nominal Performance
NREL	National Renewable Energy Laboratory
NS	Nominal Stability
NTM	Normal Turbulence Model
OL	Open-Loop
PBD	Pitch Bearing Damage
PBSID-opt	Optimized Predictor-based Subspace Identification
PID	Proportional-Integral-Derivative
PI	Proportional-Integral
PM	Phase Margin
PRBN	Pseudo-Random Binary Noise
RHP	Right-Hand-Plant
RP	Robust Performance
RS	Robust Stability
PSD	Power Spectrum Density
RGA	Relative Gain Array
SIMO	Single-Input, Multiple-Output
SISO	Single-Input, Single-Output
SVD	Singular Value Decomposition
TI	Turbulence Intensity
TurbSim	Turbulence Simulator
TSR	Tip Speed Ratio
VAF	Variance-Account-For
WFFC	Wind Farm Flow Control

List of Symbols

β^e_{tilt}	Tilt Pitch Signal in the Helix Frame
β^e_{yaw}	Yaw Pitch Signal in the Helix Frame
β_0	Cumulative Pitch Signal
β_{tilt}	Tilt Pitch Signal in the fixed Frame
β_{yaw}	Yaw Pitch Signal in the fixed Frame
β_i	Pitch Angle for Individual Blade i
γ	Turbine Yaw Setting
ω	Rotor Rotation Rate
ω_b	Bandwidth Frequency

ω_c	Crossover Frequency
ω_r	Wind Turbine Rotating Frequency
ω_{ss}	Steady-State Frequency
ψ_{off}	Azimuth Offset Angle
ψ_i	Azuimuth Angle of Blade i
τ	Time Delay Factor
φ	Half Cone Angle
φ	LiDAR Half Cone Angle
k	Generator Torque Set-point
$\hat{y}$	Delayed Output
$\mathcal{H}_\infty$	H-infinity Controller
St	Strouhal Number
A	Helix Excitation Amplitude
a	Induction Factor
c	Speed of Light
C_p	Power Coefficient
C_t	Thrust Coefficient
D	Rotor Diameter
d	External Disturbance
e	Error Signal
f_0	Original Frequency of Laser Beam
f_e	Excitation Frequency
f_e	Helix Frequency
$G(z)$	Original Plant
$G_{bw}(z)$	Bandwidth Decoupled Plant
$G_{ss}(z)$	Steady-State Decoupled Plant
M_{edge}	Edge-wise Blade Root Bending Moment
M_{flap}	Flap-wise Blade Root Bending Moment
r	Reference Signal
$R(\omega_e t)$	Rotational Matrix
St	Strouhal Number
T_e	Helix Cycle
T_s	Sampling Time
u	Partial Speed
U_{disc}	Rotor-disc Wind Speed
u_{LOS}	Line-of-Sign Speed
U_∞	Hub-high Wind Speed
U_∞	Inflow Velocity
$W(z, F)$	LiDAR Weight Function
W_{bw}	Bandwidth Pre-Compensator

W_{ss}	Steady-State Pre-Compesator
y_{LiDAR}	LiDAR Measurement Output
y_c	Combined Output
y_m	Wind Turbine Measurement Output